

Droplet-Droplet, Droplet-Wall and Microorganism-Wall Collisions

A Thesis

Presented to

the faculty of the School of Engineering and Applied Science

University of Virginia

In Partial Fulfillment of the requirements

for the Degree

Master of Science in Mechanical and Aerospace Engineering

by

K Ghokulla Haran Krishnan

December 2013

APPROVAL SHEET

The thesis
is submitted in partial fulfillment of the requirements
for the degree of
Master of Science

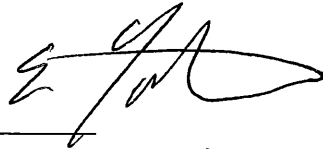


12/09/2013

AUTHOR

The thesis has been read and approved by the examining committee:

Eric Loth

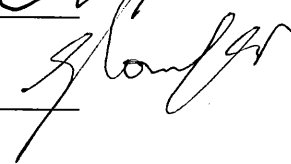


Advisor

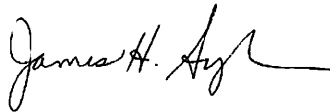
Carl Knospe



Gabriel Laufer



Accepted for the School of Engineering and Applied Science:



Dean, School of Engineering and Applied Science

December
2013

Acknowledgements

I would like to thank the National Science Foundation (NSF) for funding this project. I would like to extend a special thanks to the co-PI's involved in this project Dr. Perry Li, Dr. Terry Simon, Dr. James van de Ven from the University of Minnesota.

I would also like to thank my advisor Dr. Eric Loth for his unparalleled guidance and advice, knowledge, and motivation throughout this project. I'd also like to thank other members of the Loth research group at the University of Virginia in providing help and support. I would also like to thank undergraduate student researchers Peter Malm and Michael Starr in their efforts in data collection.

I would like thank my family for the love and support throughout my graduate studies.

List of Contents

List of Figures	vi
1 Drop-Drop Collision Regimes for Variable Gas Pressures and Viscosities	1
1.1 Introduction	1
1.2 Experimental Data Surveyed	12
1.3 Results	13
1.4 Conclusions	25
1.5 Appendix	44
1.6 References	50
2 Predicting Contact Angles for Regular Surfaces	54
2.1 Introduction	54
2.2 Data Surveyed	57
2.3 Results and Discussion	60
2.4 Conclusions	69
2.5 References	70
3 Drop Impact on Nanotextured Surfaces	72
3.1 Introduction	72
3.2 Experimental Setup	79
3.3 Results	81

3.4 Conclusion	96
3.5 Appendix	97
3.6 References	98
4 Hydrophobic Coating Resistance to Freshwater Biofouling Inception	100
4.1 Introduction	100
4.2 Experimental Methods	105
4.3 Results of Dynamic Testing	108
4.4 Conclusions	115
4.5 References	116

List of Figures

Figure 1.1 Collisional geometry between a large particle of diameter d_{large} and a small particle of diameter d_{small} , where the collision plane is tangent to their surfaces at the initial collision point. The incoming impact angle (θ) is based on the relative velocity and the collision plane and θ equals 90° for head-on collisions and approaches 0° for grazing collisions.	28
Figure 1.2 Classification of outcomes of droplet-droplet interactions based on increasing relative velocity for first four columns	29
Figure 1.3 Stability nomogram of water droplet interaction in a 7.5 atm helium environment showing experimental outcomes as symbols (Qian and Law, 1997) and droplet-interaction outcome boundaries as lines based only on the experimental data (no models).	30
Figure 1.4 Experimental outcomes in nitrogen (Qian and Law, 1997) compared to previous prediction models of outcome boundaries for: a) water drops in 1 atm and b) water drops in 8 atm and c) tetradecane drops in 1 atm.	31
Figure 1.5 Influence of droplet viscosity on horizontal intercept between fast coalescence and reflexive separation (experiments as symbols)	32
Figure 1.6 Droplet-droplet outcomes for ethanol in air at one atmosphere (Estrade <i>et al.</i> 1999) and present models for outcome boundaries	33
Figure 1.7 Droplet-droplet outcome boundaries for: a) water drops & b) tetradecane drops in nitrogen. (Qian & Law, 1997)	34
Figure 1.8 Droplet-droplet outcomes (Kuschel & Sommerfeld, 2011) compared to	35

present models for outcome boundaries for a) ethanol, b) propanol and c) hexanol in air at 1 atm.

Figure 1.9 Experimental droplet-droplet outcome boundaries as symbols for high viscosity drops in air at 1 atm (Gotaas et al., 2007) compared to present models for outcome boundaries as lines for a) monoethylglycol, b) diethylglycol and c) triethylglycol. 36

Figure 1.10 Influence of particle viscosity on horizontal intercept between fast coalescence and stretching separation for: a) low Ohnesorge drops and b) high Ohnesorge drops. 37

Figure 1.11 Droplet-droplet outcomes for water drops (Qian & Law, 1997) compared to present models for outcome boundaries where surrounding gas is nitrogen at: a) 2.7 atm & b) 8 atm. 38

Figure 1.12 Droplet-droplet outcomes for water drops (Qian & Law, 1997) compared to present outcome boundaries where surrounding gas is helium at: a) 4.4 atm, b) 7.5 atm and c) 11.7 atm 39

Figure 1.13 Influence of drop and gas properties on a) horizontal intercept i.e. We_{B0} b) mid-point interval i.e. $We_{B0.5}$, between bounce and fast coalescence. 40

Figure 1.14 Creation of an internal bubble of gas: a) numerical evolution at $Re=We=1$ showing concave interface for drops that can create a viscously trapped gas when the interfaces are numerically prevented from merging (Jiang, 2006) and b) qualitative illustration of the thin gas bubble trapped between the droplets just after initial impact (similar to $t=0.37$ time frame from above) at higher Weber number where deformations are greater. 41

Figure 1.15 Water droplet outcomes in air at 1 atm at different relative humidity (Ochs <i>et al.</i> 1989) showing three pairs of data at two humidity levels with data artificially shifted within a pair to avoid symbol overlap. The results indicate a weak or negligible effect of humidity on the outcome, consistent with present model boundaries in lines.	42
Figure 1.16 Influence of drop viscosity and gas pressure on horizontal intercept between slow coalescence and bounce, i.e. We_{SC} , where the outcome of Q& L tetradecane drops colliding in ethylene gas is also shown assuming a partial ethylene film at the interface determines the drop interaction properties (denoted by blue solid square).	43
Figure 1.17 Droplet-droplet regimes for tetradecane drops in (Qian & Law, 1997) compared to present outcome boundaries for: a) 100% ethylene b) 50% ethylene-50 % nitrogen and c) 100% nitrogen in 8 atm.	44
Figure 1.A.1 Droplet-droplet regimes for hydrocarbon droplets in air at 1 atm: a) heptanol, b) nonanol and c) dodecylalcohol. (Kuschel & Sommerfeld, 2011).	45
Figure 1.A.2 Droplet-droplet regimes for a) 10% pvp, b) 20% pvp and c) 30% pvp, droplets in air at 1 atm. (Kuschel & Sommerfeld, 2011).	46
Figure 1.A.3 Droplet-droplet regimes for a) water (Kuschel & Sommerfeld, 2011) and b) diesel (Post & Abraham, 2001), droplets in air at 1 atm.	47
Figure 1.A.4 Droplet-droplet regimes for tetradecane droplets in nitrogen at: a) 0.6 atm, b) 2.4 atm (Qian & Law, 1997).	48
Figure 1.A.5 Droplet-droplet regimes for tetradecane droplets in helium at: a) 0.7	49

atm, b) 2.4 atm and c) 4.4 atm (Qian & Law, 1997).

Figure 1.A.6 Droplet-droplet regimes for water drops in air at one atmosphere (Ashgriz-Poo, 1990).	50
---	----

Figure 2.1 Images of surfaces used for present survey listed by row:	59
--	----

Figure 2.2 Receding contact angle as a function of roughness ratio	60
--	----

Figure 2.3 Receding contact angle as a function of solid fraction	62
---	----

Figure 2.4 Advancing contact angle as a function of roughness ratio	63
---	----

Figure 2.5 Advancing contact angle as a function of solid fraction	64
--	----

Figure 2.6 Static contact angle as a function of roughness ratio	65
--	----

Figure 2.7 Static contact angle as a function of solid fraction	67
---	----

Figure 2.8 Transition roughness as a function of solid fraction	68
---	----

Figure 3.1 Performance of previous deposition boundary models compared to data for a variety of surfaces and liquids where solid symbols indicate deposition and starred symbol indicate splashing	78
--	----

Figure 3.2 Droplet velocity against height	80
--	----

Figure 3.3 a) Illustration and b) Picture of the experimental setup	81
---	----

Figure 3.4 Observed outcomes of droplet-wall collision	83
--	----

Figure 3.5 We-Oh regime for various liquid on aluminum surface	85
--	----

Figure 3.6 We-Oh regime for various liquid on a superhydrophobic surface, SH-1	87
--	----

Figure 3.7 Water droplet collision outcomes on various surfaces for the hydrophobic and hydrophobic regimes as defined by the receding contact angle.	90
--	----

Figure 3.8 Collision outcomes on various surfaces as a function of receding contact angle for 40% Glycerin/Water droplets	92
Figure 3.9 Collision outcomes on various surfaces as a function of receding contact angle for 60% Glycerin/Water droplets	92
Figure 3.10 Collision outcomes on various surfaces as a function of receding contact angle for 77% Glycerin/Water droplets	93
Figure 3.11 Plot of We_{Dep} against the receding contact angle for various Ohnesorge liquids	95
Figure 4.1 Skin friction increase in terms of roughness and Reynolds numbers where blue arrows indicate friction at location for laminar and turbulent conditions.	101
Figure 4.2 Biofouling effects on boundary layers: a) surface-view visualization of turbulent transition due to fouling elements (glass microspheres) shown by arrows from flow over a test article in the 48" water tunnel in the Applied Research Lab at Penn State University, courtesy of Alan Jennings, and b) side-view of average boundary layer growth (as dashed line) due to transition caused by fouling element.	103
Figure 4.3 Images of surfaces before and after dynamic testing with arrows indicating fouling elements (very little fouling was observed for the PUR + NC surface).	110
Figure 4.4 Magnified images detailing the variety of biofouling specimens found on the polyurethane sample, including a) algae, b) fine plant litter, c) ciliates, d) chlorophytes, e) insect parts, and f) unidentified microorganism	111
Figure 4.5 Three-dimensional surface rendering based digital microscope: a) for Fig.	112

4.4e, b) for Fig. 4.4f

Figure 4.6 Plot denoting average number of fouling elements in a 1 cm x 1cm field
of view for each surface based on height bins 114

1 Drop-Drop Collision Regimes for Variable Gas Pressures and Viscosities

1.1 Introduction

Droplet-droplet collisions in a gas occur when droplets move towards each other in flight and come into direct contact. The “outcome” is defined herein to be the state of the liquid matter after the collision process is completed and generally can be classified as an agglomeration (two drops become one drop), reflection (two drops stays as two drops), or a break-up (more than two drops result from the interaction). The outcome can be important for many energy systems, particularly fuel sprays in the near injector region, where there can be many collisions between droplets (defined as drops with diameters of less than 500 microns). The outcomes for these interactions are critical to the overall size distributions, which in turn can affect overall combustion performance. Models for predicting the outcome are typically based on inviscid stability criterion and are validated using experimental data of water droplets colliding in atmospheric pressure conditions. However, combustion sprays generally include hydrocarbon droplets (with lower surface tension and higher viscosity) impacting in high pressures gasses and often with elevated temperatures (where gas densities and viscosities are also elevated). As such, a robust set of models to predicting the collision outcome under conditions of variable gas pressure and viscosity as well as variable viscosity and surface tension of the liquid is important for computational modeling of such systems.^{1,2}

The most common interaction is a “binary” collision whereby two droplets collide as shown in Fig. 1.1. In comparison, ternary and more complex collisions are generally rare for aerosol sprays. A binary collision typically results in significant deformation if there is a large “relative velocity”, which is defined below and in Fig. 1.1 as

$$\mathbf{V}_{p-p} \equiv \mathbf{V}_{\text{large}}^{\text{in}} - \mathbf{V}_{\text{small}}^{\text{in}} \quad (1.1)$$

If the drops are of similar size³, the collision dynamics can be classified by five types based on Qian and Law⁴, (hereafter referred to as Q&L). Examples of these five are shown in Fig. 2 in order of increasing relative velocity for a given size of droplets and given liquid, and include:

SC: “slow coalescence” where the droplets move slow enough that the deformation is weak and the interaction times is long enough time for the interfaces to merge by diffusion;

B: “bounce” where the impact speeds yield significant deformation but the interaction is too fast for merger, such that the drops reflect away from each other after impact;

FC: “fast coalescence” which includes significant deformation dynamics causing the interfaces to break and merge, after which the dynamics subside and a single combined drop is formed;

RS: “reflexive separation” where the droplets impact at roughly head-on angles and temporarily coalesce as their interfaces “pancake” due to the high impact speeds (as in FC), but the high inertias and dynamics then leads to separation yielding two primary drops and often a smaller drop when the connecting filament breaks;

SS: “stretching separation” or “off-center separation” where the droplets impact at roughly grazing conditions and temporarily coalesce via a ligament but then separate as they continue past each other and yielding two primary droplets and often many satellite droplets.

To characterize the destabilizing effects of inertia compared to the stabilizing effects of surface tension, the collision Weber number is defined using the small drop diameter (d_{small}), droplet density (ρ_p), and the liquid-gas surface tension (σ) as:

$$\text{We}_{p-p} \equiv \frac{\rho_p v_{p-p}^2 d_{\text{small}}}{\sigma} \quad (1.2)$$

This inviscid parameter is the strongest determinant of the impact outcomes for head-on

collisions when the collision Weber value is larger than unity. Note that in Fig. 1.2, the pre-collision droplet geometries are spherical indicating that the aerodynamic Weber number (based on air density) is small compared to unity.

If the collisions are not head-on, the second most influential parameter is the incoming impact angle (θ) between the drop-drop collision plane and the relative incoming velocity vector as defined in Fig. 1.1. This angle can be used to define an impact parameter:

$$\beta \equiv \cos(\theta) \quad (1.3)$$

Thus, a head-on collision corresponds to $\beta \approx 0$ ($\theta \approx 90^\circ$) while a nearly tangential grazing condition corresponds to $\beta \approx 1$ ($\theta \approx 0^\circ$).

The third most influential non-dimensional parameter is the drop size ratio (Δ), which simply normalizes the small diameter (d_{small}) by the large diameter (d_{large}) as:

$$\Delta \equiv \frac{d_{\text{small}}}{d_{\text{large}}} \quad (1.4)$$

As the drop size ratio becomes much less than unity, the collision outcome will depend primarily on the properties of the small droplet size (since the large droplet will approach that of an infinite liquid bath).

If one ignores viscous effects and assumes a fixed size ratio, the droplet collisions are thus primarily characterized by two non-dimensional parameters: We_{p-p} and β . The dependence of these parameters on the collision outcome (SC, B, FC, SS, and RS) can be expressed in terms of a nomogram as shown by the example in Fig. 1.3. In this figure, lines are drawn to indicate the qualitative boundaries between the regimes. In order to quantify the boundaries for head-on collision ($\beta=0$), three critical Weber numbers can be defined: We_{SC} as the SC/B horizontal intercept, We_B as the B/FC horizontal intercept, and We_{FC} as the FC/RS horizontal intercept. Since the FC/SS boundary does not generally occur for head-on collisions and has no horizontal

intercept, it can be quantified by defining a fourth critical Weber number, We_{SS} , as the FC/SS boundary at $\beta=0.5$. Furthermore, a fifth critical Weber number, $We_{B0.5}$, can be defined as the B/FC boundary at $\beta=0.5$ which is used in the present models to differentiate between the controlling physics for We_B . One may note that there is significant experimental uncertainty regarding the boundaries between these regimes, which is typical of such measurements and is attributed to the difficulty in prescribing and measuring the impact conditions as well as in controlling any pre-collision instabilities.

As noted in Fig. 1.3, the boundary between slow coalescence and bounce (SC/B, shown a short-dashed line) is observed at very low Weber numbers for mainly head-on collisions. Slow coalescence ($We_{p-p} < We_{SC}$) occurs when the liquid interfaces can be connected across the gas film through a “drainage” process before the collision process is completed.

At higher impact velocities ($We_{SC} < We_{p-p} < We_B$) for a head-on collision, the gas interface integrity between the drops is maintained so the droplets will repel as two separate entities, i.e. they will bounce. One may expect that increased gas pressure will serve to improve the probability of a bounce outcome by keeping the gas film stable and this trend is consistent with experiments of Q&L. As the Weber number is increased further ($We_B < We_{p-p} < We_{FC}$) for a head-on collision, increased deformation of the droplets yields instabilities that provoke rupture of the interfaces leading to a merger of the two droplets, and this is identified as fast coalescence. As shown in Fig. 1.3, off-axis collisions ($\beta > 0$) with smaller normal velocity components are less likely to have interface rupture (more likely to bounce) so that the Weber number for the B/FC boundary (shown a solid black line) will increase as the β increases.

When the drop Weber number becomes very large (and surface tension effects are weakened), the internal dynamics of the droplet after the merger become even more exaggerated and can cause re-separation (Fig. 1.2). This occurs when a temporarily coalesced entity has very

high internal kinetic energy and interface dynamics owing to high collision velocities, which causes a dumbbell shape of two large masses (connected by a filament) moving away from each other. The high momentum in the opposite directions causes the filament to break droplets to re-separate (Fig. 1.2). For a head-on collision ($\beta=0$) with large enough Weber number ($We_{p-p} > We_{FC}$) this leads to RS, while re-separation for a near-grazing condition leads to SS. These two boundaries are shown in Fig. 1.3 as a thick grey line and a long-dashed line, respectively. Brazier-Smith *et al.*⁵ showed that increasing the We_{p-p} for the stretching separation regime also increases the number of small satellite drops which are formed, due to increased instability of the temporary filament. At very high impact speeds (ca. $We_{p-p} > 100$), a “shattering separation” occurs whereby the combined mass rapidly breaks up into several drops⁶. However, this sixth regime and other rapid break-up regimes are beyond the scope of this study.

In all of the five regimes studied herein, viscous effects can generally stabilize a drop collision and allow increased critical Weber numbers. In some cases, the gas viscosity may also influence the collision outcome, if a cushion of gas is formed. To characterize their influence, it is convenient to define the drop and gas Ohnesorge numbers based on their respective viscosities (μ_p and μ_f) and densities (ρ_p and ρ_f) and the interfacial surface tension (σ):

$$Oh_p \equiv \frac{\mu_p}{\sqrt{\rho_p \sigma d}} \quad (1.5a)$$

$$Oh_f \equiv \frac{\mu_f}{\sqrt{\rho_f \sigma d}} = Oh_p \frac{\sqrt{\rho_p / \rho_f}}{\mu_p / \mu_f} \quad (1.5b)$$

These two dimensionless parameters relate internal and external viscous stresses to surface tension stresses. For drops in gasses, $Oh_p > Oh_f$ so that one may expect Oh_p to generally dominate the viscous influence for deformation.

In this study, data are reviewed to characterize the various physics which control the outcomes of droplet-droplet collisions, especially in terms of the above non-dimensional

quantities. The test conditions are limited to those for which the flow speeds are not impacted by compressibility or by non-continuum effects. Furthermore, previous models for the boundaries between these regimes in the domain of Weber number and impact parameter are considered. However, as discussed in the following section, there is not a robust set of models that accurately predict the boundaries between the five outcomes of Fig. 1.2 for variable gas density and droplet viscosity for spherical droplets that impact at significant Weber numbers ($We_{p-p} > 1$).

Based on this motivation, the first objective of this study is examine a wide set of experimental data sets that represent the totality of rigorous published data associated with the above conditions, thereby providing the most comprehensive overview yet presented (to the author's knowledge). The data sets investigated and reviewed are summarized in Table 1.1. The second objective is examine previous models for outcome predictions, and to develop and validate improved boundary models that can be used to predict the spray characteristics in energy systems.^{1,2}

1.1.2 Previous Studies

There have been several studies that have examined and proposed models for the boundaries between bounce, fast coalescence, reflexive separation, and stretching separation. These models have been primarily based on inviscid instabilities and validated with collisions of water droplets in air at standard pressure and temperature ($p_o = 101,320 \text{ N/m}^2$ and $T_o = 293\text{K}$). The most common of these predictive models are discussed below in the order of increasing impact Weber number. They are also presented and compared in Fig. 1.4 to experimental data at varying gas pressures and drop viscosities. One exception is the boundary between slow coalescence and bouncing for which no previous models are available for the conditions associated with Table 1.1 (as discussed below), at least to the author's knowledge.

A. The SC/B Boundary:

There are only a few studies which model the boundary between slow coalescence and bouncing and most, if not all, focus on different conditions than those described in Table 1.1. For example, Bach *et al.*⁷ considered 20-40 micron drops impacting on a nearly planar interface. For these small sizes, the Knudsen number (Kn , which is a measure of molecular mean free path to the droplet diameter) was no longer small and revealed the presence of non-continuum effects. Furthermore, the very small impact velocities yielded very small Weber numbers ($We_{p-p} < 10^{-3}$) indicating negligible deformation. In contrast, the drops in Table 1.1 have much larger diameters yielding small Knudsen numbers ($Kn < 10^{-3}$) so that non-continuum effects are expected to be negligible. In addition, their impact velocities are much higher yielding significant Weber numbers ($We_{p-p} > 1$) so deformation at impact will be important.

Another study considered the rebound of solid particles in a liquid bath, and showed that the rebound can be damped by the surrounding fluid viscosity if the impact Stokes number was of order unity or smaller.⁶ The impact Stokes number can be expressed as $St_{\perp} = We^{1/2}/Oh$, whereby this damping effect becomes important for $St_{\perp} < 25$. Since the drop-drop experiments in gas of Table 1.1 have impact Stokes numbers in the range of 25-500, this particular viscous damping effect is not expected to play a large role.

As such, there are no previous models or detailed analyses for the boundary between slow coalescence and bouncing for Table 1.1 conditions. However, Q&L noted that slow coalescence is more likely than bounce for low surface tension liquids (e. hydrocarbons) and at low gas pressure. In fact, Willis and Orme (2000) suggested that drops will not bounce at all in a vacuum.

B. The B/FC Boundary:

To describe the boundary between bouncing and fast coalescence, Estrade *et al.*⁹ proposed that bouncing will occur if the initial kinetic energy does not exceed that needed to create a minimum deformation limit. The resulting inviscid model is given as

$$We_{B/FC} = \frac{\Delta(1+\Delta^2)(4\phi'-12)}{\chi(1-\beta^2)} \quad (1.6a)$$

$$\chi = \begin{cases} 1-(2-\psi)(1+\psi)/4 & \text{if } \psi > 1.0 \\ \psi^2(3-\psi)/4 & \text{if } \psi \leq 1.0 \end{cases} \quad (1.6b)$$

$$\psi \equiv (1-\beta)(1+\Delta) \quad (1.6c)$$

$$\phi' \equiv 2 \left(\frac{3}{4\phi^2} + 1 \right)^{-2/3} + \left(\frac{3}{4\phi^2} + 1 \right)^{1/3} \quad (1.6d)$$

In this expression, ϕ is defined as the ratio of $\delta_{\text{large}}/d_{\text{large}}$ or the ratio of $\delta_{\text{small}}/d_{\text{small}}$ beyond which coalescence or separation occurs, with δ being the deformed droplet width normal to the collision velocity.

The predictions based on the above model correlated reasonably well with the data of Estrade *et al.*⁹ for methyl alcohol drops in air at one atmosphere. However, this model is only qualitatively correct when evaluated with water droplets. In particular, the $We_{B/FC}$ is substantially over-predicted for water drops in one atmosphere pressure (Fig. 1.4a) and under-predicted at eight atmospheres pressure (Fig. 1.4b). This indicates a significant sensitivity to gas pressure, which is absent from their model, but consistently observed by Qian & Law.⁴ This effect is attributed to a gas cushion which can develop between the two droplet interfaces at the minimum gap distance. This cushion can be maintained when the gas is not able to squeeze out fast enough to prevent interface coalescence. The time for the gas to escape may be a function of

the gas viscosity but droplet viscosity may also influence the B/FC boundary since it can dampen the dynamics of the liquid motion. This influence is demonstrated by comparing Fig. 1.4a and Fig. 1.4c whereby fast coalescence is less likely to occur for tetradecane droplets than water droplets at the same Weber number and pressure. These gas and droplet viscosity effects are neglected in Eq. (1.6), which may explain why the model is not robust for the conditions of Fig. 1.4.

C. The FC/RS Boundary:

Ashgriz and Poo¹⁰, hereafter referred to as A&P, developed a model for the appearance of reflexive, or head-on separation. This was based on the total surface energy of the drops compared to the internal reflexive kinetic energy of the fluid within the droplets. Their criterion states that reflexive separation will occur if the reflexive kinetic energy of the two combined droplets is greater than 75% of the surface energy. This postulate leads to the following form for the outcome boundary:

$$We_{FC/RS} = 3 \left[7(1+\Delta^3)^{2/3} - 4(1+\Delta^2) \right] \frac{\Delta(1+\Delta^3)^2}{\Delta^6 \eta_1 + \eta_2} \quad (1.7a)$$

$$\eta_1 = 2(1-\xi)^2 (1-\xi^2)^{1/2} - 1 \quad (1.7b)$$

$$\eta_2 = 2(\Delta-\xi)^2 (\Delta^2-\xi^2)^{1/2} - \Delta^3 \quad (1.7c)$$

$$\xi = \frac{1}{2}\beta(1+\Delta) \quad (1.7d)$$

This model correctly predicts the qualitative trends observed in experiments, but under-predicts $We_{FC/RS}$ for liquids with higher droplet viscosity, as shown in Fig. 1.4c (where many coalescence events are noted below the predicted boundary). This can be attributed to the internal drop viscous losses which dampen the kinetic energy required for separation; an effect that was

recognized by Jiang *et al.*¹¹ To incorporate this droplet viscosity effect, Q&L⁴ expressed the head-on intercept boundary value (at $\beta=0$) as We_{FC} and modeled this intercept in terms of the droplet Ohnesorge number defined in Eq. (1.5a) as:

$$We_{FC} \approx 680Oh_p + 15 \quad (1.8)$$

It should be noted that these values were obtained by assuming a nearly vertical (i.e. blunt) intercept for the FC/RS boundary. However, many experiments indicate a shallow intercept behavior (as shown in Fig. 1.3) and a shallow intercept is also consistent with the model of A&P (Fig. 1.4). Therefore, a model which incorporates the Ohnesorge effects of Q&L with the β effects of A&P may provide a more robust and accurate description.

D. The FC/SS Boundary:

Several models have been proposed for the FC/SS boundary and the most common are discussed below. By considering the necessary energy required to form two separate droplets, Brazier-Smith *et al.*⁵ proposed a criterion based on the amount of rotational energy required to overcome the surface energy of the two drops. This led to the following boundary for droplets to collide and re-separate:

$$We_{FC/SS} = \frac{4.8 \left\{ 1 + \Delta^{-2} - (1 + \Delta^{-3})^{2/3} \right\} (1 + \Delta^{-3})^{11/3}}{\beta^2 \Delta^{-6} (1 + \Delta^{-1})^2} \quad (1.9)$$

This model was an improvement over a similar model developed by Park¹², which utilized a relationship between the surface tension and the angular momentum of the particles at their initial point of contact.

Arkhipov¹³ later developed a formulation based on the minimum potential-energy variational principle and the assumption of a system with constant angular velocity. The resulting boundary can be described as:

$$\text{We}_{\text{FC/SS}} = \left(\frac{1}{\Delta^3} \right)^2 \left(\frac{6(1+\Delta^3)}{\beta^2} \right) \quad (1.10)$$

If one neglects the size ratio effects ($\Delta=1$), the relations become very similar with Eq. 1.9 reducing to $9/\beta^2$ and Eq. 1.10 reducing to $12/\beta^2$.

A&P expressed some reservations about all three of the models discussed above and suggested that separation occurs if the total effective stretching kinetic energy is larger than the surface energy of the region of interaction. Their model can be expressed as:

$$\text{We}_{\text{FC/SS}} = \frac{4(1+\Delta^3)^2 \left[3(1+\Delta)(1-\beta)(\Delta^3 \phi_{\text{small}} + \phi_{\text{large}}) \right]^{1/2}}{\Delta^2 \left[(1+\Delta^3) - (1-\beta^2)(\phi_{\text{small}} + \Delta^3 \phi_{\text{large}}) \right]} \quad (1.11a)$$

$$\phi_{\text{small}} = \begin{cases} 1 - \frac{1}{4\Delta^3} (2\Delta - \tau)^2 (\Delta + \tau) & \text{for } h > \frac{1}{2} d_{\text{small}} \\ \frac{\tau^2}{4\Delta^3} (3\Delta - \tau) & \text{for } h < \frac{1}{2} d_{\text{small}} \end{cases} \quad (1.11b)$$

$$\phi_{\text{large}} = \begin{cases} 1 - \frac{1}{4} (2 - \tau)^2 (1 + \tau) & \text{for } h > \frac{1}{2} d_{\text{large}} \\ \frac{\tau^2}{4} (3 - \tau) & \text{for } h < \frac{1}{2} d_{\text{large}} \end{cases} \quad (1.11c)$$

$$\tau \equiv (1+\Delta)(1-\beta) \quad (1.11d)$$

$$h \equiv \frac{1}{2} (d_{\text{small}} + d_{\text{large}}) (1-\beta) \quad (1.11e)$$

This model is more complex than those of Eqs. (1.9) or (1.10), but is still only a function of impact angle, β and drop size ratio, Δ .

The predictions from Eqs. 1.9 and 1.11 are quite similar and reasonable for water droplets at one atmosphere (Fig. 1.4a). Since this is the most commonly studied condition, their prediction models are perhaps the most commonly cited. Their predictions are also reasonable for water at eight atmospheres pressure (Fig. 1.4b) indicating that gas pressure effects are not substantial for

this boundary. However, for hydrocarbons droplets with increased viscosity, the inviscid model of Brazier-Smith *et al.* and A&P tend to under-predict the $We_{FC/SS}$ number for a given β (while the model of Arkhipov gives better agreement with experiments). This is attributed to increased dissipation of energy which can prevent the droplets from re-separating once temporarily coalesced. This tendency is consistent with experiments of Jiang *et al.*¹¹ for a wide variety of liquid/droplet properties. Brenn and Kolobaric¹⁴ proposed a model to include the effect of drop viscosity on the FC/SS boundary which gave good results for high viscosity liquids (Oh_p on the order of 0.5 and greater). However, their predictions yielded poor results for low viscosity liquids like water and alcohol. For example, the predictions for 300 μm water drops with an Oh_p of 0.0068 based on Brenn and Kolobaric¹⁴ model yields We_{FC} values in excess of 1000, while experimental We_{FC} values (Brazier-Smith *et al.*⁸) are only on the order of 20-25. Thus, a robust model for this boundary is not currently available.

1.2 Experimental Data Surveyed

To investigate the various collision regimes, a comprehensive review was undertaken to obtain quantitative nomograms from all relevant experimental studies which included Weber numbers between 1 and 100 (where significant deformation occurs but surface tension effects cannot be neglected). In addition to that, only uncharged and binary interactions were considered. On the basis on the data quality and quantity to establish specific conditions for droplet collision outcomes (e.g. a bounce), the following experimental studies were selected: Q&L⁴, Estrade *et al.*⁹, A&P¹⁰, Jiang *et al.*¹¹, Ochs III *et al.*¹⁵ Gotaas¹⁶ and Kuschel & Sommerfeld¹⁹. Table 1 lists the droplet and gas properties of the selected studies. Note that some of the test conditions only reported a range of droplet diameters for a nomogram (as opposed to a fixed droplet diameter) for each point on the nomogram). To model these cases

herein, the average droplet diameter was employed to compute the Oh_p , Oh_f , etc. The largest expected deviation from this average from was the case of Q&L who reported diameters ranging from 200 μm to 400 μm , which resulted in an uncertainty of about $\pm 40\%$ in the We and $\pm 20\%$ in the Oh_p . In addition, there is significant uncertainty for some of the boundaries due to inconsistent reported outcome as previously mentioned for Fig. 1.3. This indicates the high sensitivity of the outcomes to minor changes in experimental conditions and this uncertainty must also be considered when assessing models for the boundaries.

1.3 Results

As noted above, predictions from previous models were found to be only qualitatively consistent for boundary predictions. This lack of fidelity motivated the present work, whose primary objective was to thoroughly review available data to provide a comprehensive assessment and whose secondary objective was to develop quantitative boundary models which take into account effects of droplet and gas viscosity, as well as the pressure and density of the surrounding gas. The models developed herein were kept relatively simple so that they may be computed rapidly for a large number of droplet interactions and since the outcome uncertainty of the experimental results did not justify more detailed and complex descriptions. The experimental data reviewed herein is first discussed, followed by proposed models for each of the four aforementioned boundaries, starting with high Weber number outcomes (where more models and experiments are available) and proceeding to lower Weber number outcomes (where experiments and robust models are less common).

1.3.1 The FC/RS Boundary:

As discussed earlier (§1.1.2 C), the boundary between fast coalescence and reflexive separation was treated theoretically by A&P for inviscid conditions and their model gave reasonable agreement with experiments at low droplet viscosities. However, Q&L noted a significant influence of Oh_p for droplets with high liquid viscosity. This effect can be traced to the reduced rebound dynamics associated with increasing the droplet viscosity, as discussed by Bayer & Megaridis¹⁸. The viscosity can thus reduce the velocity associated with stretching the merged droplets apart, which can stabilize the coalescence and increase We_{FC} . Q&L proposed a linear relationship to take droplet viscosity into account for the intercept value (We_{FC}) assuming a blunt, nearly vertical, intercept curve. Their relationship is given by Eq. (1.8) and is shown as a dashed line in Fig. 1.5a. Also included in this figure are the We_{FC} values obtained by assuming a blunt intercept as per Q&L. It can be seen that increasing Oh_p generally leads to increased We_{FC} , i.e. increasing viscous effects tends to prevent the temporarily coalesced droplets from re-separating due to dissipation of the kinetic energy. In general, the Q&L model is consistent with the data that assume a blunt intercept. However, a notable exception is the data of Adams *et al.*³ for charged drops. Such a result is consistent with findings of Czys and Ochs²⁰ who noted that charged droplets are more likely to coalesce even when the charges are of the same sign (since the difference in magnitude between charges can cause attraction).

An issue with the Q&L empirical model is that it assumes a blunt intercept. However, the theory of A&P (Eq. (1.7)) and most of the experimental data indicate an angled-intercept for this boundary. As such, the Q&L of Eq. (1.8) generally leads to an over-prediction of the boundary Weber numbers once a variety of collision angles are considered on a nomogram. Therefore, the measurements from the nomograms of Table 1.1 were analyzed assuming an angled intercept consistent with the theory of A&P. The results indicated that there are two Ohnesorge regimes,

which are modeled herein with two empirical fits:

$$We_{FC} = 700Oh_p + 12 \quad (1.12)$$

The proposed linear fit of the intercept values for low Ohnesorge data (Eq. 1.12) is shown in Fig. 1.5 along with the experimental data in grey and solid symbols. Recent simulations by Gotaas *et al.*¹⁶ on high viscosity droplets indicate that We_{FC} could exponentially increase at high Oh number ($Oh > 0.1$) prompting Gotaas *et al.*¹⁶ to propose the following power law model for “highly viscous” drops

$$We_{FC} = 9309(Oh_p)^{1.7056} \quad \text{for } Oh_p > 0.04 \quad (1.13)$$

However, the experiments of Fig. 1.5 for a wide range of droplet viscosity ($0.015 < Oh < 0.08$), especially those of Kuschel & Sommerfeld¹⁹ suggests that the present model given by Eq. 1.12 is reasonably accurate, as also shown in Fig. 1.5. In particular, the shift from the linear variation of Eq. 1.12 for “highly viscous” drops may not occur until $Oh > 0.1$. To investigate the trends for higher Ohnesorge number drops, more experiments are needed.

While Eq. 1.12 gives the angled intercept values, one must account for collision angle effects as well. To obtain this dependence, the four-equation model given by A&P (Eq. 1.7a-d) was simplified to a single equation for computational convenience as:

$$We_{FC/RS} = \frac{We_{FC}}{(1-3\beta)\Delta} \quad (1.14)$$

This expression assumes that the larger droplet primarily determines the outcome of the collision. Furthermore, the differences introduced by this simplification are less than the uncertainty associated with the experimentally observed outcome boundaries.

The combination of Eqs. (1.12) and (1.14) was then evaluated with the data of Table 1 and this model was found to be reasonably robust. For example, the effect of diameter ratio (Δ) is shown in Fig. 1.6, where the changes predicted by the present simplified version of A&P’s

model are consistent with the experimental data. The effect of droplet viscosity through Oh_p is seen in Figs. 1.7 and 1.8 in which a significant shift in FC/RS boundary is seen as the Oh_p increases for both the experimental data and for the model. Similar experimental trends and model performance are found in later figures. It is important to note that We_{FC} was found to be relatively independent of the gas properties (density, pressure, etc.).

1.3.2. The FC/SS Boundary:

Similar to the phenomenon associated with the FC/RS, inviscid dynamics are the primary mechanism for the boundary between fast coalescence and stretching separation for the conditions of Table 1. The inviscid transition is shown by the thin solid black lines in the figures whereby the inviscid Brazier-Smith *et al.*⁵ and A&P models for the FC/SS boundary behaved reasonably well for water droplets. However, droplet viscosity can also play a significant secondary role as evidenced by the experiments of Jiang *et al.*¹¹ and others whereby that the FC/SS boundary tends to larger Weber numbers as the drop viscosity (and thus Oh_p) increases. The recent experiments conducted by Gotaas *et al.*¹⁶ with high viscosity drops suggested a similar trend with increasing viscosity although with a varying degree of dependence. This increasing importance of droplet viscosity can be traced to an increase in the droplet Reynolds number (as defined by the impact velocity) whereby the liquid Reynolds numbers for the water droplets at the intercept conditions are on the order of 60-500 but are on the order of 15-25 for the drops of Gotaas *et al.*¹⁶

To determine this dependence, measured values of We_{SS} were evaluated as a function of Oh_p for the available experimental data of Table 1.1. As with the We_{FC} dependence, the We_{SS} showed a consistent increase for higher drop Ohnesorge numbers. This trend is shown by Fig. 1.10 and can be approximated as

$$We_{ss}=630(Oh_p)+21 \quad \text{for } Oh_p \leq 0.03 \quad (1.15a)$$

$$We_{ss}=135(Oh_p)+36 \quad \text{for } Oh_p > 0.03 \quad (1.15b)$$

This empirical dependence was based on a wide variation of surrounding gas properties (pressure, density and chemical composition) and drop properties (diameter, viscosity, and surface tension). This result is also qualitatively consistent with data obtained by Brenn *et al.*²¹ which focused on satellite formation.

To incorporate collision angle dependence, the form of the Brazier-Smith boundary equation is employed for the present model as it is quite reasonable in the limit of very low Oh_p values. The combination of Eqs. 1.9 and 1.15 to take into account increasing drop viscosity and diameter ratio becomes:

$$We_{FC/SS} = \frac{We_{ss}}{5.24\beta^2} \frac{\left\{1+\Delta^{-2} - (1+\Delta^{-3})^{2/3}\right\} (1+\Delta^{-3})^{11/3}}{\Delta^{-6} (1+\Delta^{-1})^2} \quad (1.16)$$

This model predicts the SS region boundary quite well for water droplets in Figs. 1.11 and 1.12 and reflects the independency of the gas properties on the outcome boundary. Figure 1.6 illustrates the dependence on the droplet diameter ratio and reasonableness of this model for the FC/SS boundary. The dependence of Oh_p on this boundary is shown in Figs. 1.7 and 1.8 yielding reasonable agreement, though some of the nomograms contain overlapping coalescence and separation outcomes, making the boundary difficult to identify. As noted earlier, this difficulty is attributed to uncertainty in the individual drop test conditions and indicates that the above model is only approximate.

1.3.3. The B/FC Boundary:

To model the boundary between bouncing and fast coalescence, it is important to identify the liquid and gas properties that primarily influence the intercept value (We_B) obtained from the experimental data. The primary physics of the interaction is inviscid, and thus controlled by a critical Weber number. As the droplets start to interact (but before any coalescence may have occurred), the droplet surfaces flatten out next to each other leading to nearly disk-like surfaces separated by a thin gas film at the collision plane. If the interfaces have small instabilities, they can come into direct contact and cause the two interfaces to merge. If fast coalescence occurs, these interfaces fully merge before the drops rebound away from each other. This merging phenomenon converts the kinetic energy of the droplets into surface energy, and this criterion can be used to determine the critical Weber number (We_B) for inviscid conditions.²

However, droplet viscosity and gas effects may also affect the B/FC boundary that is represented as the thin solid black line in the nomograms. The strongest influence for this transition is due to droplet viscosity which can be readily observed by considering trends in the We_B (head-on collision intercept for this transition). From Figs. 1.7 and 1.8, an increase in the We_B (for a fixed gas conditions) correlates with high droplet viscosity (μ_p). This trend is also seen from other experiments of Qian & Law⁴ when comparing water droplet collisions with and tetradecane collisions and by the experiments of Jiang *et al.*¹¹ for hydrocarbon droplet collisions with increasing droplet viscosity.

By taking into consideration of the physics of droplet bounce and the qualitative observation of the experimental data, it was found that droplet viscosity effects controlled the boundary modification for head-on collisions ($\beta=0$), but that gas viscosity effects also became important for angled conditions ($\beta>0$). This suggested a layered analysis to better model the boundary. In order to quantify the droplet viscosity effect for head-on impacts, the critical Weber number at

$\beta=0$, We_B is plotted as a function of the Oh_p in Fig. 13a for all the cases at 1 atm pressure environment to eliminate the effect of the gas. The results clearly demonstrate that increasing droplet viscosity tends to increase this critical Weber number, which is consistent with increased stabilization through viscosity preventing coalescence so that the drops are more likely to bounce. However, the experimental data also shows but We_B tends to reach a maximum value of 27 at very high Oh_p values, indicating that at these high velocities the viscosity effects are no longer sufficient to dampen the instabilities which lead to coalescence. These trends were modeled as:

$$We_B = \min[700Oh_p + 7, 27] \quad (1.17a)$$

This expression provides a very good prediction except for the case at $Oh_p=0.09$, which is for the droplets of 30% pvp in air. However, the 30% pvp droplets included solid particle contents in the droplets after mixing which could serve as a contaminant and explain the over-prediction of the critical Weber number for that specific case.

The next step was to identify the gas effects for angled collisions. A close analysis of both the gas pressure and density for the available data indicated that the gas density had a much more consistent impact on the boundary.

Figures 1.11 & 1.12 independently indicate that $We_{B0.5}$ increases with gas density for a fixed gas species and liquid type. In addition, comparing Figs. 1.11a to 1.12a and Figs. 1.11b to 1.12b, also indicates that $We_{B0.5}$ generally increases with gas density. To determine the possible mechanism for this effect one must consider the controlling non-dimensional numbers. As can be seen from Table 1, the gas viscosity was nearly constant for all the tests, thus changes in gas density would modify the Reynolds number and Ohnesorge number for the gas and, in turn, change in the relative influence of gas viscosity. Assuming that the liquid velocity drives the gas

velocity and that the flow length scale is the drop diameter, the corresponding gas flow Reynolds number for ambient air can be estimated as about 30 for a typical We_B value of 10. Therefore, one may expect that gas viscous effects can play a role (especially since the flow length scale of the captured gas is smaller than the drop diameter) though convective effects associated with the Weber number would be the primary driver for the collision outcome. The increase gas viscosity that leads to droplet bounce has not been fully understood yet.

In general, the impact of drop and gas viscosity was qualitatively described with the following fit:

$$We_{B0.5} = \min \left[100Oh_p \left(1 + \frac{0.08}{Oh_f} \right) + 2, 27 \right] \quad (1.17b)$$

The influence of the collision angle, β , can then be expressed using the form of Eq. (1.6) since this theoretical dependency was found to be consistent with experimental trends.⁸ The net combination of effects can thus be expressed as:

$$We_{B/FC} = \max \left[We_B, \frac{We_{B0.5}(1+\beta)}{3(1-\beta)} \right] \quad (1.18)$$

In general, the proposed model is qualitatively consistent in predicting the boundary separating the bounce and head-on separation (B/FC) boundary for most all conditions shown in the nomograms. However, it is often difficult to segregate the effects slow coalescence and bounce with bounce and fast coalescence because of uncertainty (outcome overlap) of the experimental data. Furthermore, the complex dual influence of drop and gas viscous effects suggest that the proposed empirical correlation may not be robust and that additional experiments, computations and theory are needed to understand the mechanisms that control this boundary under variable drop and gas properties.

1.3.4. The SC/B Boundary:

The boundary between slow coalescence and bounce has not been previously modeled, but it is known that droplet and gas properties are important mechanisms for this phenomenon. Since the influence of slow coalescence is highest at the head-on collision condition, we first seek a model for We_{SC} , the intercept value of this boundary.

For the slower velocities associated with this interface (with Weber and gas Reynolds numbers of order unity), the drop dynamics are more benign. As a result, the gas between the impacting drops is more likely to be captured as a semi-stagnant pocket of gas as can be noted by the simulations of Jiang²⁶ shown in Fig. 1.14. This gas capturing is a result of the drops dynamics that produce concave surfaces after impact (whereby the interface separation is greater at the centerline than at the edges). The predicted centerline thickness of gas between the drops is typically on the order of 1% of the droplet diameters, i.e. on the order of a few microns for the cases of Table 1.1. Note that the merger of the interfaces by molecular diffusion requires that the two interfaces be much closer, e.g. on the order of 0.01 microns (Q&L). This length-scale disparity suggests that slow coalescence is instead a result of interface instabilities and that bounce will occur if the instabilities are prevented. Since the thin film of gas will be more stable at high pressures, one might expect, that such conditions are more likely to yield bouncing, which is consistent with the data surveyed herein. Similarly, one would expect slow coalescence merging at low pressures, which is consistent with experimental results in vacuum conditions by Willis & Orme²² whereby bounce was not observed. At near-grazing conditions ($\beta \sim 1$), there is little experimental evidence of slow coalescence occurring even at very low Weber numbers and this is consistent with a reduced likelihood of a captured thin gas layer when the impact is highly skewed.

To characterize the controlling flow instabilities for head-on collisions, one may relate the dynamics of a thin film of gas caught between two droplets with the inviscid oscillation dynamics of a compressible gas bubble in a liquid. In this case the time period of oscillations is as described Minneart time-scale²⁷:

$$\tau_{\text{Minneart}} \propto d_{\text{bubble}} \sqrt{\frac{\rho_{\text{liquid}}}{p}} \quad (1.19)$$

Approximating the trapped air diameter by the droplet diameter as shown in Fig. 1.14b ($d_{\text{trapped}} \approx d_{p-p}$), the natural frequency for oscillation^{27,28} can be approximated as:

$$\tau_{\text{osc}} \propto d_{p-p} \sqrt{\frac{\rho_p}{p}} \quad (1.20)$$

This natural frequency time-scale can be compared to the capillary time-scale²⁸ associated with liquid viscous damping of interface movement:

$$\tau_{\text{cap}} \propto \frac{d_{p-p} \mu_p}{\sigma} \quad (1.21)$$

The ratio of the respective time scales can be expressed as:

$$\frac{\tau_{\text{osc}}}{\tau_{\text{cap}}} \propto \frac{\sigma}{\mu_p} \sqrt{\frac{\rho_p}{p}} \quad (1.22)$$

A large time scale ratio would indicate high degree of instabilities that are not significantly damped (low droplet viscosity), leading to an outcome of slow coalescence which is consistent with the observed trend in experimental data. Conversely, a low ratio of the time scales would indicate that the trapped gas is more likely to be stable which in turn would result in the droplets bouncing.

By examining the available experimental data, a linear variation of this time-scale ratio was found to give a reasonable correlation of the We_{SC} trends as shown in Fig. 1.15:

$$We_{SC} = 1.15 \left(\frac{\sigma}{\mu_p} \sqrt{\frac{\rho_p}{p}} \right) = \frac{1.15}{Oh_p} \sqrt{\frac{\sigma}{pd}} \quad (1.23)$$

The correlation of Fig. 1.15 appears to be quite strong indicating that this effect is significant for the current conditions. In contrast, the capillary, Mach and Knudsen numbers (as suggested by Bach *et al.*⁷) were also investigated but did not robustly correlate the observed experimental trends surveyed herein. This lack of correlation is consistent with the conditions investigated which focused on drops of several hundred microns (200-400 μ m) with a $Kn < 10^{-3}$, $Ma < 10^{-2}$ and $Ca < 10^{-4}$.

To approximate the relationship of the SC/B boundary for a general collision angle, the experimental variations were considered. These indicated that slow coalescence did not occur for grazing conditions ($\beta=0$) and that the boundary tended to decrease monotonically with β . Since the data was relatively scarce and limited, a linear variation was employed:

$$We_{SC/B} = We_{SC} (1-\beta) \quad (1.24)$$

The SC/B boundaries from Eqs. (1.24) and (1.25) were predicted for all the data of Table 1 and are shown in Figs. 1.7, 1.8, 1.11 & 1.12. The prediction of current model for various droplets and gases at high pressure environment is good. However, this simple variation is empirical, and further investigation is warranted to determine a theoretically founded basis for these trends.

The only distinct mis-prediction for the present model from Eqs. (1.23) and (1.24) is the case of the tetradecane droplets in ethylene at 8 atm (Fig. 1.17a) and as also shown in Fig. 1.13. For the one case, the model dramatically under-predicts the intercept Weber number by an order of magnitude. This anomaly was suggested to be a result of hydro-carbon vapor concentration by

Estrade *et al.*⁹ who expected that the same large effect would occur in terms of humidity for water drops. However, Ochs III *et al.*¹⁵ investigated water droplets at different relative humidities and saw only a minor effect in terms of collision outcome. This is evidenced by Fig. 1.15 for which relative humidity levels of 34% and 95% (saturated conditions) yielded little difference in the slow coalescence boundary. This suggests another mechanism is the primary cause for the increase in We_{SC} .

One possibility is that the high pressure (8 atm) for this case coupled with slight temperature differences may have caused the ethylene vapor to partially condense forming a thin liquid ethylene film around the tetradecane droplets. In this case, the slow coalescence process would be controlled by ethylene's surface tension (as opposed to that of tetradecane). If one were to assume the presence of such a liquid film by encapsulation, the predicted We_{SC} would be much higher. Based on these assumptions, the present model (denoted by the blue line) indeed agrees well with the experimental data as shown in Figs. 1.13 and 1.17a. To further support this conclusion, it should be noted that any condensation due to humidity on a water droplet would not change the surface tension, which is consistent with the lack of a change shown in Fig. 1.15. However, it is noteworthy that all the experimental data considered herein included liquids and gases at room temperature. If a diffusion principle is dominant, then one may expect temperature effects could be significant indicating that the empirical factor of Eq. (1.24) is not necessarily a constant.

1.3.5. Other Effects (and Limitations of the Proposed Models)

Besides the uncertainty of the experimental data (which translated into uncertainties in the coefficient and functional relationships as discussed above), it is important to note that the experimental data considered and the associated models do not include non-continuum effects, chemical reaction, heat transfer, electric charge, nor changes in the temperature of the gas or the

droplet.

In addition, the conditions do not include pre-collision shape effects (Willis & Orme²² investigated the collision of ellipsoidal drops, which can be quite complex as compared to that of their spherical counterparts). This can be an issue at significant aerodynamic Weber numbers ($We_f > 1$ where droplets become non-spherical prior to collision. The aerodynamic Weber number can be related to the impact Weber number in terms of the density ratio: $We_f = \rho_f v_p^2 d / \sigma = We_{p-p} (\rho_f / \rho_p)$). However, an initially spherical droplet which has recently undergone coalescence or separation will be significantly non-spherical after the interaction until the shape oscillations damp out. Therefore, an ensuing secondary collision could involve non-spherical collisions even when the aerodynamic Weber number is small.

Other issues not modeled include effects of temperature gradient. In particular, Neitzel & Dell'Aversana²³ noted that the critical pressure for coalescence (related to the drop vapor emission) decreases with increasing temperature gradient. The presence of surfactants, which can inhibit coalescence, is another issue. Models for coalescence rates especially in contaminated systems is still quite empirical due to the complexity of the drainage nanophysics.²¹ Finally, the segmental parameter noted in Fig. 1.13 for the boundary between bouncing and fast coalesce suggest competing effects may be present indicating a single non-dimensional parameter to describe both the pressure and viscous effects may not be sufficient. Thus, significant further research (experiments, theoretical analysis, and detailed interface-resolving numerical simulations) for a variety of test conditions are warranted to more fully understand and quantify the collision mechanism details and to better model the outcome boundaries.

1.4 Conclusions

The four prediction boundaries characterizing drop-drop collisions were investigated with

respect to the viscous effects of the droplet and surrounding gas properties as a result of a comprehensive survey of experimental data. Previous models based on deformation dynamics and were considered for various droplets and gas environments that may be of interest for combustion sprays under pressure. In general, the inviscid dynamic primarily governed the deformation (consistent with Weber and Reynolds numbers much greater than unity for the conditions surveyed), but secondary effects were found to be still quite important.

The FC/RS and FC/SS boundaries are sensitive to the viscosity of the droplet and the drop size ratio and generally insensitive to the surrounding gas properties. A revised model was proposed for both of the two boundaries that provides better prediction including the highly viscosity drops. However, the physics become more complex for the B/FC and SC/B boundaries that occur at slower speeds. At the speeds where the impact distortions are weakest, the SC/B boundary results and a qualitative model indicate a stabilizing influence of gas pressure and droplet viscosity based on a captured pocket of gas between the drops, whilst suggesting a negligible influence of relative humidity or vapor pressure.

Table 1.1 Gas and liquid properties (“TD” refers to tetradecane and “PVP” refers to polyvinylpyrrolidone).

Data source	d_{small} (μm)	Δ	Liquid	ρ_p (kg/m^3)	$\mu_p \times 10^{-6}$ (kg/m-s)	σ (N/m)	Gas	$\mu_f \times 10^{-6}$ (kg/m-s)
Q&L	300	1	Water	1000	1002	0.073	Nitrogen	17.4
Q&L	300	1	Water	1000	1002	0.073	Helium	19.4
Q&L	300	1	TD	773	2300	0.027	Nitrogen	17.4
Q&L	300	1	TD	773	2300	0.027	Helium	19.4
Q&L	300	1	TD	773	2300	0.027	Ethylene	9.6
Estrade	200	0.5, 1	Ethanol	789	1166	0.022	Air	18.2
A&P	300	0.5-1	Water	1000	1002	0.073	Air	18.2
Jiang	300	1	Heptane	680	400	0.021	Air	18.2
	300	1	Decane	726	900	0.024	Air	18.2
	300	1	Dodecane	755	1450	0.025	Air	18.2
	300	1	TD	773	2300	0.027	Air	18.2
	300	1	Hexadecane	780	3350	0.027	Air	18.2
Ochs	304	0.5-1	Water	1000	1002	0.073	Air, Vapor	18.2
Law	214	1	TD	773	2300	0.027	Air	18.2
Gotaas	350- 356	1	Monoethyleneglycol	1113	2181	0.051	Air	18.2
	351- 364	1	Diethyleneglycol	1118	3826	0.050	Air	18.2
	357- 375	1	Triethyleneglycol	1125	4794	0.047	Air	18.2
Kuschel & Sommerfeld	370	1	Water	1000	1002	0.073	Air	18.2
	370	1	Ethanol	790	1166	0.022	Air	18.2
	370	1	Propanol	803	2000	0.024	Air	18.2
	370	1	Hexanol	814	4300	0.026	Air	18.2
	370	1	Heptanol	820	7400	0.027	Air	18.2
	370	1	Nonanol	828	12900	0.028	Air	18.2
	370	1	Dodecylalcohol	831	15900	0.030	Air	18.2
	380	1	PVP - 10%	1020	2350	0.069	Air	18.2
	380	1	PVP - 20%	1046	6010	0.067	Air	18.2
	380	1	PVP - 30%	1065	15410	0.066	Air	18.2

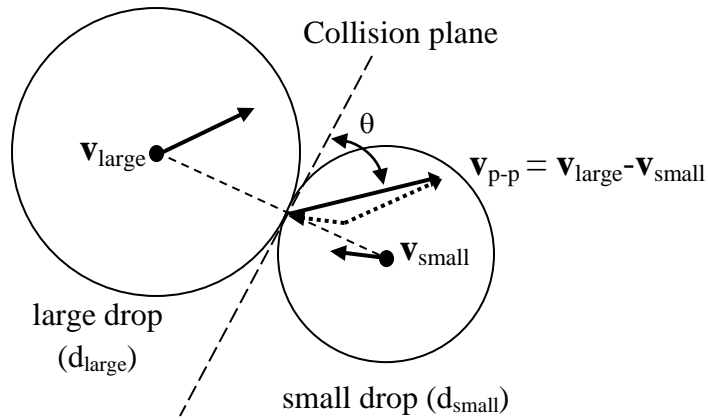


Figure 1.1 Collisional geometry between a large drop of diameter d_{large} and a small drop of diameter d_{small} , where the collision plane is tangent to their surfaces at the initial collision point. The incoming impact angle (θ) is based on the relative velocity and the collision plane and θ equals 90° for head-on collisions and approaches 0° for grazing collisions.

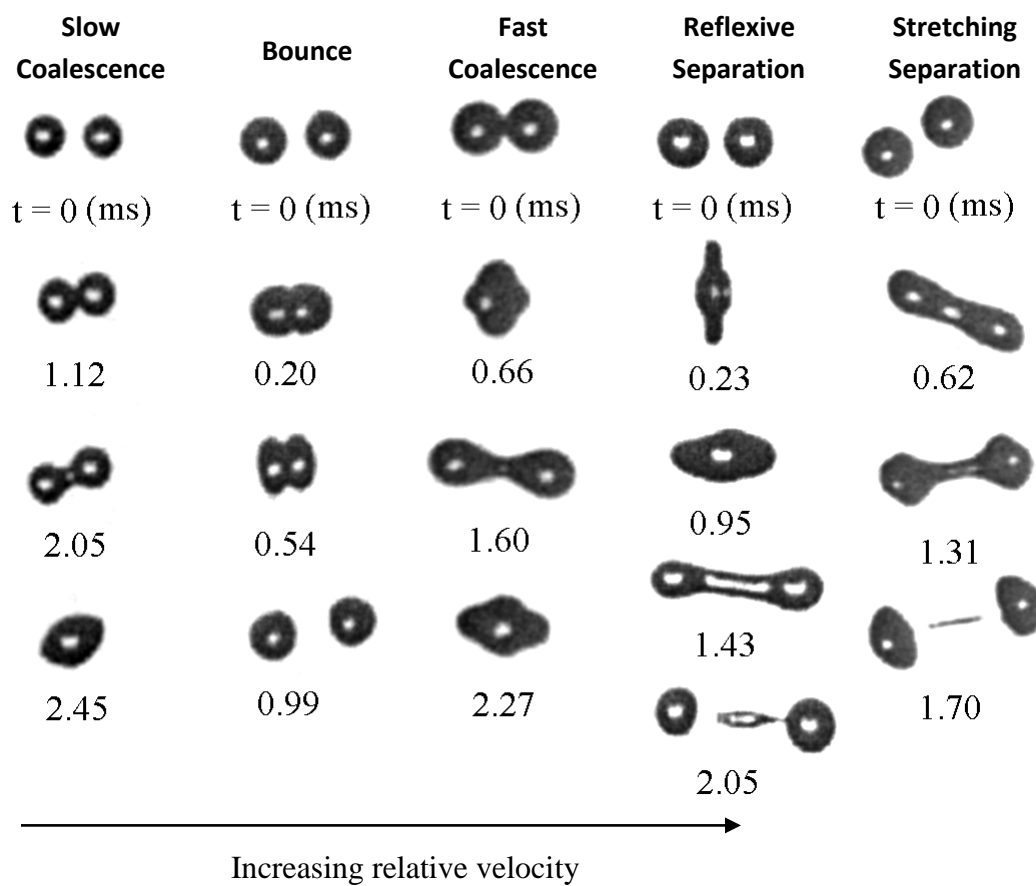


Figure 1.2 Classification of outcomes of droplet-droplet interactions based on increasing relative velocity for first four columns (Qian & Law, 1997).

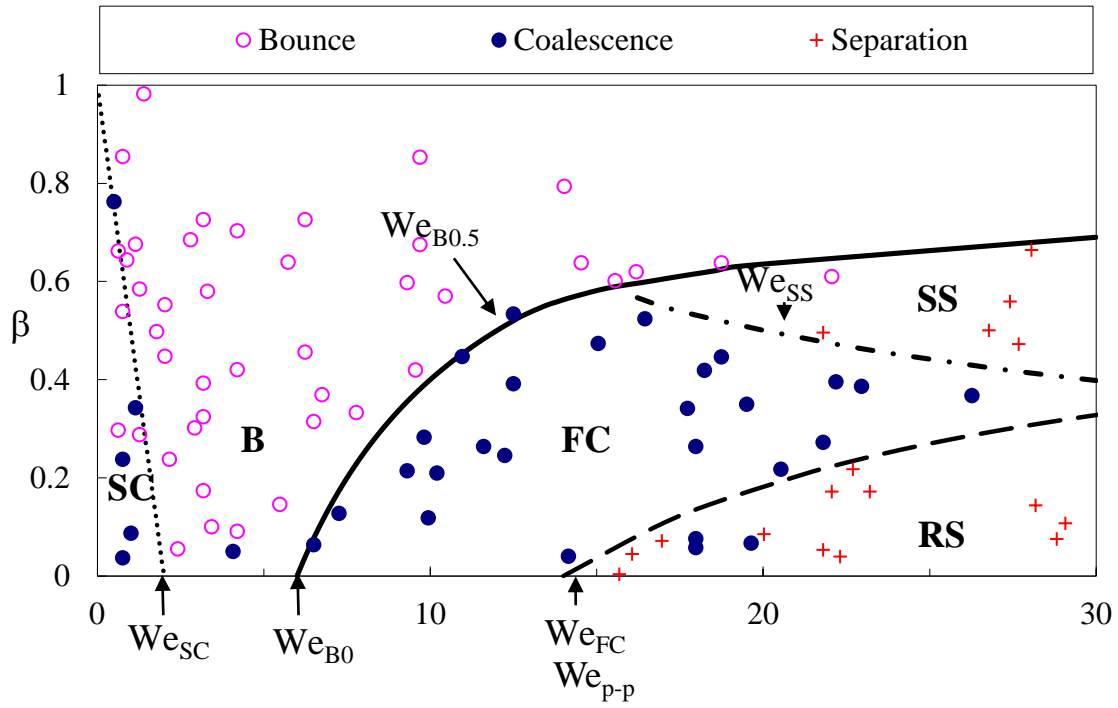


Figure 1.3 Stability nomogram of water droplet interaction in a 7.5 atm helium environment showing experimental outcomes as symbols (Qian and Law, 1997) and droplet-interaction outcome boundaries as lines based only on the experimental data (no models).

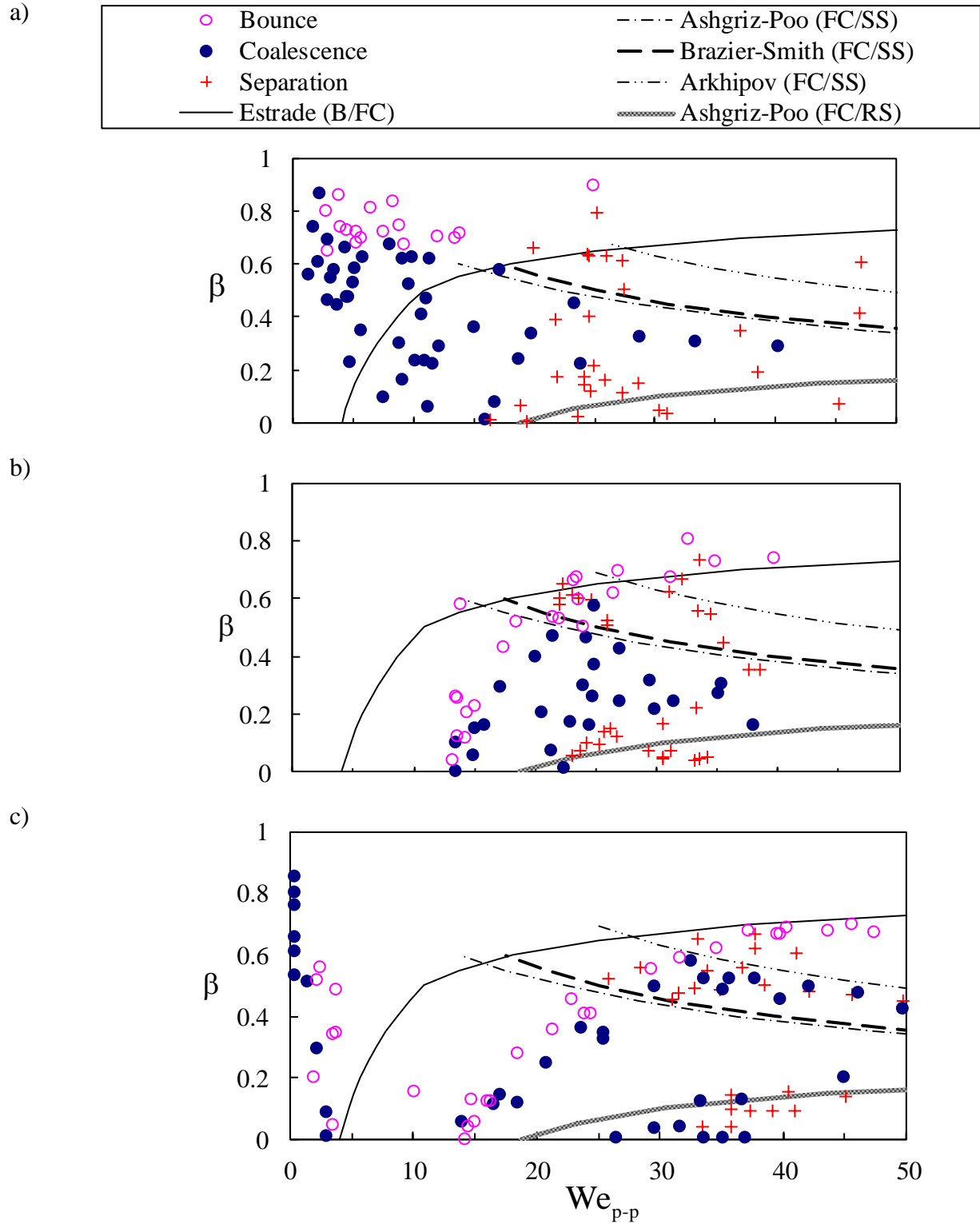


Figure 1.4 Experimental outcomes in nitrogen (Qian and Law, 1997) compared to previous prediction models of outcome boundaries for: a) water drops in 1 atm and b) water drops in 8 atm and c) tetradecane drops in 1 atm.

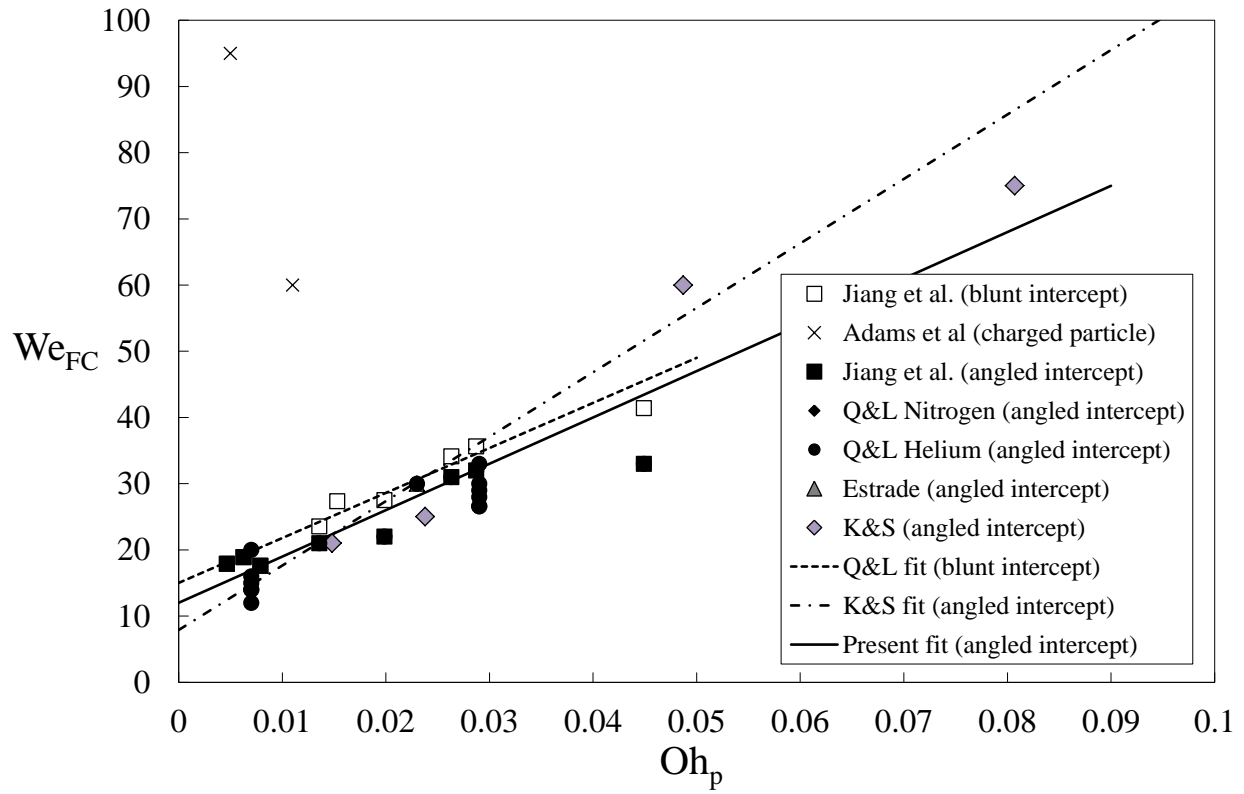
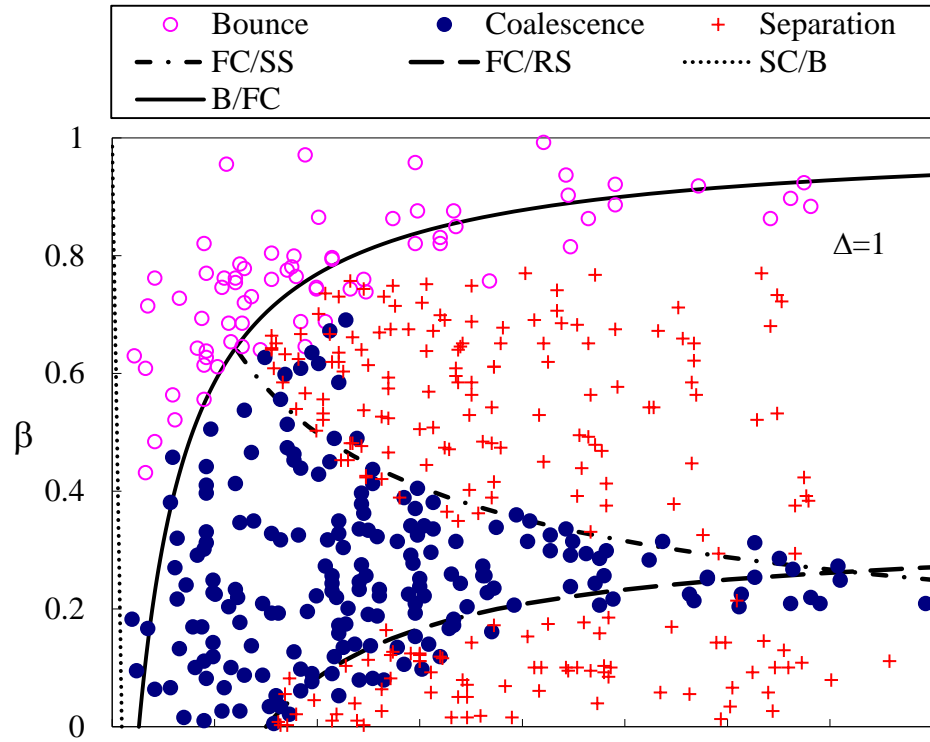


Figure 1.5 Influence of droplet viscosity on horizontal intercept between fast coalescence and reflexive separation (experiments as symbols)

a)



b)

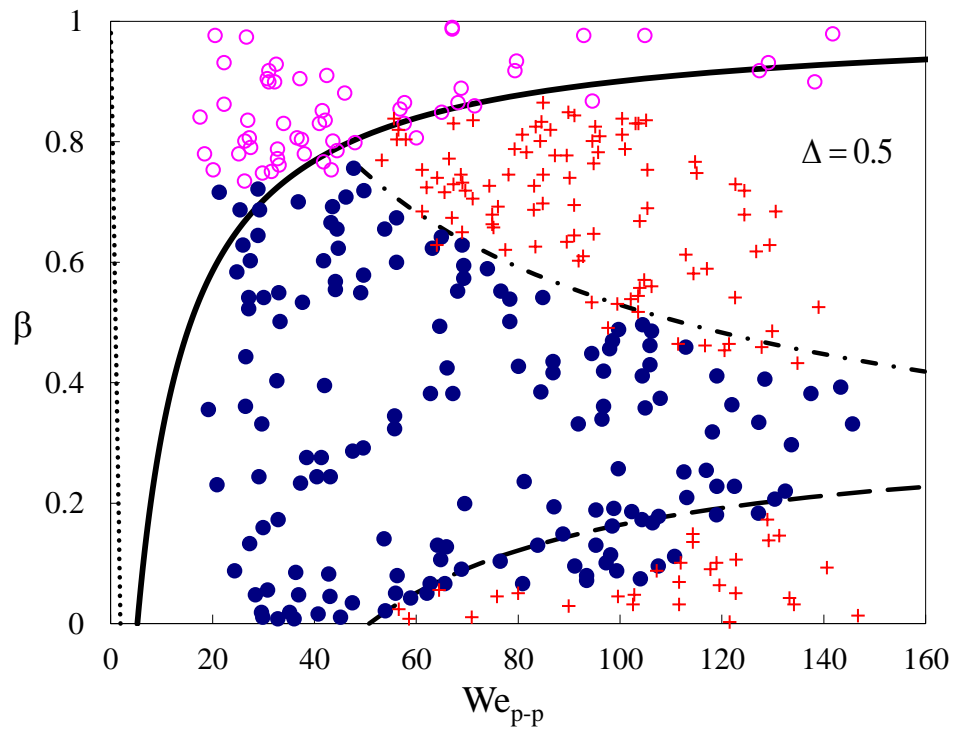


Figure 1.6 Droplet-droplet outcomes for ethanol in air at one atmosphere (Estrade *et al.* 1999) and present models for outcome boundaries.

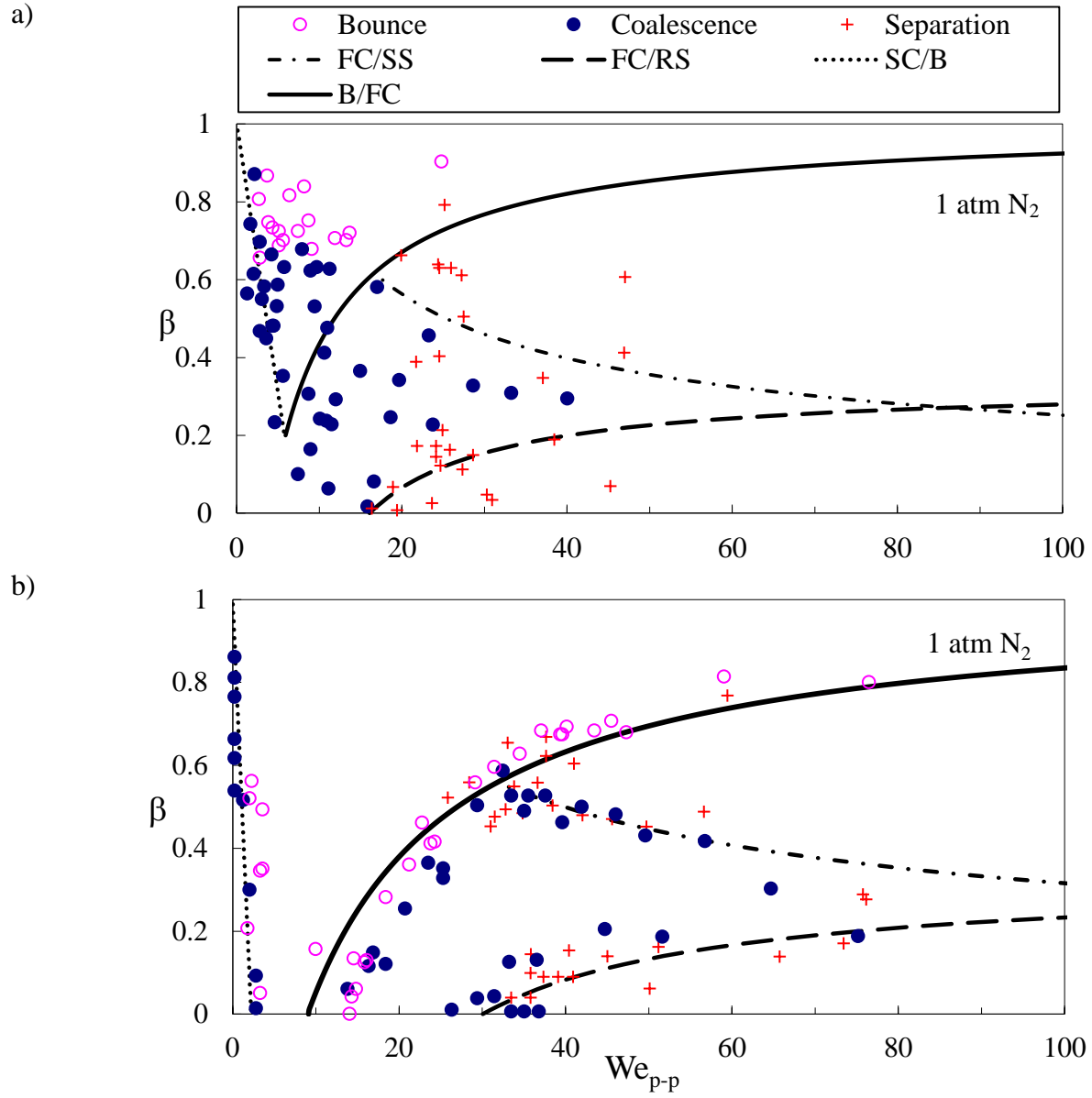


Figure 1.7 Droplet-droplet outcome boundaries for: a) water drops & b) tetradecane drops in nitrogen. (Qian & Law, 1997)

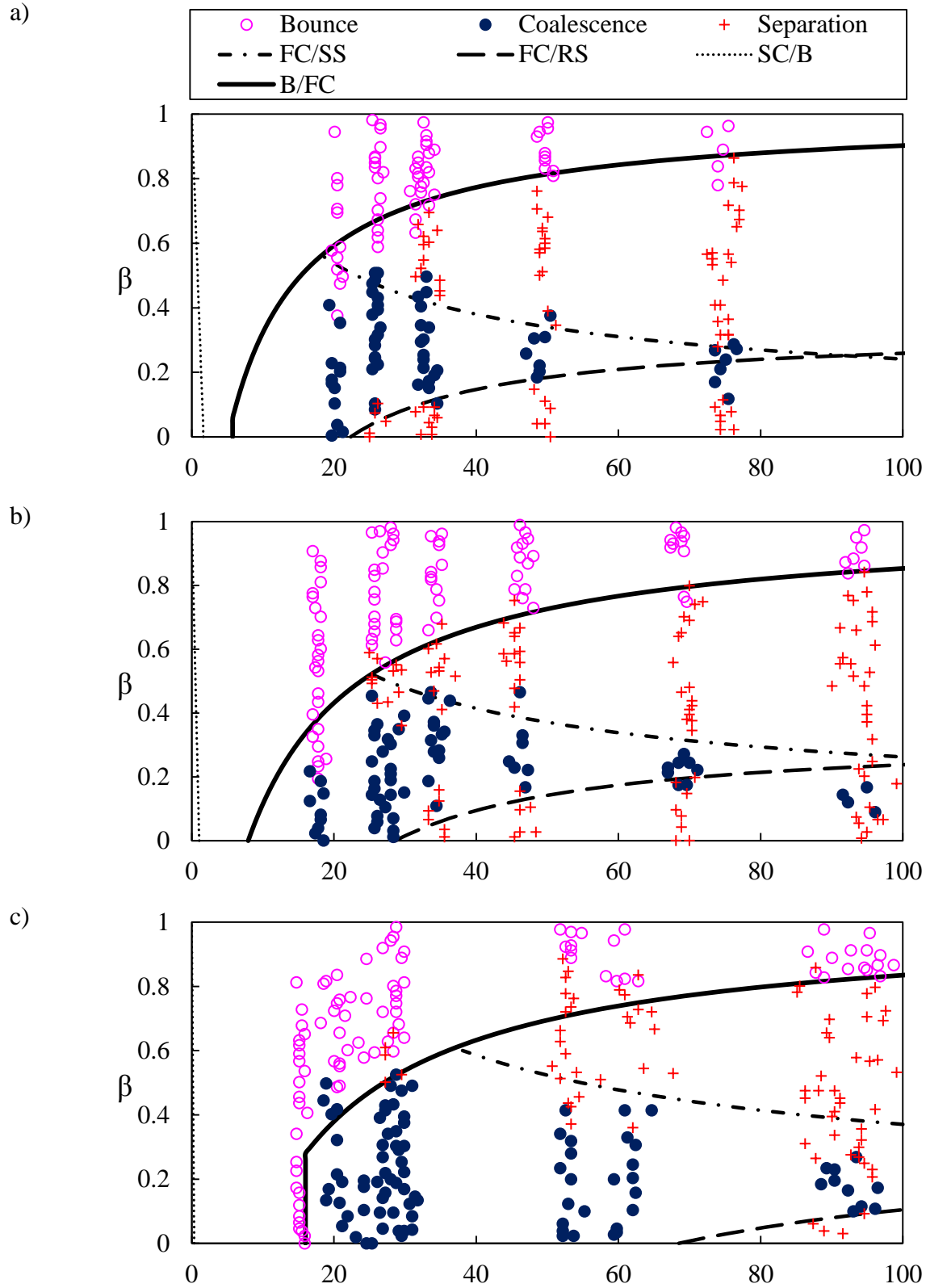
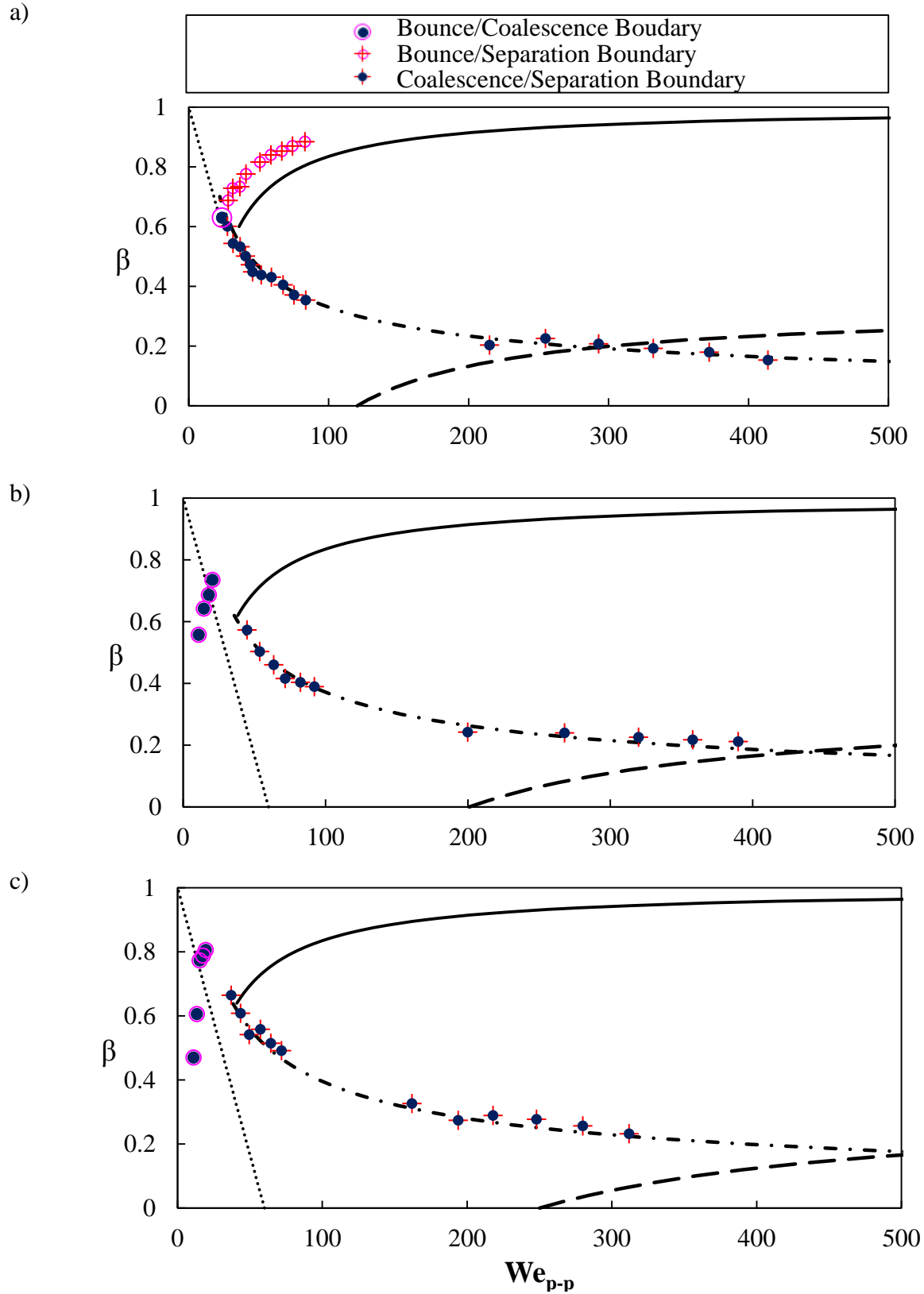
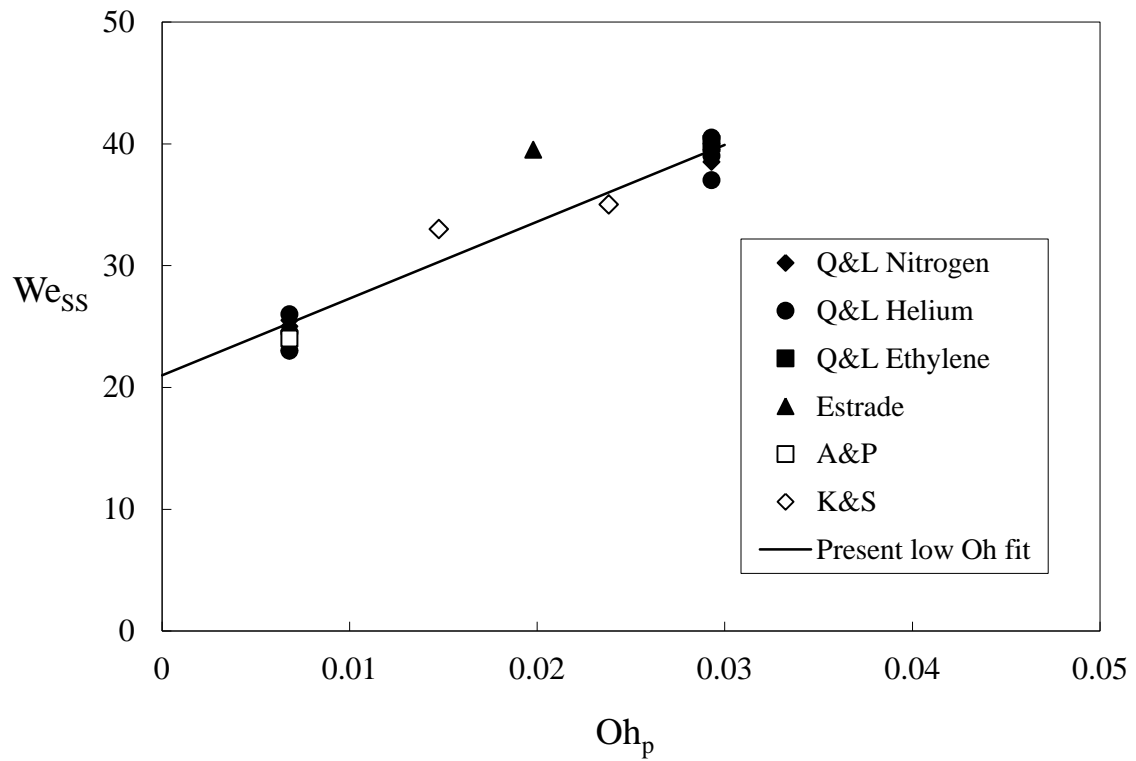


Figure 1.8 Droplet-droplet outcomes (Kuschel & Sommerfeld, 2011) compared to present models for outcome boundaries for a) ethanol, b) propanol and c) hexanol in air at 1 atm.



a)



b)

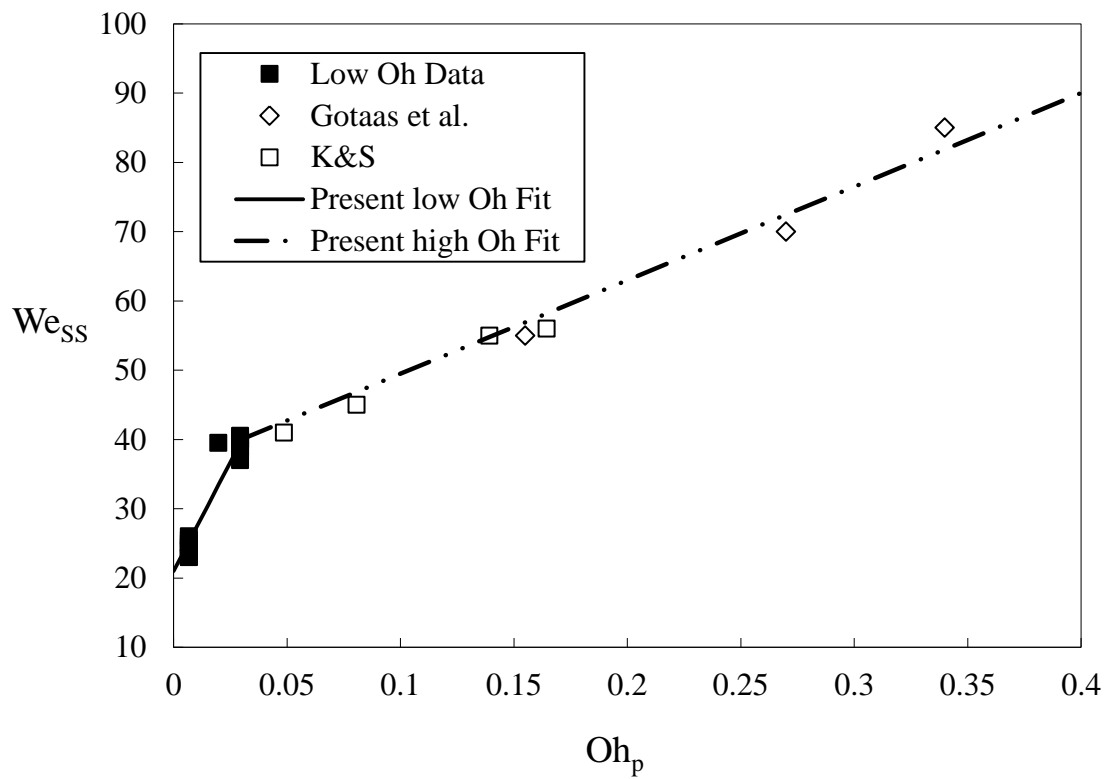


Figure 1.10 Influence of drop viscosity on horizontal intercept between fast coalescence and stretching separation for: a) low Ohnesorge drops and b) high Ohnesorge drops.

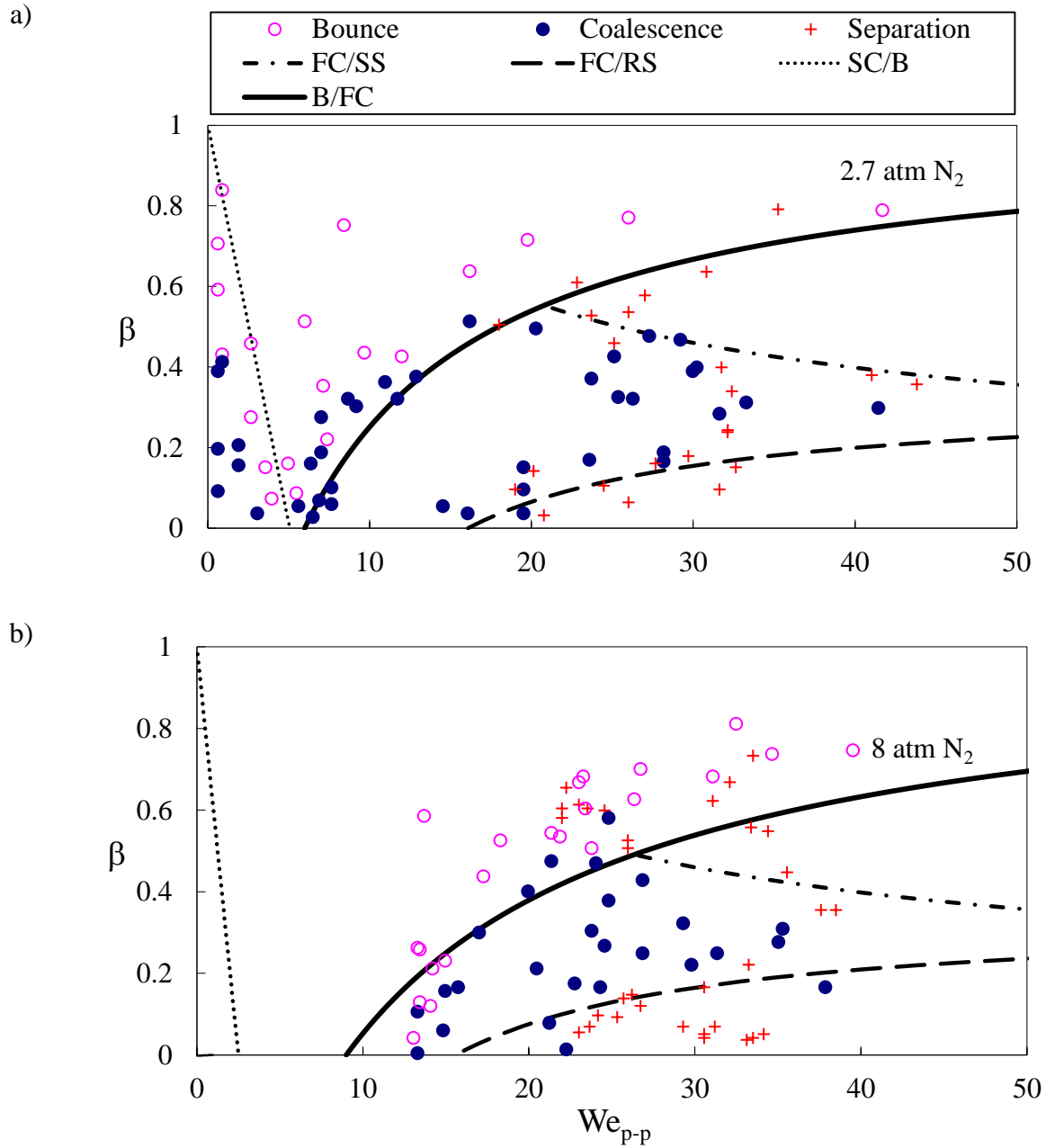
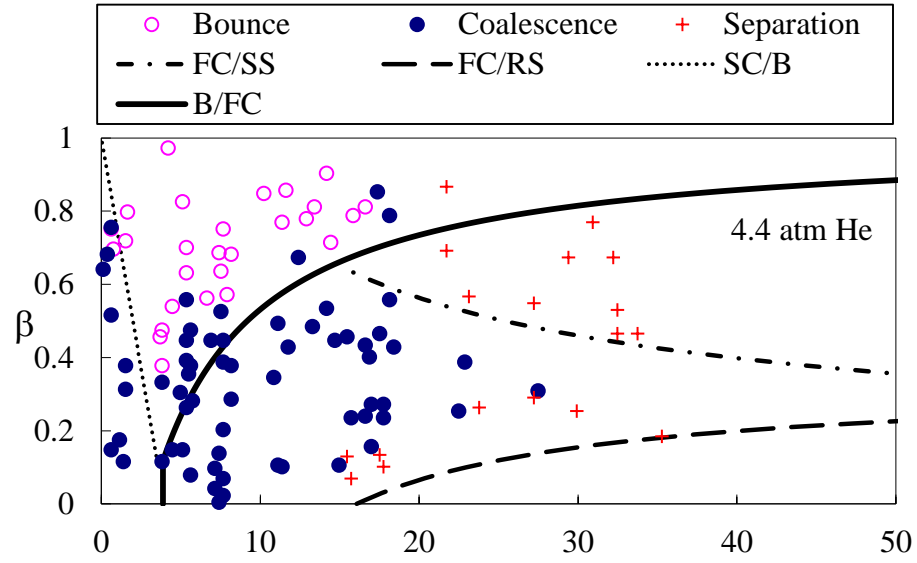
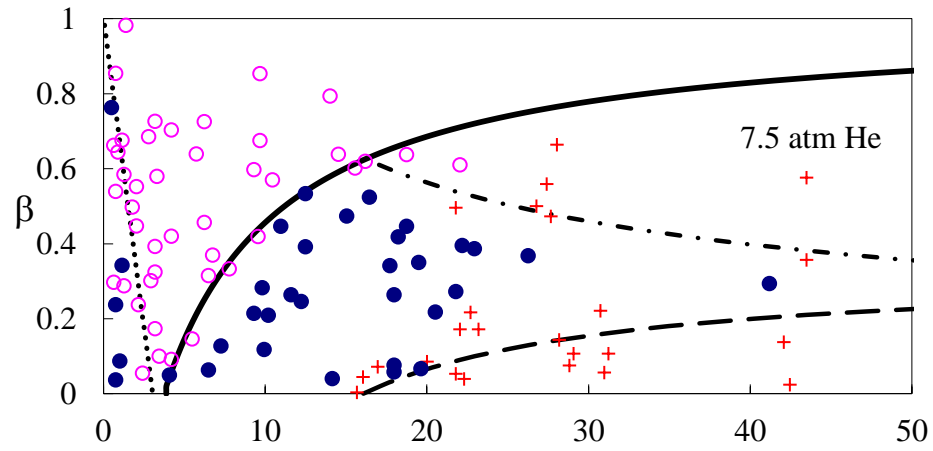


Figure 1.11 Droplet-droplet outcomes for water drops (Qian & Law, 1997) compared to present models for outcome boundaries where surrounding gas is nitrogen at: a) 2.7 atm & b) 8 atm.

a)



b)



c)

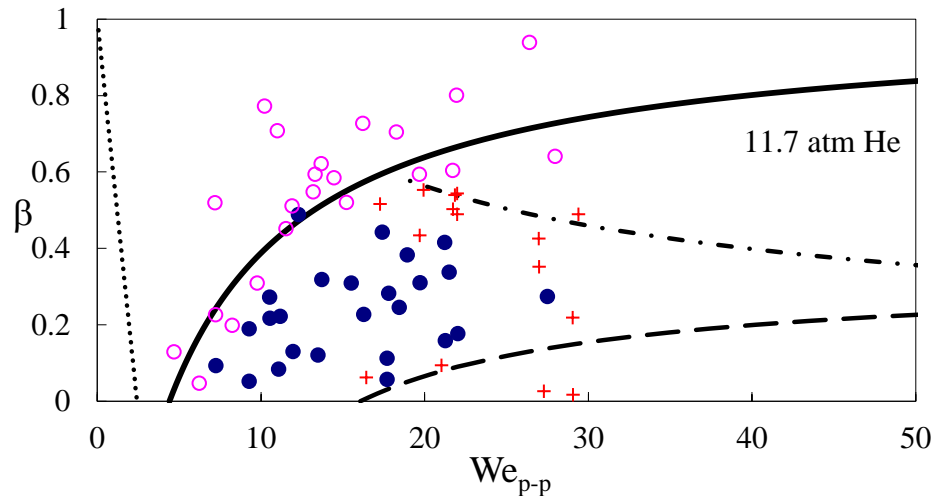
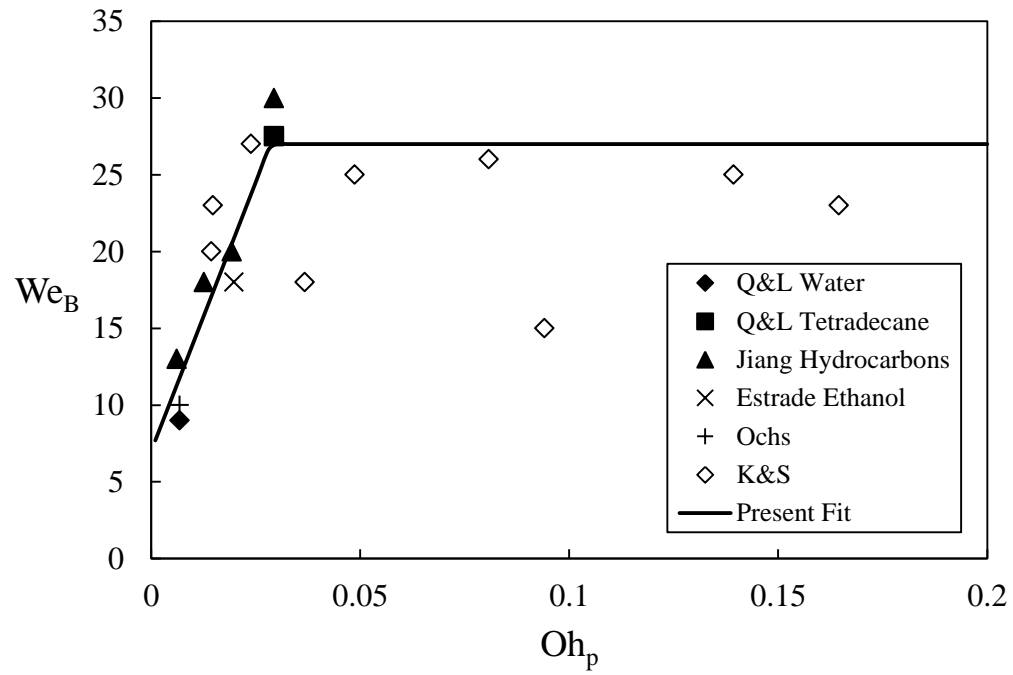


Figure 1.12 Droplet-droplet outcomes for water drops (Qian & Law, 1997) compared to present outcome boundaries where surrounding gas is helium at: a) 4.4 atm, b) 7.5 atm and c) 11.7 atm

a)



b)

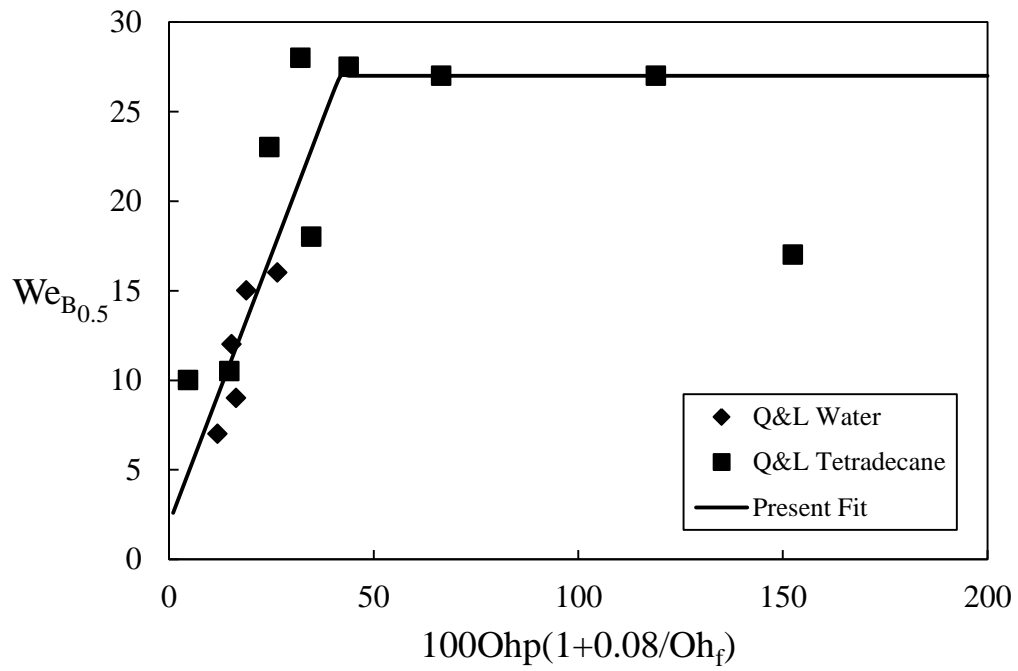
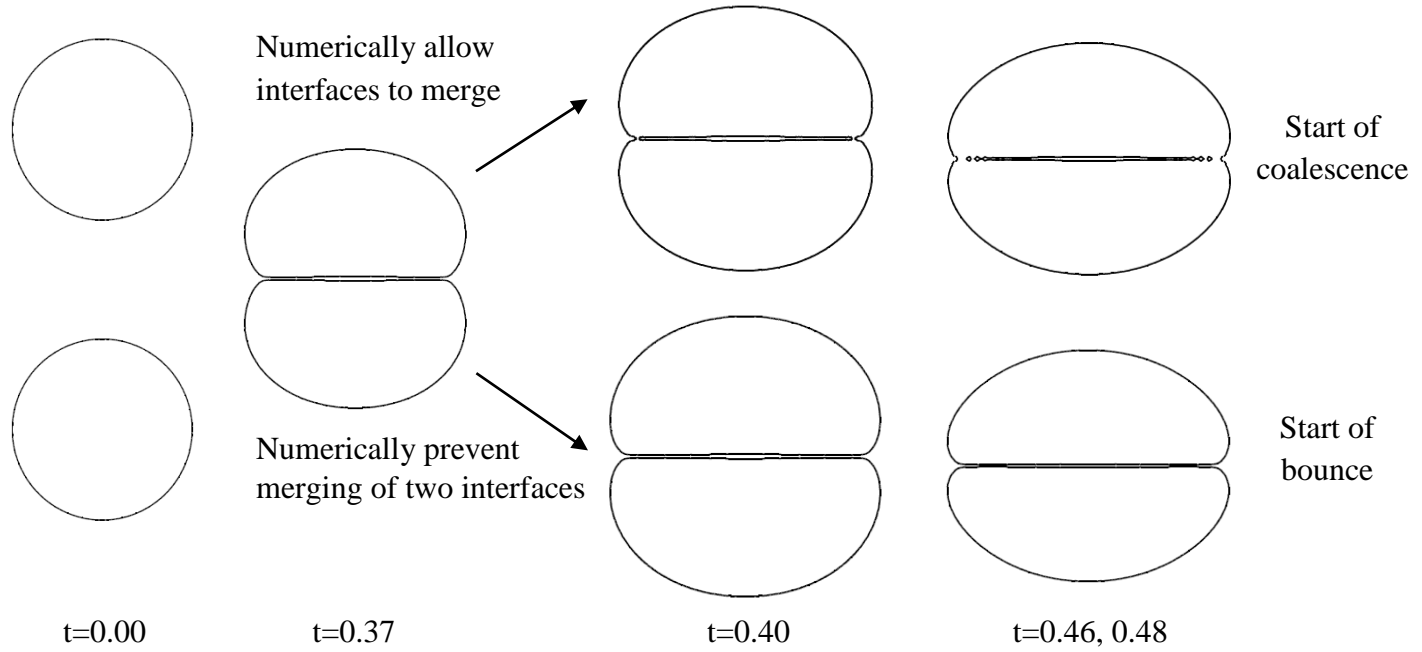


Figure 1.13 Influence of drop and gas properties on a) horizontal intercept i.e. We_{B0} b) mid-point interval i.e. $We_{B0.5}$, between bounce and fast coalescence.

a)



b)

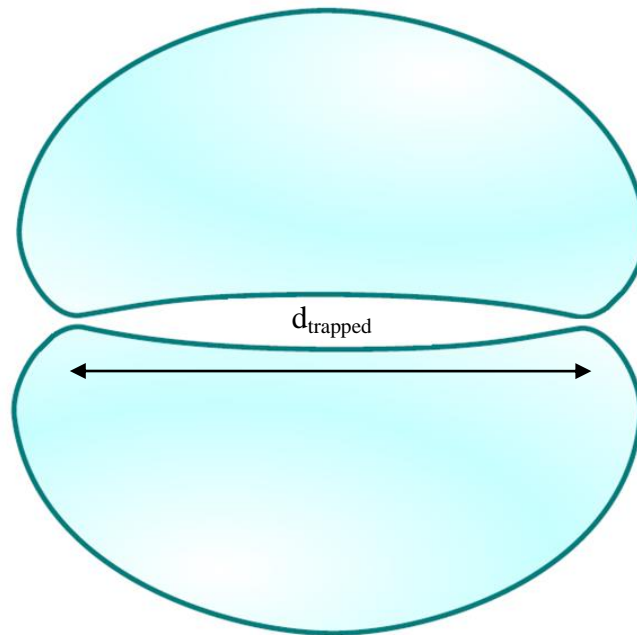


Figure 1.14 Creation of an internal bubble of gas: a) numerical evolution at $Re=We=1$ showing concave interface for drops that can create a viscously trapped gas when the interfaces are numerically prevented from merging (Jiang, 2006) and b) qualitative illustration of the thin gas bubble trapped between the droplets just after initial impact (similar to $t=0.37$ time frame from above) at higher Weber number where deformations are greater.

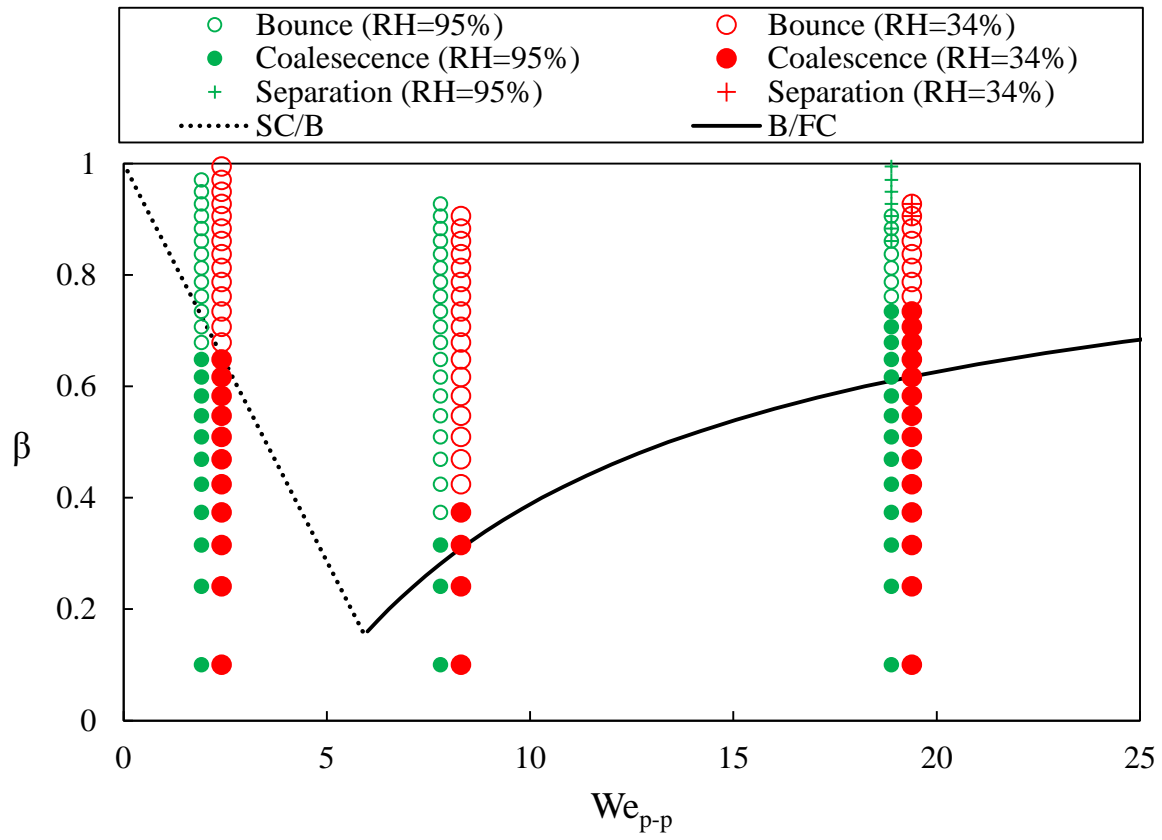


Figure 1.15 Water droplet outcomes in air at 1 atm at different relative humidity (Ochs *et al.* 1989) showing three pairs of data at two humidity levels with data artificially shifted within a pair to avoid symbol overlap. The results indicate a weak or negligible effect of humidity on the outcome, consistent with present model boundaries in lines.

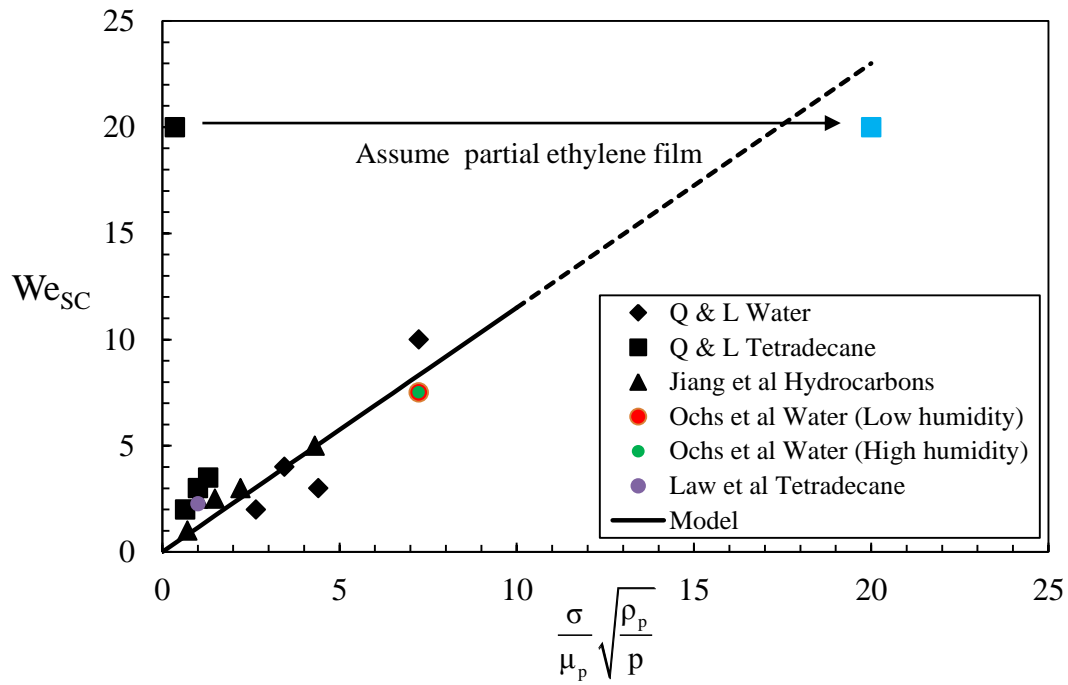


Figure 1.16 Influence of drop viscosity and gas pressure on horizontal intercept between slow coalescence and bounce, i.e. We_{SC} , where the outcome of Q& L tetradecane drops colliding in ethylene gas is also shown assuming a partial ethylene film at the interface determines the drop interaction properties (denoted by blue solid square).

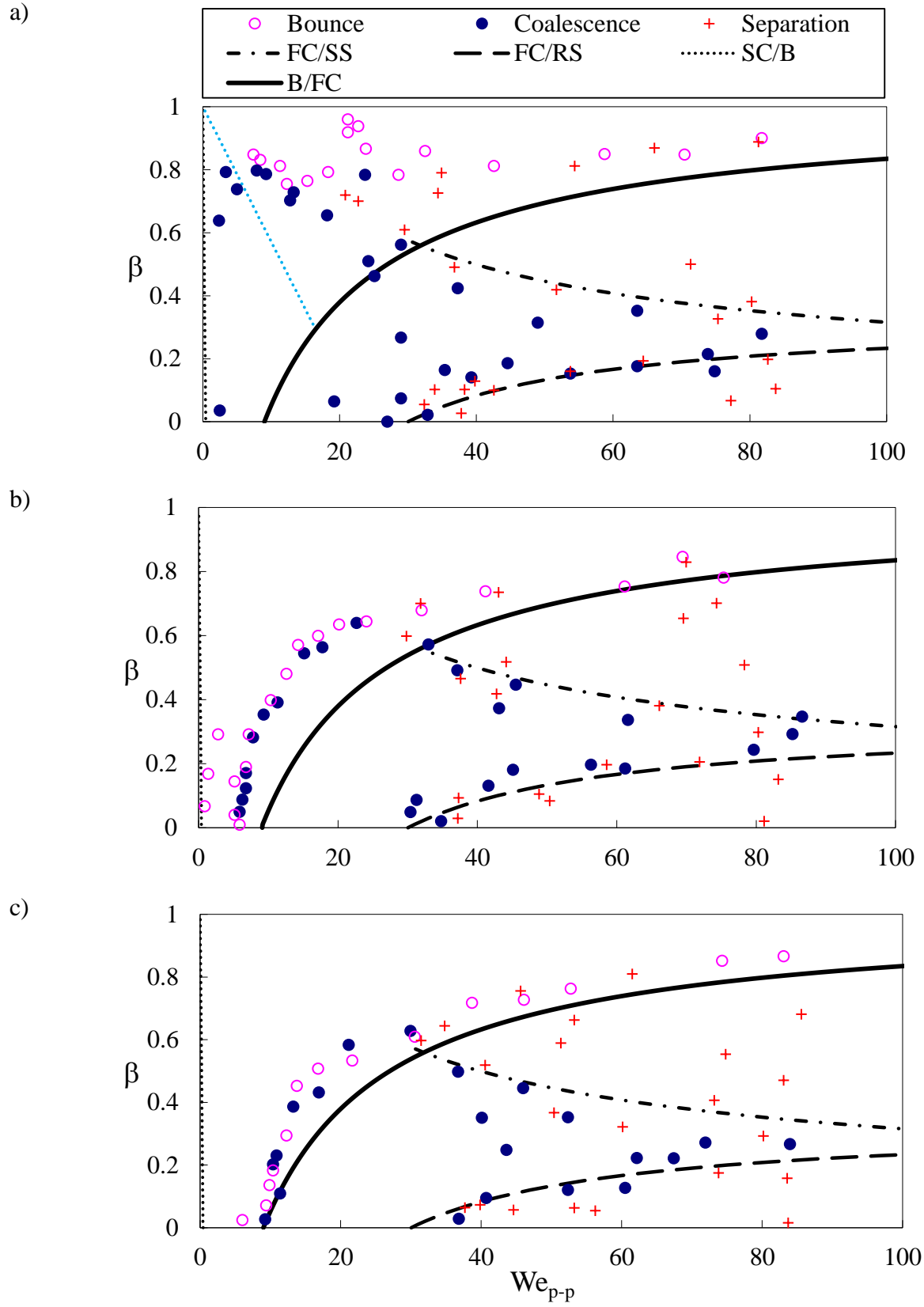


Figure 1.17 Droplet-droplet regimes for tetradecane drops in (Qian & Law, 1997) compared to present outcome boundaries for: a) 100% ethylene b) 50% ethylene-50 % nitrogen and c) 100% nitrogen in 8 atm.

1.5 Appendix

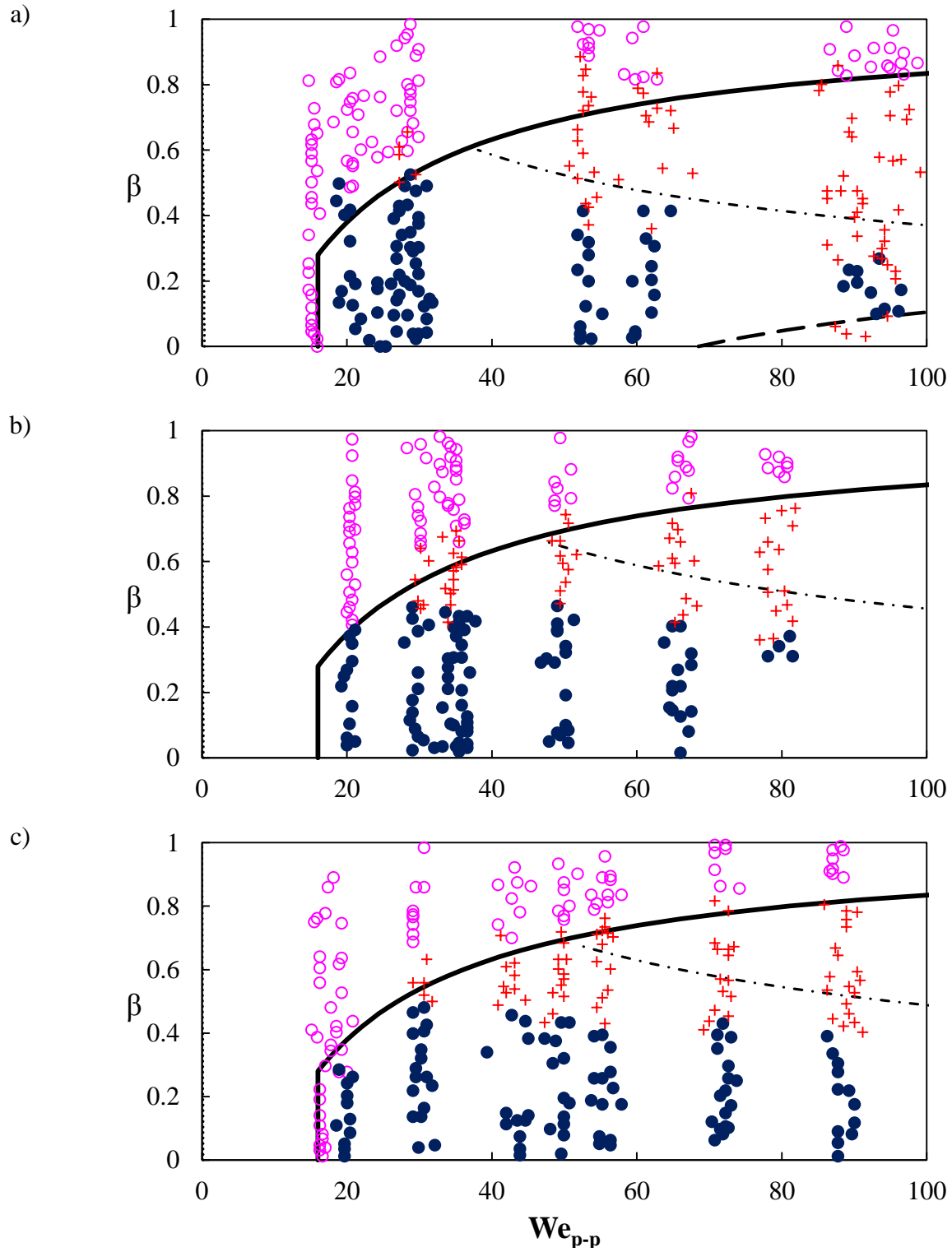


Figure 1.A.1 Droplet-droplet regimes for hydrocarbon droplets in air at 1 atm: a) heptanol, b) nonanol and c) dodecylalcohol. (Kuschel & Sommerfeld, 2011).

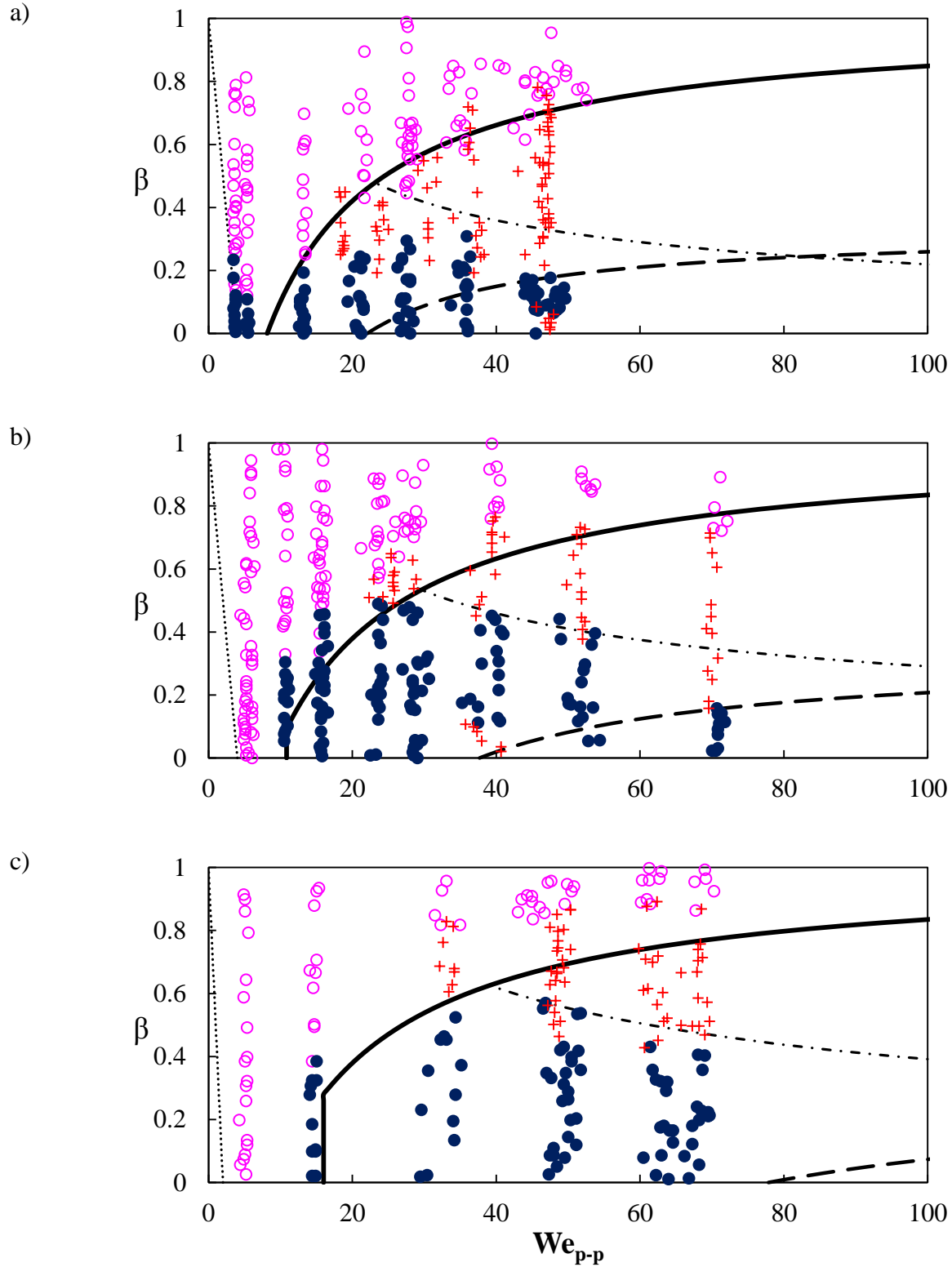


Figure 1.A.2 Droplet-droplet regimes for a) 10% pvp, b) 20% pvp and c) 30% pvp, droplets in air at 1 atm. (Kuschel & Sommerfeld, 2011).

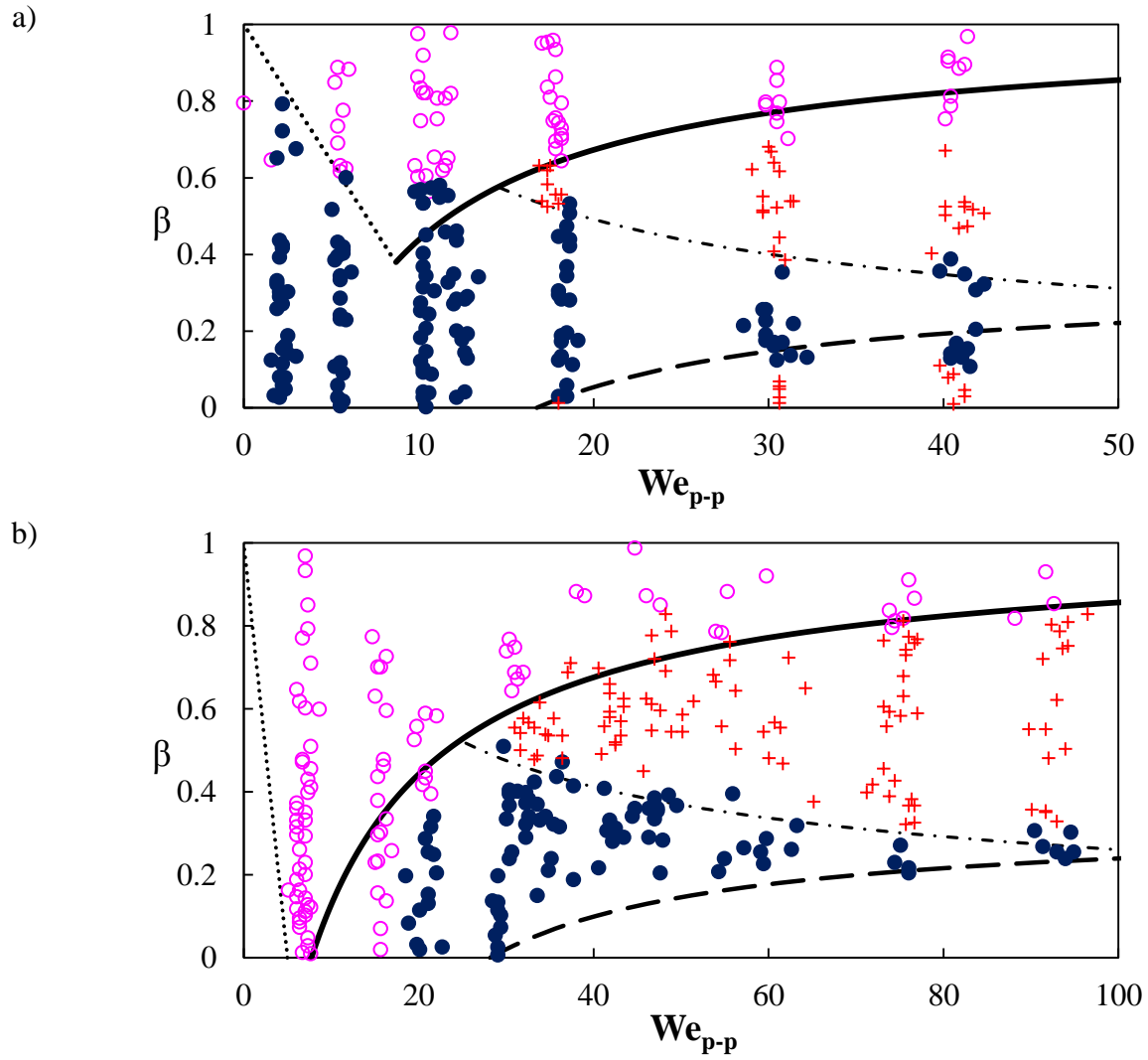


Figure 1.A.3 Droplet-droplet regimes for a) water (Kuschel & Sommerfeld, 2011) and b) diesel (Post & Abraham, 2001), droplets in air at 1 atm.

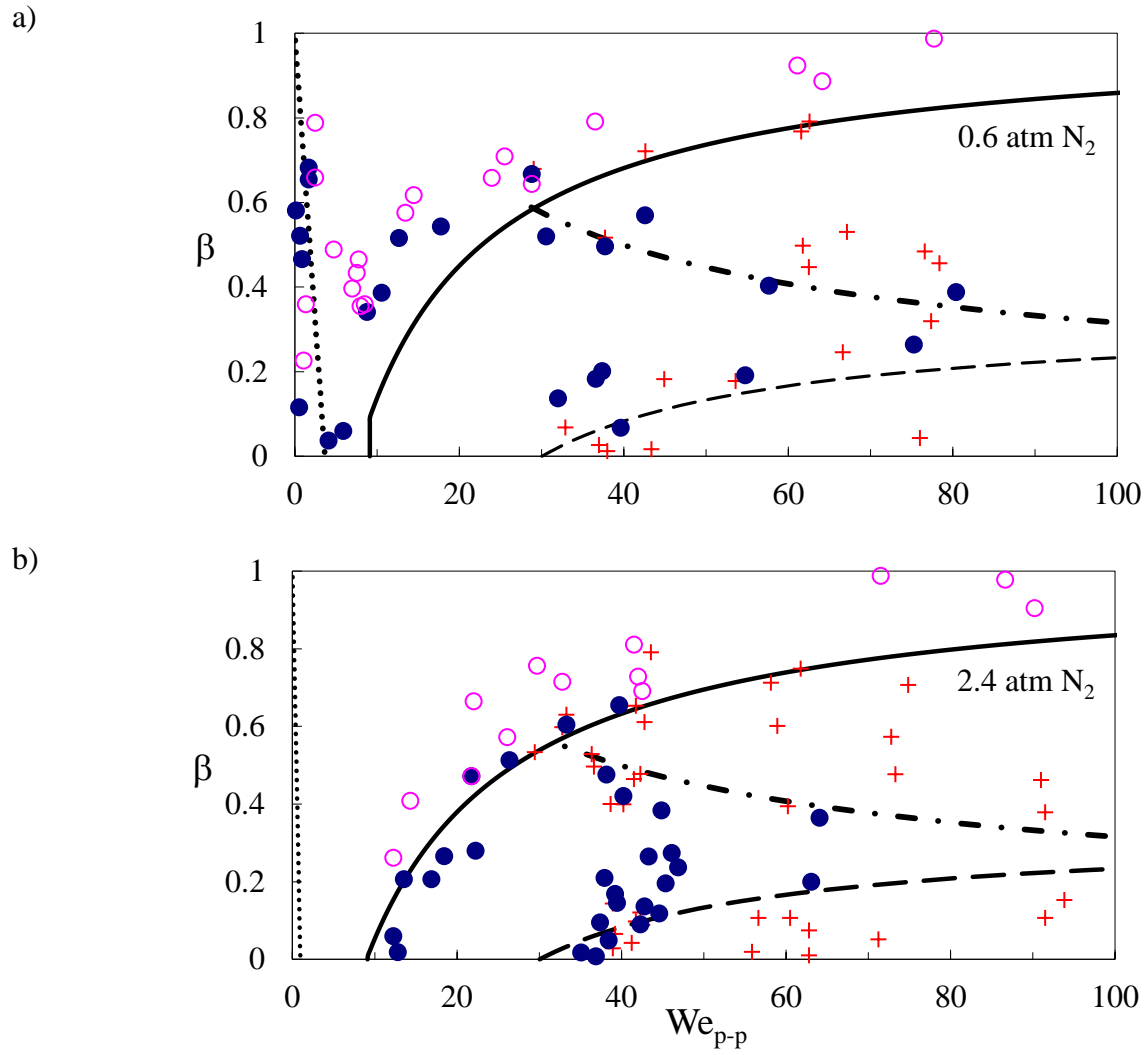


Figure 1.A.4 Droplet-droplet regimes for tetradecane droplets in nitrogen at: a) 0.6 atm, b) 2.4 atm (Qian & Law, 1997).

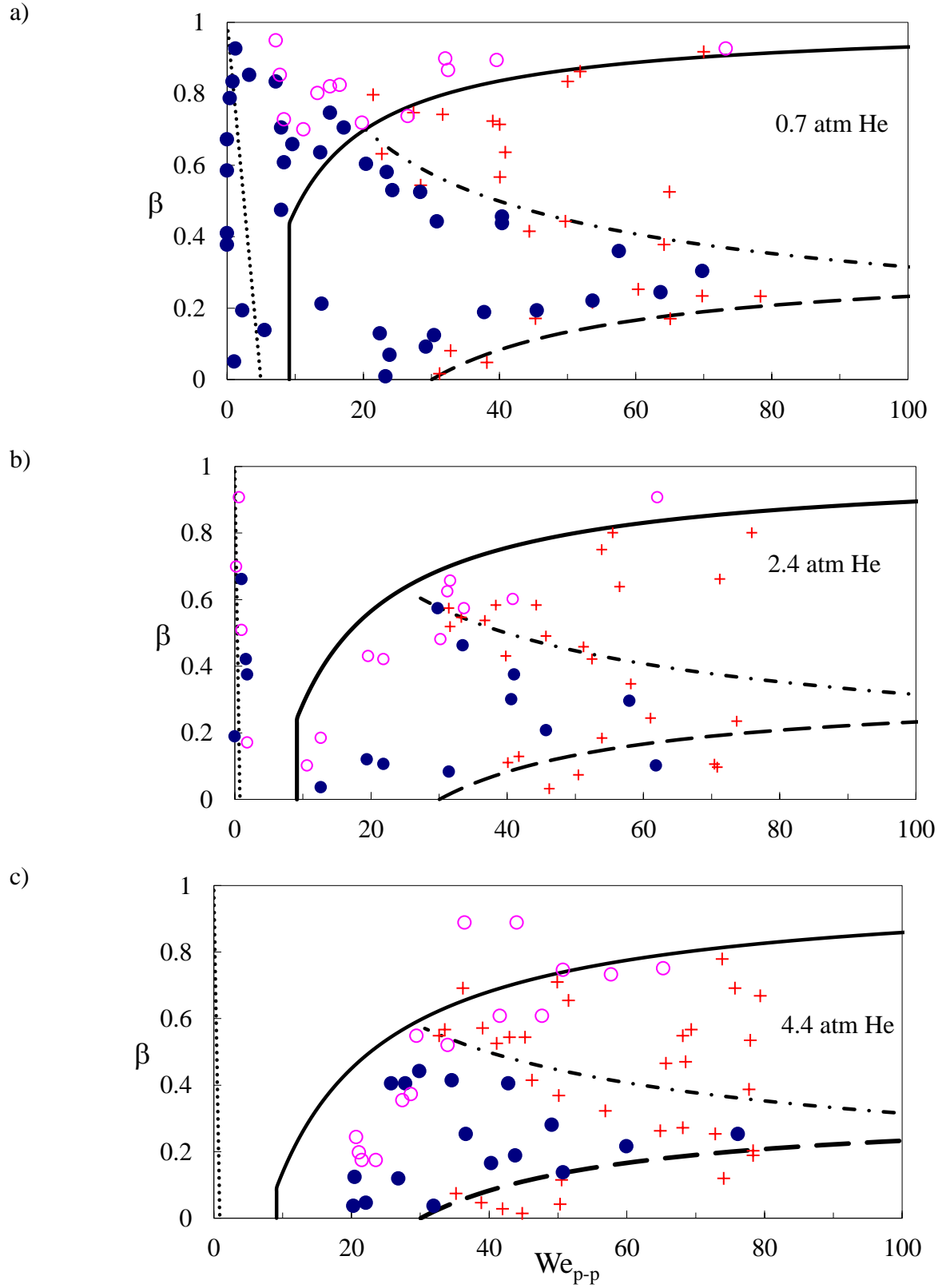


Figure 1.A.5 Droplet-droplet regimes for tetradecane droplets in helium at: a) 0.7 atm, b) 2.4 atm and c) 4.4 atm (Qian & Law, 1997).

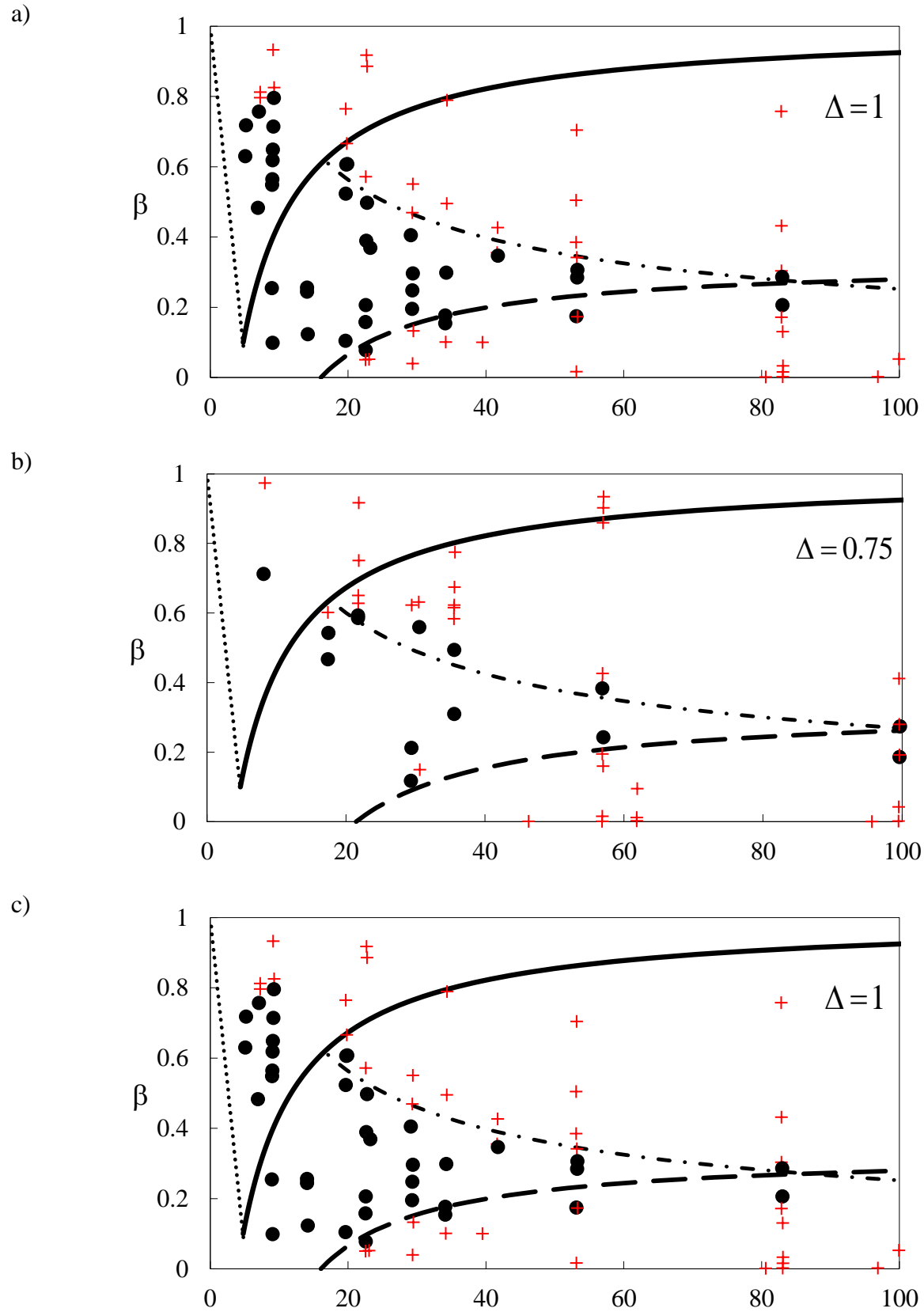


Figure 1.A.6 Droplet-droplet regimes for water drops in air at one atmosphere (Ashgriz-Poo, 1990).

1.6 References

1. Post, S. and Abraham, L. (2002), “Modeling the outcome of drop-drop collisions in Diesel sprays”, *International Journal of Multiphase Flow*, Vol. 28, Iss. 6. pp. 997-1019.
2. Kollar, L., Farzaneh, M., Karev, A. (2005), “Modeling droplet collision and coalescence in an icing wind tunnel and the influence of these processes on droplet size distribution, *International Journal of Multiphase Flow*, Vol. 31, Iss. 1. pp. 69-92.
3. Adams, J.R., Lindblad, N.R. & Hendricks, C.D. (1968), “The Collision, Coalescence, and Disruption of Water Droplets” *Journal of the Applied Physics* Vol. 39, pp. 5173-5180.
4. Qian, J. and Law, C.K., (1997) "Regimes of Coalescence and Separation in Droplet Collision," *Journal of Fluid Mechanics*, Vol. 331, pp. 59-80.
5. Brazier-Smith, P. R., Jennings, S. G. and Latham, J., (1972) “The Interaction of Falling Water Drops: Coalescence,” *Proceedings of the Royal Society of London. Series A, Mathematical and Physical Sciences* Vol. 326, No. 1566, pp. 393-408.
6. Qian, J., Tryggvason, G. and Law, C. K. (1997) “[An experimental and computational study of bouncing and deformation in droplet collision](#)” AIAA-1997-129, *Aerospace Sciences Meeting and Exhibit*, 35th, Reno, NV, Jan. 6-9.
7. Bach, G. A., Koch D. L. and Gopinath, A. (2004) “Coalescence and bouncing of small aerosol droplets”, *Journal of Fluid Mechanics*, 518, pp. 157-185.
8. Loth, E. (2010) “Point-force Collision Models for Solid and Fluid Spherical Particles”, *7th International Conference on Multiphase Flow*, Tampa, FL.
9. Estrade, J.-P., Carentz, Hervé, Lavergne, G., and Biscos, Y., (1999) “Experimental investigation of dynamic binary collision of ethanol droplets – a model for droplet

- coalescence and bouncing,” *International Journal of Heat and Fluid Flow*, Vol. 20, pp. 486-491.
10. Ashgriz, N. and Poo, J. Y. (1989) “Coalescence and separation in binary collisions of liquid drops,” *Journal of Fluid Mechanics*, Vol. 221, pp. 183-204.
 11. Jiang, Y. J., Umemura, A., and Law, C. K., (1992) “An experimental investigation on the collision behaviour of hydrocarbon droplets,” *Journal of Fluid Mechanics*, Vol. 234, pp. 171-190.
 12. Park, R. W. (1970) “Behavior of water drops colliding in humid nitrogen”, Ph.D. thesis, Department of Chemical Engineering, The University of Wisconsin, p.577.
 13. Arkhipov, V.A, Vasenin, I.M & Trofimov, V.F. (1983) “Stability of colliding drops of ideal liquid”, Tomsk. Translated from *Zh.Prikl. Mekh. Tekh. Fiz.* 3, 95-98.
 14. Brenn, G., & Kolobaric (2006) “Satellite droplet formation by unstable binary drop collisions” *Physics of Fluids*, Vol. 18, Art. 087101.
 15. Ochs III, H. T., Beard, K. V., Laird N. F., Holdridge, D. J, and Schaufelbergert, D. E., (1995)“Effects of Relative Humidity on the Coalescence of Small Precipitation Drops in Free Fall”, *Journal of the Atmospheric Sciences*, Vol. 52, No.21.
 16. Gotaas, C., Havelka, P., Jakobsen, H-A., Svendsen, H.F., Hase, M., Roth, N. and Weigand, B., (2007) “Effect of viscosity on droplet-droplet collision outcome: Experimental study and numerical comparison”, *Physics of Fluids*, Vol. 19, 102106.
 17. Payr, M., Vanaparthi, S.H. and Meiburg E. (2005) “Influence of variable viscosity on density-driven instabilities in capillary tubes”, *Journal of Fluid Mechanics*, Vol. 525, pp. 333-353.

18. Bayer, S.I and Megaridis C.M. (2006) “Contact angle dynamics in droplets impacting on flat surfaces with different wetting characteristics”, *Journal of Fluid Mechanics*, Vol. 558, pp. 415-449.
19. Kuschel, M. and Sommerfeld, M. (2011) “Collision regimes of the series of alcohol”, *24th Annual Conference on Liquid Atomization and Spray Systems*, Estoril, Portugal.
20. Czys, R. R. and Ochs, H. T. (1988) “The influence of charge on the coalescence of water drops in free fall”, *Journal of the Atmospheric Sciences*, November, pp 3161-3168.
21. Brenn, G., Valkovska, D. and Danov, K.D. (2001) “The formation of satellite droplets by unstable binary drop”, *Physics of Fluids* Vol. 13, pp. 2463-2477.
22. Willis, K. D. and Orme, M. E., (2000) "Experiments on the dynamics of droplet collisions in a vacuum", *Experiments in Fluids*, Vol. 29, pp. 347-358.
23. Neitzel, G.P & Dell'Aversana, P. (2002) “Noncoalescence and Nonwetting Behavior of Liquids”, *Annual Rev. Fluid Mech.* Vol. 3, pp. 267–89.
24. Tsouris, C. ,and Tavlarides, L.L (1994) “Breakage and coalescence models for drops in turbulent dispersions”, *AIChE Journal*, Vol. 40, No. 395-406.
25. Pan, K., Law, C. K. and Zhou B. (2008) “Experimental and mechanistic description of merging and bouncing in head-on binary droplet collision”, *Journal of Applied Physics*, 103, 064901.
26. Jiang, X. (2006) “Numerical simulation of head-on collision of two equal sized drops”, PhD. Thesis, University of Minnesota.
27. Minnaert, M. (1933) “On musical air-bubbles and the sounds of running water,” *Phil Mag.* Vol. 16, pp. 235-248.

2 Predicting Contact Angles for Regular Surfaces

2.1 Introduction

2.1.1 Motivation

Numerous research studies have used models for the antiwetting behavior of a surface based on its geometric (pattern shapes) and chemical (surface energy) properties. Such models help describe the physics of antiwetting and help guide the design of the surfaces.

The typical models for antiwetting behavior characterize surface performance through static and dynamic contact angles. Two most common models that are used to predict the contact angles on patterned surfaces are the Wenzel (W) and Cassie-Baxter (CB) models. As discussed in the next section, these models can also be used to predict transition between Wenzel state and the Cassie-Baxter state on such surfaces. However, the robustness of these highly-cited models is not well understood nor characterized, especially for recently-developed regularly-patterned superhydrophobic surfaces. This lack of a detailed assessment motivates the present study which examines the fidelity of the Wenzel and Cassie-Baxter models with a comprehensive set of data for superhydrophobic surfaces with a wide variety of geometries.

2.1.2 Common Contact Angle Models

The antiwetting behavior is typically characterized through the static contact angle (θ), dynamic contact angles: i) advancing contact angle (θ_{adv}) and receding contact angles (θ_{rec}). Observations¹ have shown that the static, i.e. equilibrium, contact angle generally falls between the advancing contact angle and the receding contact angle.

The static contact angle (θ_{smooth}) of a liquid on a flat smooth solid surface is given by Young's equation²:

$$\cos \theta_{smooth} = \frac{\gamma_{SG} - \gamma_{SL}}{\gamma_{LG}} \quad (2.1)$$

where γ_{SG} , γ_{SL} and γ_{LG} are the interfacial free energies per unit area of the solid-gas, solid-liquid and liquid-gas respectively. This equation only applies to a flat or smooth surface.

When the surface roughness exists, the Wenzel model assumes that the liquid penetrates the asperities of the region where it is in contact with the surface.³ Due to this definition, the surface that is in Wenzel state is often referred to as the “wetted surface”. This model was proposed to predict the static contact angle on a rough surface relative to that on a smooth surface.

$$\cos \theta^w = r \cos \theta_{smooth} \quad (2.2)$$

where r is the ratio of the actual area of the rough surface to the projected area. Other researchers¹ have proposed that this same model can be applied to predict the dynamic contact angles on a rough surface relative to those on a smooth surface

$$\cos \theta_{adv}^w = r \cos \theta_{adv,smooth} \quad (2.3a)$$

$$\cos \theta_{rec}^w = r \cos \theta_{rec,smooth} \quad (2.3b)$$

These models are not as well tested.

The other model commonly used in the literature is the Cassie-Baxter model which assumes a composite surface is formed when a droplet comes in contact with a rough surface which makes the liquid droplet to be lifted up the roughness features.⁴ The static contact angle on a rough surface is predicted by:

$$\cos \theta^{CB} = \phi_s (\cos \theta_{smooth}) - (1 - \phi_s) \quad (2.4)$$

where ϕ_s is the solid-liquid contact fraction of the surface, i.e. the upper area of the surface expected to support the liquid in the Cassie state normalized by the total area of surface. One may similarly, predict the dynamic angles in the Cassie-Baxter-State as

$$\cos \theta_{adv}^{CB} = \phi_s (\cos \theta_{adv,smooth}) - (1 - \phi_s) \quad (2.5a)$$

$$\cos \theta_{rec}^{CB} = \phi_s (\cos \theta_{rec,smooth}) - (1 - \phi_s) \quad (2.5b)$$

From the static contact models above, one may predict exists the transition between Wenzel and Cassie-Baxter state. In particular, the transition roughness, r_{trans} can be determined by combining Eqns. (2.2) and (2.4):

$$r_{trans} = \phi_s - \frac{1 - \phi_s}{\cos \theta_{smooth}} \quad (2.6)$$

If the $r < r_{trans}$, then the liquid penetrates the pillars and therefore is in the Wenzel state. If the $r > r_{trans}$, then the liquid suspends on the pattered surface and is in the Cassie state.

2.1.3 Objective

The objective herein is to investigate the performance of the aforementioned models to experimental data taken across many different surfaces to examine their robustness. The models have been often applied within a single investigation but typically not with respect to other studies and with respect to highly different shapes. In this study, the applicability of the models for several investigations (with a wide variety of length-scales, shapes and surface energies) is explored for the static, advancing and receding contact angles as well as the Wenzel to Cassie state transition criterion. If the transition could be predicted accurately, surfaces could be designed to safely remain in only one of these states or surfaces could be designed as switchable between the states. To the author's knowledge, this is the first study to conduct a comprehensive survey of available data in terms of the Cassie-Baxter and Wenzel models for static and dynamic models, and especially for transition.

2.2 Data Surveyed

The classic wetting models from Eqs. 2.1-2.6 have been often applied for comparison within a set of surfaces from a single published study. In this study, the applicability of the wetting models is explored for data from several studies to investigate the predicted vs. measured hydrophobic performance. In particular, several different types of regularly-patterned surfaces with a wide range of chemical functionality and geometric shape were considered in terms of the static, advancing and receding contact angles as well as in terms of the Wenzel to Cassie state transition criterion. To be as comprehensive as possible, the publically available literature was extensively reviewed for experimental data which met the following guidelines: a) quantitative geometrical dimension is reported, b) the smooth contact angle (θ_{smooth}) is reported, c) the roughness ratio, r and the solid fraction ratio, ϕ_s , is either reported or could be calculated and d) the apparent contact angle is reported. Table 2.1 shows the studies which satisfied these criteria and includes information on pitch (p , distance between pillar centers or geometry centers), height (h , total height of the pillars or geometry), width (w , dimensional length of the pillars or geometry), smooth static contact angle (the contact angle without any surface texturing, θ_{smooth}) and diameter of the droplet that was used to measure the contact angles. The features of these surfaces are shown in Fig. 2.1 where they are grouped by geometric shape including: square posts, cylindrical posts, hoodoo or mushroom surfaces and some non-traditional surfaces.

Table 2.1 Hydrophobic data sets used for survey with ranges shown for sets that contain multiple surfaces

Dataset	Shape	Pitch, p (μm)	Height, h (μm)	Width (μm)	θ_{smooth} (Deg)	Droplet diameter, d (mm)	d*, d/p
Cortese et al.	Square posts	28-70	25	10-28	115	3-10	43-107
Yeh et al.	Square posts	3-9	3-20	0.04- 18.59	120	0.5-1.5	56-500
Zhu et al.	Square posts	20-100	16	10-85	110	N/A	N/A
Milionis et al.	Square posts	60	33	42	82	2.7	45
Oner et al.	Square posts and star shaped posts	4-256	20-140	2-128	105	0.5-1.5	2-375
Furstner et al.	Square posts and cylindrical pillars	1-5	1-4	1-2	103-120	3	1200
Bushan et al.	Cylindrical pillars	10-26	5-30	5-14	~110	2	77-200
Bushan & Jung	Cylindrical pillars	7-210	10-30	5-14	109	2	9-286
Zhao et al.	Cylindrical pillars with flat top	4.5-12	7-7.2	3	107	2	167-444
Martines et al.	Cylindrical pillars with flat and hemispherical top	0.3	0.116- 0.792	0.105- 0.157	114	2-3	6667- 10000
Tuteja et al.	Hoodoo – Mushroom shape	10	N/A	N/A	55	1.5	150
Choi et al.	Hoodoo Surface	22.4	7	17.6	68	4	179
Shirtcliffe et al.	“Chocolate chip cookies”	~30	<5	~20	N/A	N/A	N/A

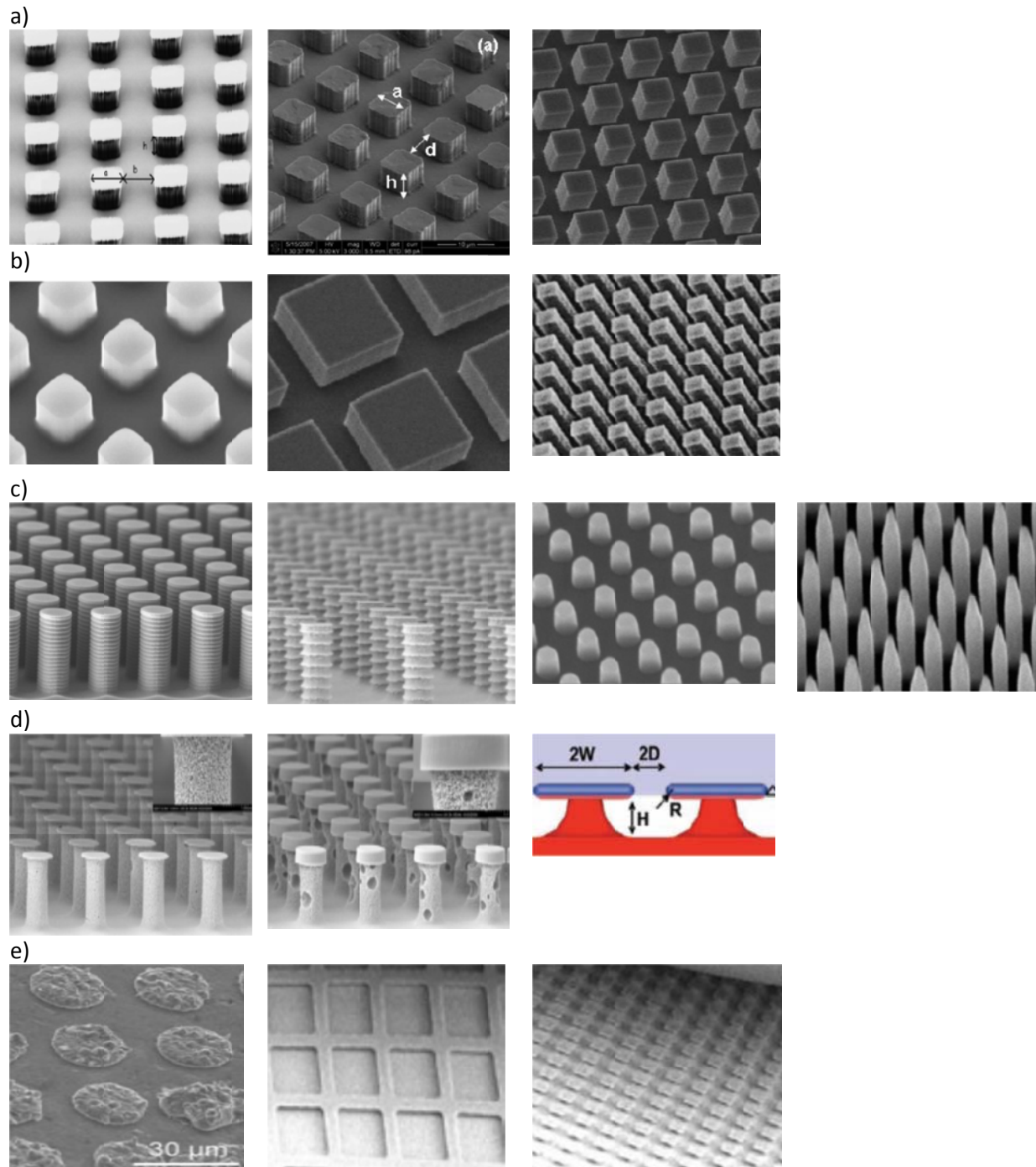


Figure 2.1 Images of surfaces used for present survey listed by row:

- a) square posts from Cortese et al., Yeh et. al, Zhu et al.,
- b) square posts from Milionis et al., Furstner et al. and Oner et al.
- c) cylindrical posts from Furstner et al., Furstner et al., Bushan et al., Zhao et al.,
- d) hoodoo surfaces from Zhao et al., Zhao et al., Martines et al. , and
- e) non-traditional surfaces from Shirtcliffe et al, Choi et al., Choi et al.

2.3 Results and Discussion

The available data in the literature for a regular surface was first examined in terms of receding angle as this angle has been identified as particularly critical for predicting droplet-wall rebound.¹⁷ Results for the available data from three studies are shown in Fig. 2.2 for which the smooth receding angles for all three studies was nearly the same. It can be seen that the Wenzel model accurately predicting the receding contact angle for roughness levels ranging from unity (smooth surface) up to the transition value (r_{trans}). At higher roughness levels, the receding contact angle dramatically increase from hydrophilic ($<90^\circ$) to hydrophobic ($>90^\circ$) as the droplet interface transitions from the “Wenzel” state to “Cassie” state. It is interesting to note that the transition occurs around roughness ratio, r , of around 1.3-1.4 for all three surfaces shown. All the surfaces reported here of the type square posts.

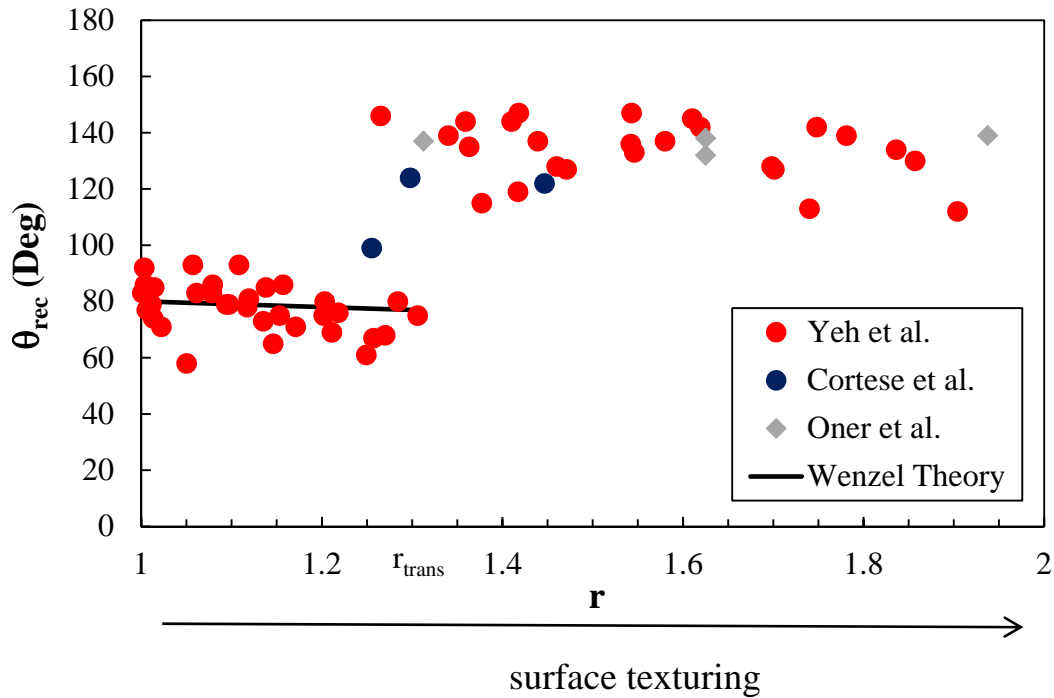


Figure 2.2 Receding contact angle as a function of roughness ratio

Figure 2.2 shows the receding contact angles for water on surfaces plotted as a function of the unity minus the solid fraction. Plotting it in this fashion ensures that texturing increases from left to right, so as to be consistent with that for Fig. 2.3. The results indicate strong quantitative agreement between data and the CB theory for texturing with $1-\phi_s$ as high as 0.85. This is rather remarkable given that this theory was developed for static angles and that the resulting receding angles for this regime are quite different from the smooth values. However, it should be noted that the surfaces tend to show departure from the theory when $1-\phi_s$ exceeds 0.85, i.e. when the protruding solid fraction area is reduced below 15%. This difference may be partially attributed to experimental uncertainty, but may also be related to the shapes of the pillars for these surfaces. In particular, pillars with a square cross-section and a flat top (Yeh et al.) yielded the lowest receding angles while those with a cylindrical cross-section and a flat top (Zhao et al.) were higher but still below the predicted values. Interestingly, the surfaces with a cylindrical cross-section and a hemi-spherical top yields the highest receding angles. This suggests that reducing sharp corners on the pillar top surfaces tends to improve the receding angle hydrophobicity. It should also be noted that the variation in the Oner data for $1-\phi_s=0.75$ is associated with increasing values of pitch to height ratio. The increase in height is not reflected in the solid area fraction, ϕ_s , and therefore yields a constant value although the contact angle could change as the height changes. The C-B model for hexadecane is reasonably accurate in predicting the contact angles. However, the octane model underpredicts the contact angles although the qualitative trend is predicted accurately. Isotropy could also impart an effect on the contact angles.⁵

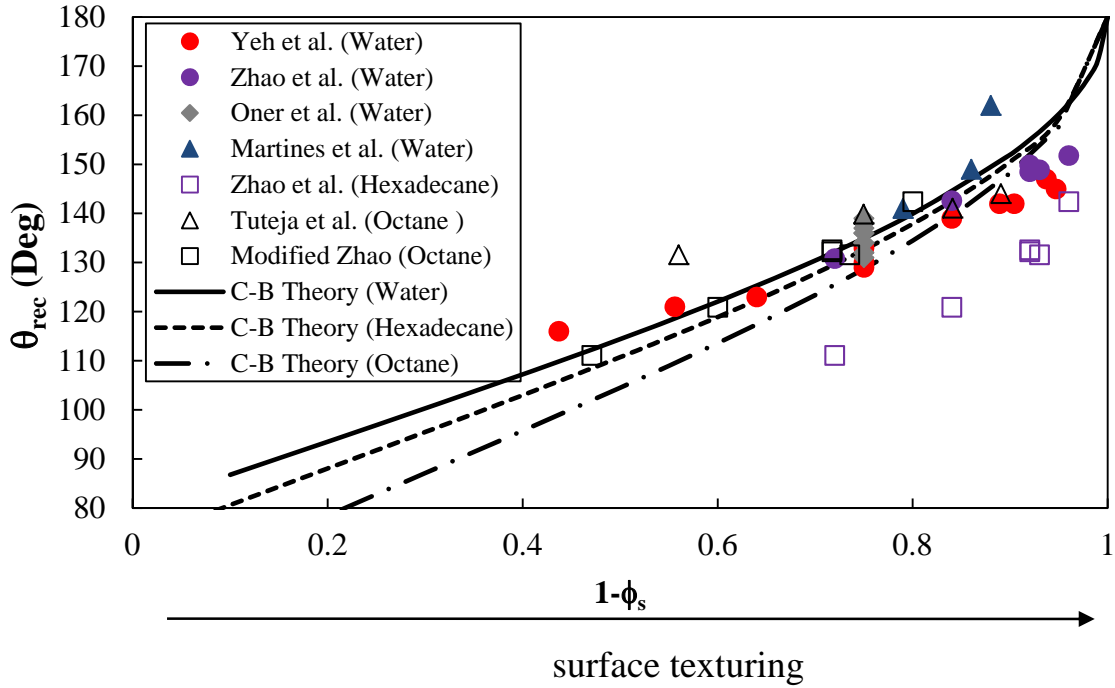


Figure 2.3 Receding contact angle as a function of solid fraction

The advancing contact angles were next considered, and Fig. 2.4 shows the results as a function of roughness ratio, r . Unlike the receding contact angle, the advancing contact angle is only qualitatively predicted by the Wenzel theory before the onset of transition, and does not show a marked increase just past this transition. Instead, the advancing angle shows a more gradual rise though there is considerable scatter despite that all three surface have the same shape (square flat-top posts) and nearly the same smooth advancing angle.

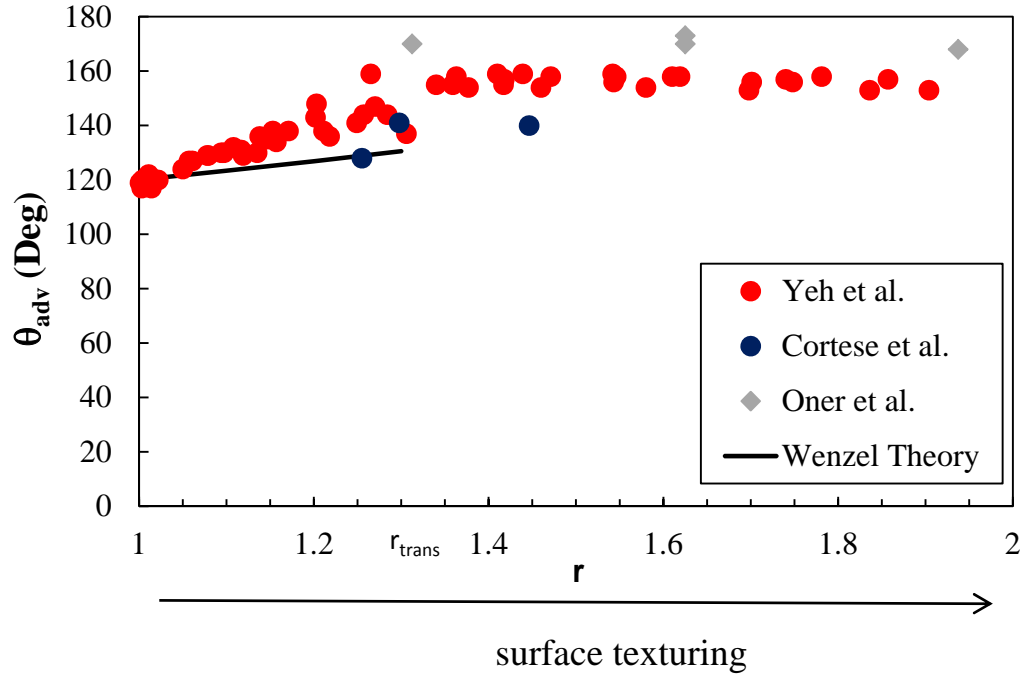


Figure 2.4 Advancing contact angle as a function of roughness ratio

Turning attention to the advancing angles as a function of surface solid fraction for the Cassie-Baxter state, the results are shown in Fig. 2.5 for data significantly above the Wenzel predicted values. It can be seen that the departures from theory are even more exaggerated with the differences that are both quantitative and qualitative for both the superhydrophobic and superoleophobic surfaces. In particular, the Cassie-Baxter theory predicts a gradually increasing trend commensurate with increasing surface texturing, while the measured advancing contact angles (aside from the Oner data) tends to be nearly a constant value between 155° and 165° , i.e. independent of the solid fraction as shown by the boxed region. This may be partially attributed to the higher proximity of Wenzel and Cassie-Baxter predictions for advancing angles as compared to that for receding angle, as this reduces the outcome sensitivity of transition. However, it appears that an advancing “Cassie” state does not depend strongly on the surface area for the data in this boxed region. This lack of agreement is consistent with experiments and

predictions of Tuteja et al.¹³ One exception is the Oner data which includes higher advancing angles as the height is increased. The solid area fraction is not a function of the height, so the solid area fraction remains constant. Oner noted that as the height is increased the advancing contact angle increased but after a certain height it started decreasing. This could be related to the the droplet penetrating the asperities at the non-critical heights.

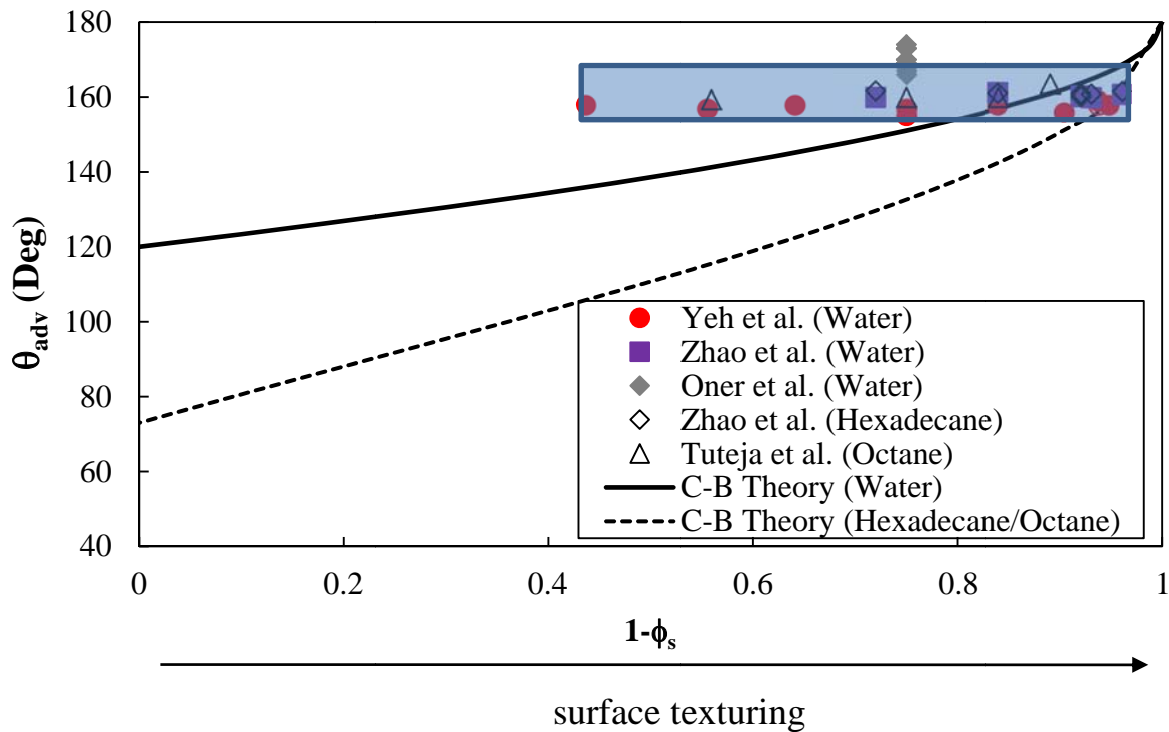


Figure 2.5 Advancing contact angle as a function of solid fraction

The effects of roughness and surface areas are next considered for the static constant angle. Figure 2.6 shows the static contact angle as a function of roughness ratio, r , for which three of the studies use surfaces whose smooth contact angle is about 100° but where a fourth surface (from Milionis) is hydrophilic in the smooth state. Considering the other three surfaces first, it can be seen that the Wenzel theory is at least qualitatively correct up to the transtion point,

whereafter the contact angle increases significantly. It is interesting that this increase is more gradual for the Furstner *et al.*¹⁵ surfaces and this may be due to a difference in nominal and actual dimensions.

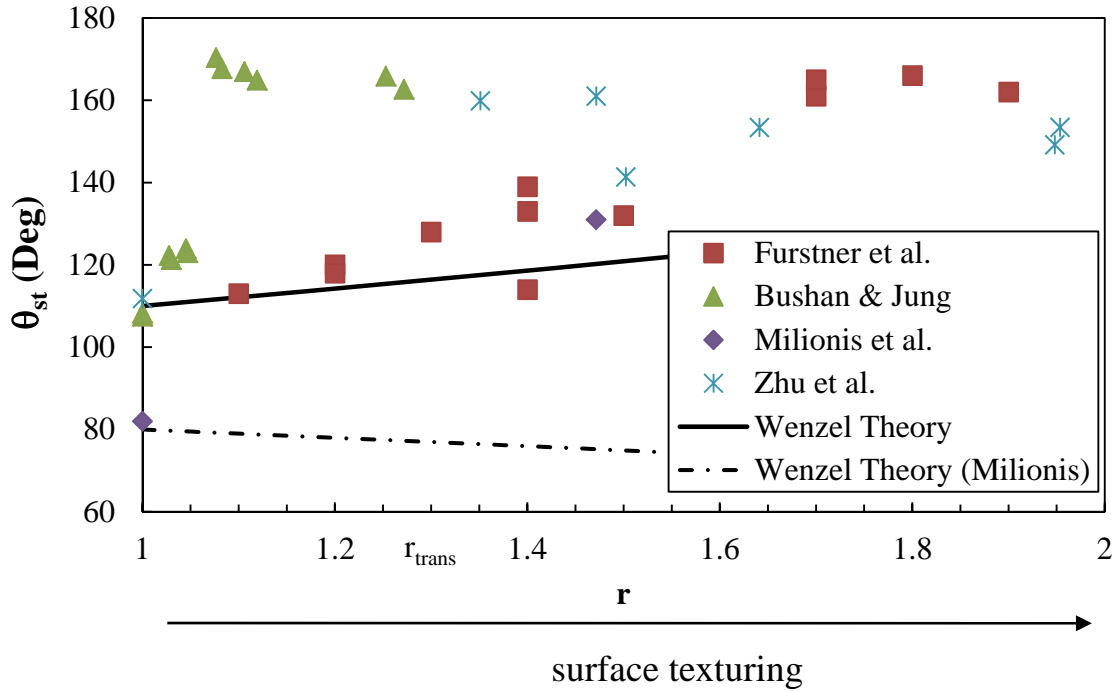


Figure 2.6 Static contact angle as a function of roughness ratio

It has been suggested that the advancing contact angle behaves similar to the static contact angle.⁶ Comparing Fig. 2.6 and 2.3 indicates that the behavior is qualitatively similar for the Wenzel regime. However, the roughness transition for static contact angle occurs in a relatively wide range of 1.1 to 1.5. The average value is similar to that observed for advancing angles in Fig. 2.2, but there is greater scatter. This may be partially due to the difficulty of defining a single equilibrium angle as the static state can be metastable, and thus not as deterministic as the static state.¹⁷ For example, some studies suggest that vibrations or slight inhomogeneities the droplet can transition from “Cassie” to “Wenzel” mode, where the latter is a more stable state in terms of surface energy.^{11,14} The above results indicate that transition from Wenzel to Cassie-Baxter is

more accurately and effectively predicted by receding contact angle rather than by static or advancing contact angle.

In Fig. 2.7, the static contact angles were plotted against the solid fraction to determine the predictive fidelity for the Cassie-Baxter theory. A qualitative agreement is observed with the CB model in that higher texturing (increased values of $1-\phi_s$) tended to correlate with higher static contact angles. However, for low to moderate texturing ($0.2 < 1-\phi_s < 0.85$), the measured values were generally higher than the theoretical predicted values. For high texturing ($0.8 < 1-\phi_s < 0.9$), the measured values were generally scattered above and below the predictions. This lack of agreement is consistent with experiments and predictions of Varanasi et al.¹⁷ Moreover, most of the data fell in the boxed region shown in Fig. 2.7, regardless of the solid fraction value. This indicates that achieving a high static contact angle does not require the surface to have the surface texture consistent with theoretical predictions. Instead, achieving a static contact angle of more than 145° once transition has occurred requires only that the smooth surface is hydrophobic ($\theta_{smooth} > 90^\circ$), and the upper (contact) surface is a minority of the overall projected surface area ($\phi_s < 0.5$). The results also show that other characteristics are more important at predicting static contact angle, e.g. pitch/height ratio and hoodoo geometry and the droplet re-entrant curvature.

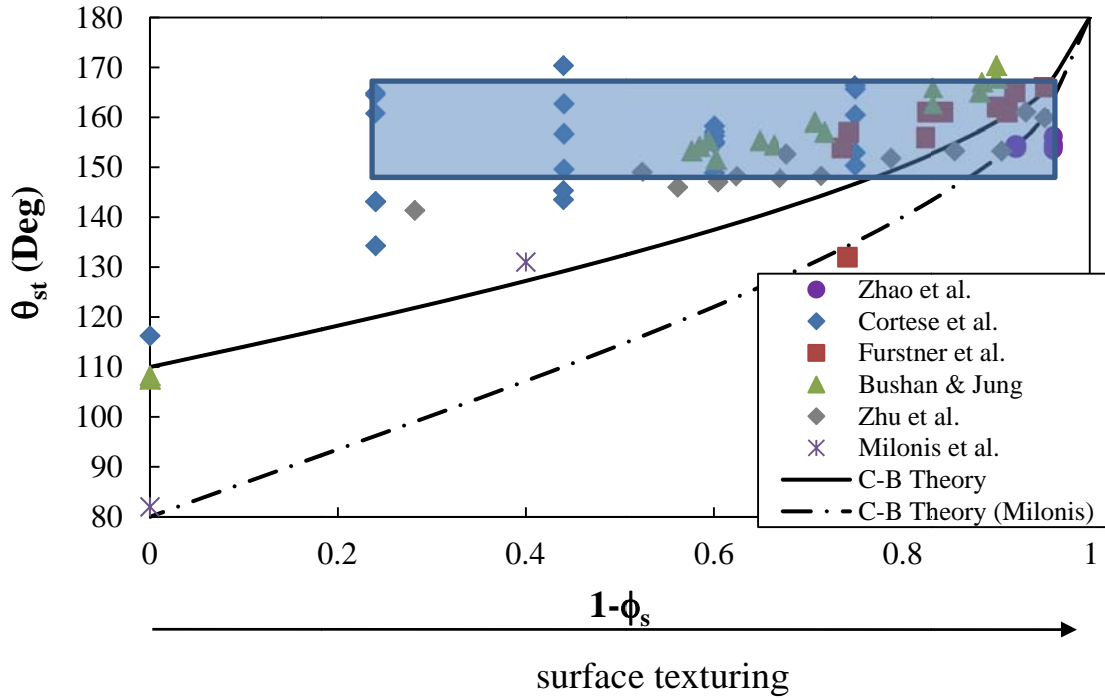


Figure 2.7 Static contact angle as a function of solid fraction

Figure 2.8 shows the theoretical transition roughness, r_{trans} , predicted by Eqn. (2.6), which is derived from both the Wenzel and Cassie-Baxter model. This model predicts a decreasing trend of transition roughness as a function of solid fraction, i.e. more roughness is required as the projected contact surface area increases (e.g. higher pillars are needed as they become more further spaced apart). In contrast, the experimental data (based on Figs. 2.2 and 2.6) indicate that the transition roughness is independent of the solid fraction for a given surface. In particular, r_{trans} generally falls between the range of 1.2 to 1.4, especially if the more reliable receding angle results for transition are considered. This criterion may be important in terms surface preparation in specifying and dimensionlizing the surface geometry to get a high antiwetting behavior through high contact angles. This result may also explain why irregular surfaces do not require high aspect ratios (height to width) of the protruding surface features in order to achieve high contact angles.¹⁸

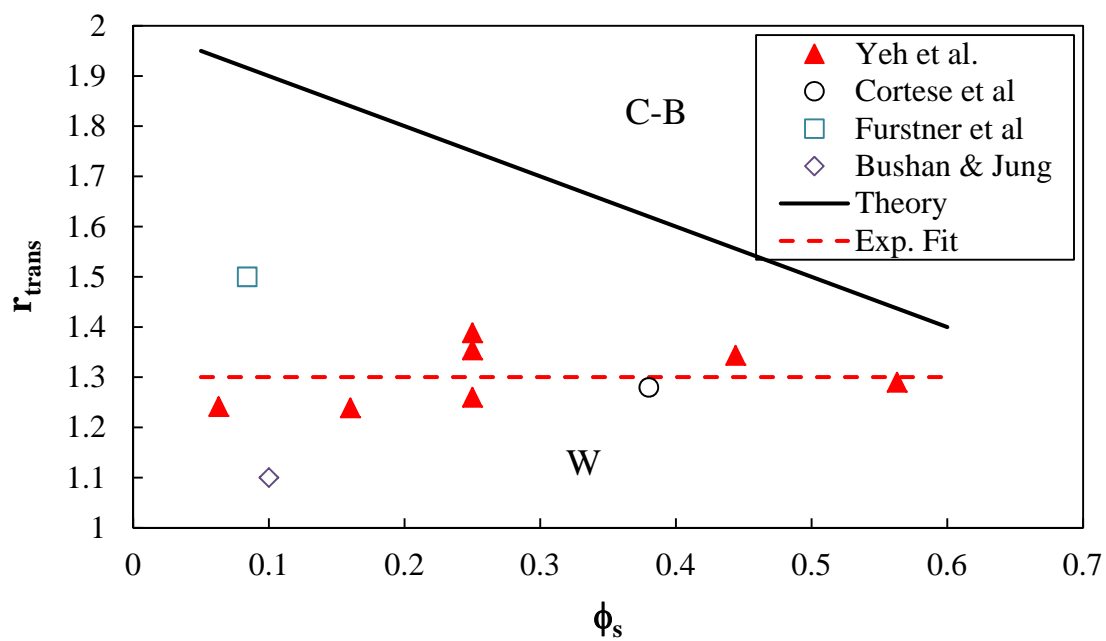


Figure 2.8 Transition roughness as a function of solid fraction

2.4 Conclusions

A comprehensive survey of experimental data was conducted to investigate the predictive fidelity of the highly-cited Wenzel and Cassie-Baxter theories for static, advancing and receding contact angles, as well as for the transition roughness. The Wenzel and CB models are generally universally applicable for most cases with the exception of some cases. The Wenzel and CB model has very strong qualitative agreement with regards to the receding contact angle. The CB model does not accurately predict the advancing contact angle while the Wenzel model performs well for advancing contact angle. Both models are inconsistent in terms of predicting the onset of transition from Wenzel to Cassie state. Both models also do not predict the static contact angle accurately.

The experimental results show that a static contact angle of more than 145° can be generally achieved if the smooth surface is hydrophobic in recession ($\theta_{smooth,rec} > 90^\circ$), the roughness is sufficient for transition ($r > 1.3$), and the upper (contact) surface is a minority of the overall projected surface area ($\phi_s < 0.5$). This is a significantly lower requirement than that predicted by the conventional wetting theory models. The receding angle is identified as the most accurate and consistent contact angle measurement for predicting transition.

2.5 References

1. Extrand, C.W., Model for Contact Angles and Hysteresis on Rough and Ultraphobic Surfaces, *Langmuir*, **2002**, 18, 7991-7999.
2. Young, T.; An Essay on the Cohesion of Fluids, *Phil. Trans. R. Soc. Lond.*, **1805**, 95: 65–87
3. Wenzel, R.N.; Resistance of solid surfaces to wetting by water, *Ind Eng Chem*, **1936**, 28:988-994.
4. Cassie, A. B. D.; Baxter, S.; Wetting of porous surfaces, *Trans. Faraday Soc.*, **1944**, 40, 546-551.
5. Good, R.; Kvikstad, J.; and Bailey, W.; Anisotropic Forces in the Surface of a Stretch-Oriented Polymer, *Journal of Colloid and Interface Science*, **1971**, Vol. 35, No.2.
6. Yeh, K.; Chen, L.; Contact Angle Hysteresis on Regular Pillar-like Hydrophobic Surfaces, *Langmuir*, **2008**, 24, 245-251.
7. Martines, E.; Seunarine, K.; Morgan, H.; Gadegaard, N.; Wilkinson, C.D.W; Riehle, M.; Superhydrophobicity and Superhydrophilicity of Regular Nanopatterns, *Nano Letters*, **2005**, Vol. 5, No.10, 2097-2103.
8. Zhao, H.; Park, K.; and Law, K.; Effect of Surface Texturing on Superoleophobicity, Contact Angle Hysteresis, and “Robustness”, *Langmuir*, **2012**, 28, 14925-14934.
9. Cortese, B.; D’Amone, S.; Manca, M.; Viola, I.; Cingolani, R.; and Gigli, G.; Superhydrophobicity Due to the Hierarchical Scale Roughness of PDMS Surfaces, *Langmuir*, **2008**, 24, 2712-2718.
10. Oner, D; and McCarthy T.; Ultrahydrophobic Surfaces, Effects of Topography Length Scales on Wettability, *Langmuir*, **2000**, 16, 7777-7782.

11. Bormashenko, E.; Pogreb, R.; Whyman, G.; and Erlich, M.; Cassie-Wenzel Wetting Transition in Vibrating Drops Deposited on Rough Surfaces: Is the Dynamic Cassie-Wenzel Wetting transition a 2D or 1D affair?, *Langmuir*, **2007**, 6501-6503.
12. Millionis, A.; Martiradonna, L.; Anyfantis, G.; Cozzoli, P. Bayer, I.; Fragouli, D.; and Athanassiou, A.; Control Of Water Adhesion On Hydrophobic Micropillars By Spray Coating Technique, *Colloid Polymer Science*, **2012**, DOI 10.1007/s00396-012-2752-5.
13. Tuteja, A.; Choi, W.; Ma, M.; Mabry, J.; Mazzella, S.; Rutledge, G.; McKinley, G.; Cohen, R.; Designing Superoleophobic Surfaces, **2007**, *Science*, Vol. 318.
14. Shirtcliffe, N.; Mchale, G.; Newton, M.; Chabrol, G.; Perry, C.; Dual-scale Roughness Produces Unusually Water Repellent Surfaces, *Advanced Materials*, **2004**, 16, No.21.
15. Furstner, R.; Barthlott, W.; Wetting and Self-cleaning Properties of Artificial Superhydrophobic Surfaces, *Langmuir*, **2005**, 21, 956-961.
16. Bhushan, B.; Nosonovsky, M.; Jung, Y.; Towards optimization of patterned superhydrophobic surfaces, *Journal of Royal Society Interface*, **2007**, 4, 643-648.
17. Varanasi, K., Deng, T., Hsu, M., Bhate, N.; Hierarchical Superhydrophobic Surfaces Resist Water Droplet Impact, *MIT Open Access Article*, **2009**, 2009-05.
18. Steele, A., Bayer, I., Loth, E.; Inherently Superoleophobic Nanocomposite Coatings by Spray Atomization, *Nano Lett.*, **2009**, 9(1), pp 501-505.

3 Drop Impact on Nanotextured Surfaces

3.1 Introduction

3.1.1 Motivation

Droplet impact on solid surfaces is a phenomenon that occurs in various engineering applications such as spray cooling of heating elements (energy storage devices, turbine blades, semiconductor chips), ink-jet printing, fire suppression sprinklers, internal combustion engine (direct injection diesel engines) and ice formation on aircraft wings, engine compressor blades and wind turbines.

The droplet-wall outcome is often essential in such processes, especially where heat transfer is important since it is linearly proportional to the net amount of surface area of all drops. For example, droplets breaking-up and rebounding upon impact will significantly increase the net droplet surface area providing increased heat transfer. Conversely, the overall surface area will decrease if many droplets deposit on the wall and eventually form a thin liquid film.

Previous literature investigating droplet-wall outcomes has focused on water droplets impacting mainly metal surfaces in smooth dry conditions. However, such studies often do not provide a complete characterization of the surface liquid contact dynamics (as discussed below), leading to classification and criteria of the outcomes that vary significantly within the literature so that a consensus of whether a drop should splash or deposit has not been reached. This is particularly true if the surface have different degrees of liquid repellency as can occur with textured surfaces. With the advent of manufacturing and nanotechnology, nanotextured surfaces have seen an increased usage in engineering applications. Droplets interact differently with nanotextured surfaces because typically they have high contact angles ($>120^\circ$) and intrinsic

roughness. This study focuses on the droplet normal impact outcomes on both smooth and nano-textured surfaces for a wide range of fluid viscosities.

3.1.2 Previous Studies

The droplet impact on a dry wall has been studied extensively.^{1,2} The effects of droplet velocity, diameter, and properties of liquid (namely, surface tension and viscosity) have been extensively researched and are very well understood.^{1,2} Those effects are often expressed through dimensionless numbers of Reynolds number, Re , Weber number, We , and Ohnesorge number, Oh .

$$Re = \frac{\rho v d}{\mu} \quad (3.1a)$$

$$We = \frac{\rho v^2 d}{\sigma} \quad (3.1b)$$

$$Oh = \frac{\mu}{\sqrt{\rho \sigma d}} = \frac{\sqrt{We}}{Re} \quad (3.1c)$$

where the ρ , μ , σ denote the droplet density, viscosity, and surface tension, respectively while the d , and v , is the droplet diameter and velocity normal to the surface just before the impact, respectively. The Reynolds number indicates the ratio of inertial forces to the viscous forces. The Weber number shows the ratio of the inertial forces to the surface tension. This could be used to characterize the droplet deformation as high Weber number will indicate a high degree of deformation. The Ohnesorge number signifies the relation of viscous forces to the inertial and surface tension forces. As shown by Eq. 3.1c, the Reynolds, Weber and Ohnesorge are interdependent and therefore studies generally choose a combination of two from the three dimensionless numbers to study the effects of surface tension, viscosity and collision inertia.

Gravity related effects can be characterized by the Bond number, Bo or the Froude number, Fr .

$$Bo = \frac{\rho g d^2}{\sigma} \quad (3.2a)$$

$$Fr = \frac{v^2}{gd} = \frac{We}{Bo} \quad (3.2b)$$

In this expression, g represents the gravitational acceleration. The gravitational effects will be negligible for a drop-wall impact if $Bo \ll 1$ and $Fr \gg 1$, as is the case for the conditions studied herein. There could also be compressibility effects as seen by Lesser & Field³ and Rein.⁴ Similarly, a Mach number can be used to describe compressibility based on the ratio of droplet impact speed to an acoustic speed of the water or air. The compressibility effect can become important at high droplet velocities of around 100 m/s for a droplet size of 200 μm .^{3,4} Since the droplet velocities studied herein are all than 25 m/s, the compressibility effect is also negligible.

Some studies have identified that contact angle and roughness have an effect on the outcome of a droplet-wall collision.^{1,2} In particular, Rioboo *et al.*¹ suggested that the roughness amplitude, R_a , roughness wavelength, R_w , and the receding contact angle, θ_{rec} , as the controlling parameters in addition to the Reynolds, Weber and Ohnesorge number effects. The latter three non-dimensional numbers are important as they characterize effects of droplet inertia, surface tension and droplet viscosity. The authors also established the qualitative trends of these effects on the specific outcome of droplet-wall outcome and established that roughness can induce a specific outcome, namely the prompt splash. However, the study lacked any transition boundary prediction or outcome regime map (such as the one shown in Fig. 3.1). The study also did not address the coupling effects of identified criteria, i.e. effects on a rough superhydrophobic surface.

Roughness is also important to create high contact angles for hydrophobicity as discussed by Wenzel^{5,6} and Cassie-Baxter⁷. This coupling of contact angle and roughness on the drop impact outcome has made it difficult to determine which of the two has the dominant effect with respect to drop collision outcome, and no previous studies have been able to quantitatively discriminate these effects. In addition, the roughness wavelength is difficult to characterize for an irregular surface, which further limits on our understanding of droplet collision outcomes.

Mundo *et al.*⁸ proposed a model based on a critical splash parameter to identify the deposition/splash limit on a dry wall. Based on his experiments, they established that splashing would occur whenever the critical parameter, K , is greater than 57.7

$$\begin{aligned} K &= Oh Re^{1.25} = We^{0.5} Re^{0.25} \\ We_{crit} &= 57.7 Oh Re^{0.75} \end{aligned} \quad (3.3)$$

Similarly, Cossali *et al.*⁹ investigated the drop-wall impact on a dry wall and with a thin liquid film and proposed a model that incorporates the effects of a thin liquid film.

$$\begin{aligned} K &= \frac{We Oh^{-0.4}}{2100 + 5880 \delta^{1.44}} \\ We_{crit} &= Oh^{0.4} (2100 + 5880 \delta^{1.44}) \end{aligned} \quad (3.4)$$

with δ being the non-dimensional thin liquid film thickness as a ratio of droplet diameter. The authors proposed that splashing would occur whenever the critical parameter, K , is greater than 1. While both models fundamentally employ Weber and Reynolds number, the different quantitative formulation is due to empirical fitting.

Palacios *et al.*¹⁰ conducted experiments to investigate the viscosity effects of drop impact on a solid dry wall and proposed a model based on critical Weber number, beyond which splashing would occur. The authors found that higher viscosity inhibits splashing and proposed a third model to fit his data, which is given by

$$We_{crit} = 0.566 Re^{0.760} + 4484 Re^{-0.5} \quad (5)$$

Vander Wal *et al.*¹¹ proposed a fourth correlation based on critical Ohnesorge number and stated that the critical capillary number is constant and equal to 0.1225 based on the assumption that the kinematic discontinuity resulting from the initial retard on the edge of the outward flowing fluid due to viscosity causes the splashing phenomenon.

$$\begin{aligned} Oh_{crit} Re^{0.609} &= 0.85 \\ We_{crit} &= 0.8 Oh Re^{1.391} \end{aligned} \quad (3.6)$$

The performance of the aforementioned models is shown in Fig. 3.1 in addition to all the experimental data available in the literature. In general, the models proposed by relevant authors agree well with their own experimental data but do not agree with data from other authors. For example, Cossali *et al.*⁹ observes deposition in the splash region predicted by Mundo's model.⁸ This indicates that additional physics must be included to properly determine the critical Weber number for splash transition. In particular, the impact of liquid-surface contact angle is important to include as this was discussed by Rioboo *et al.*¹ to be important. In general, one may expect that surfaces with higher contact angles will have a lower critical Weber number because the surface tension will be high making the droplet have a contact angle in the first place. This hypothesis is consistent with the experiments of Schmidt and Knauss as shown in Fig. 3.1 for which the droplets were molten droplets of mercury and wax. Similarly, recent studies¹³ have

shown that droplets can bounce easily from hydrophobic surfaces (for which static contact angles are greater than 90 deg.) whereas they would generally deposit on regular surfaces that are hydrophilic (for which static contact angles are less than 90 deg.). The Vander Wal *et al.*¹¹ study involved using 2mm sized droplets impacting a smooth aluminum disk with varying liquids. While the results are consistent with Palacios *et al.*¹⁰ results, there is significant disagreement with the results observed by CHR Mundo *et al.*⁸ and Cossali *et al.*⁹ The Vander Wal *et al.*¹¹ disagreement might explain the effect of contact angle as the contact is both a function of the surface and the liquid. As the liquid was varied, there is a change in contact angle. The contact angle might also play a role in the Palacios *et al.*¹⁰ results as he investigated 3mm droplets on a glass surface, which is typically a hydrophobic surface. Also, Palacios *et al.*¹⁰ used various hydrocarbon liquids such as ethanol and propanol which have a significantly higher evaporation rate than water, which also applies to the study by Vander Wal *et al.*¹¹. Since the aerodynamic drag and hence droplet deformation is usually significant for droplet diameter higher than 2mm, that could have played a role in different outcome that Palacios *et al.*¹⁰ observed. In the same study, tap water was used as a baseline condition and any contamination in water or the surface might change the outcome.

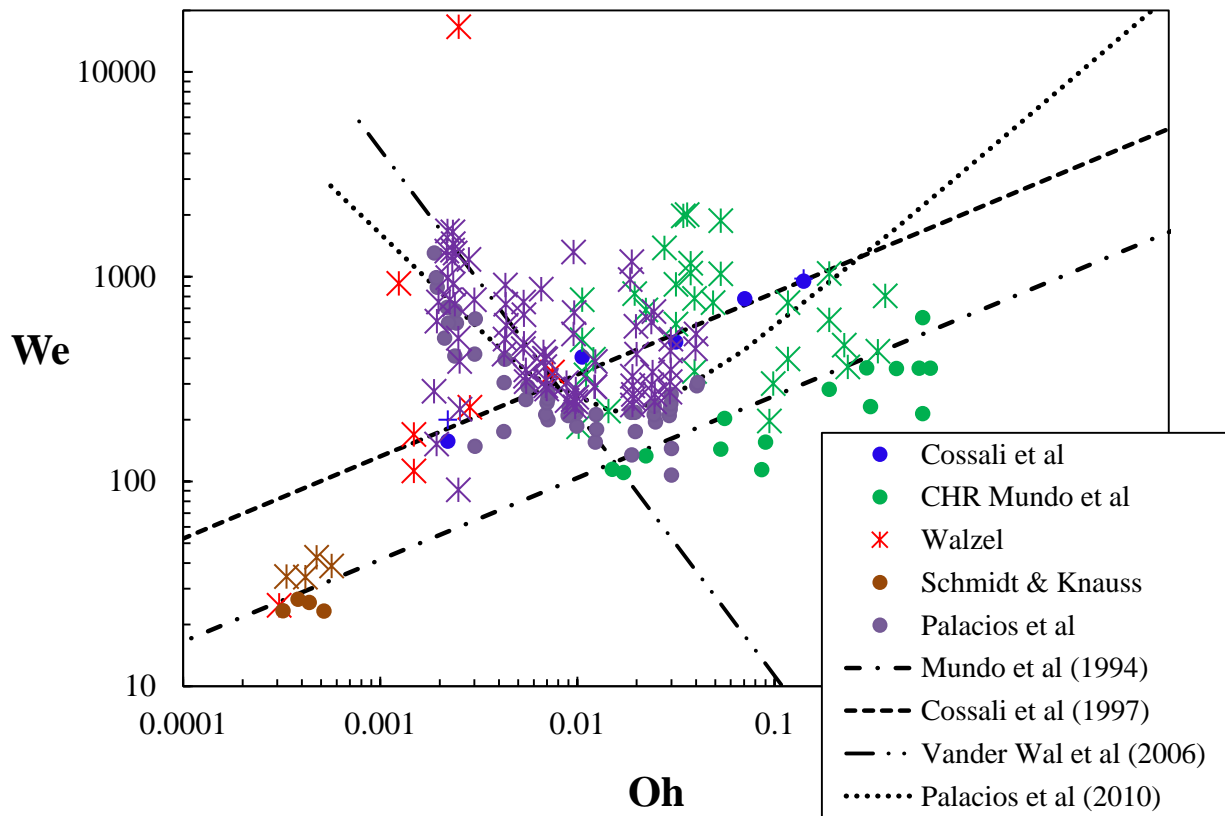


Figure 3.1 Performance of previous deposition boundary models compared to data for a variety of surfaces and liquids where solid symbols indicate deposition and starred symbol indicate splashing

3.1.2 Objectives

To date, none of the previous models of droplet-wall outcome quantitatively account for the effects of contact angle on regime maps such as shown in Fig. 3.1. The objective of this study is to obtain data and investigate the outcome relationships to better understand the role of contact angles, fluid viscosity, and droplet inertia. This may help to develop models that better capture the physics of such droplet-wall collision outcomes. Also, to date all the possible droplet-wall outcomes and definitions have not been compiled yet. Although Rioboo *et al.*¹ did an excellent

job in providing the definitions and photographs of the outcomes, there were some outcomes that were reported after his compilation.

3.2 Experimental Setup

An experimental setup consisting of a droplet syringe with variable hypodermic needle gauge that is capable of producing droplet sizes of 1.5mm to 2mm was used. The droplet diameter corresponds to the hypodermic needle gauge (diameter). A range of liquids, from water to glycerin and different water glycerin mixtures, varying in viscosity and surface tension were used. The impact velocity was varied by varying the height that the droplet was dispensed. Heights ranging from 5mm to 1.2m were achieved. The velocity was then calculated by solving the equation of motion of particle in air while taking into account of the drag force using the Putnam fit.¹² The calculated droplet velocity was then compared against the experimental velocity obtained through image analysis for 3 cases. The difference compared well and was within 10% of the calculated velocity as shown in Fig. 3.2. As the droplet velocity increases, it may start to deform even before it hits the wall due to aerodynamic pressure variations. This deformation can be characterized by the aerodynamic Weber number (We_{aero}) which is defined as in Eq. 3.1b but with the air density used instead of the droplet density. . This deformation is negligible if the Weber number calculated based on the air (fluid) is $We_{aero} < 1$. The region of $We_{aero} > 1$ is shaded in Fig. 3.2. Generally, the experimental results presented herein are below this velocity

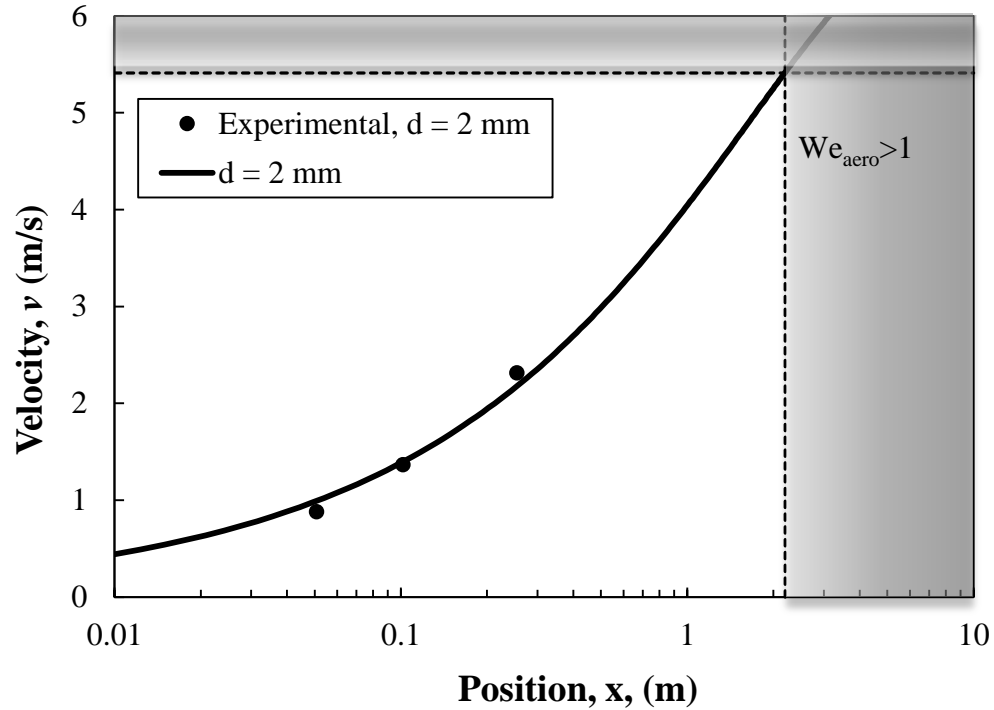


Figure 3.2 Droplet velocity against height

Different surfaces ranging from aluminum, acrylic, both of which are typically hydrophilic, Teflon (PTFE) which is hydrophobic, and an in-house superhydrophobic surface, SH-1 and a commercially available superhydrophobic surface, Rustoleum® NeverWet™ were used in this experiment. The super-hydrophobic samples used in this study have a coating thickness of about of 100 μ m and an arithmetic roughness, R_a , of about 1 μ m. This roughness is considered smooth relative to the size of the 2 mm diameter droplets, i.e. the effect of the roughness can be considered to act as a continuum that changes the wetting angles, rather than individual features that change the angle depending on the droplet position.

The droplet wall interaction is captured with the use of high-speed camera, Photron SA4, connected to a computer with sufficient backlighting. A schematic and a picture of the experimental setup are shown in Fig. 3.3. Besides that, the contact angle measurements of

samples were measured with the use of a goniometer and digital camera. The contact angles were obtained through image analysis software ImageJ in tandem to the DropSnake add-on.

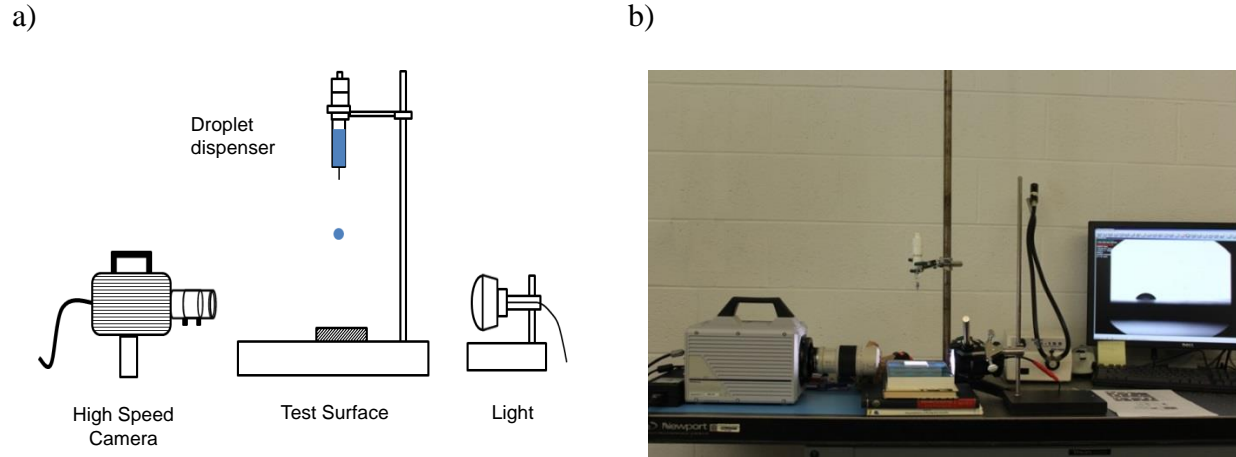


Figure 3.3 a) Illustration and b) Picture of the experimental setup

3.3 Results

3.3.1 Droplet-wall Outcome

Six types of outcomes were observed in the present in a droplet-wall collision experiments as shown in Fig. 3.4, which include:

- i. **Deposition:** The drop deforms during impact and stays attached to the surface during its entire impact process, without any breakup.
- ii. **Splash/Deposition:** A prompt splash is observed when fine droplets leave the surface upon impact followed by a deposition, i.e. deformation and stays attached to the surface. Small satellite droplets may break from the main droplet but they do not leave the wall.

- iii. **Prompt splash/Break-up:** Generation of droplets at the contact line at the beginning of spreading phase followed by a break-up that leaves behind some drops due to the receding lamella as the liquid retracts from the maximum spreading radius.
- iv. **Corona splash/Break-up:** Occurs when droplets are formed around the rim of corona, away from the solid surface (typically seen on liquid films) followed by a break-up of droplets.
- v. **Partial rebound:** Some liquid is left on the solid surface while a bounce is seen through the jetting of the liquid.
- vi. **Full rebound:** The droplet interacts with the surface and bounces off the solid wall without leaving behind any liquid upon the first impact.

The videos of the different outcomes were attached in the appendix section (§3.5) of this chapter.

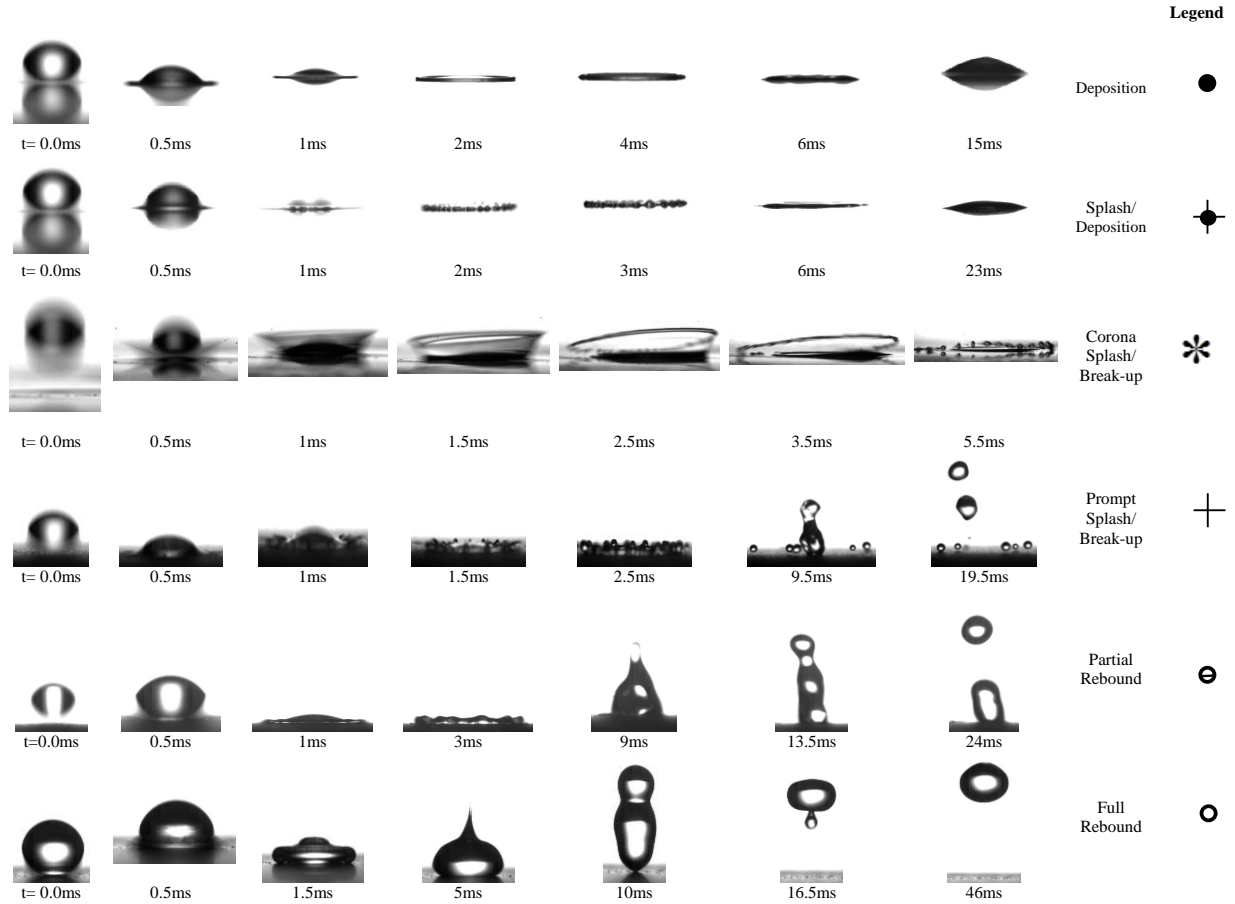


Figure 3.4 Observed outcomes of droplet-wall collision

Most of the outcomes were clear in nature in terms of the classification. However, as it approached the transition boundary, the outcomes were not distinctly clear with a hybrid of two outcomes were observed. In those cases, the outcomes were analyzed and were classified as the outcome that it resembled the most. Also, more experimental cases were conducted in the transition regime to capture the exact point of transition.

These outcomes are similar to those defined by Rioboo *et al.*¹ but definitions outcomes vary slightly for the conditions examined herein which focused on surfaces with both hydrophobic and hydrophilic properties and fluid viscosities ranging from that for pure water to pure glycerin

(with in between viscosities ranging from glycerin/water mixtures of 40% to 94% glycerin by weight). For example, Rioboo *et al.*¹ did not differentiate between the splash/deposition that occurs on the hydrophilic surfaces to splash/break-up which results in the droplets staying aloft in the air. The Weber number was generally adjusted by varying droplet height since the droplet diameter was generally fixed as 2 mm, since larger droplet diameters tended to yield significant aerodynamic deformation. This allowed the present work to focus on spherical, or nearly-spherical, droplet shapes before impact to avoid further test condition complexities. For this drop size, the maximum Weber that could be attained in the present experiments was limited to about 500 since the droplet impact speeds were limited by their terminal velocity.

For impact on an aluminum surface, the outcome of droplet-wall collision is shown in the We-Oh regime plot of Fig. 3.5. Only two outcomes, i.e. deposition and splash/deposition were observed. Deposition is more likely at low Weber numbers while splash is more likely at higher Weber numbers. However, increased fluid viscosity made the deposition outcome more likely to occur. The experiments qualitatively match the general trend that was seen with the previous experiments, shown in Fig. 3.1, for a wide variety of surfaces. Also shown in Figure 3.5 are two of the previous empirical models intended to determine the splash/deposition boundary (whereby these models are not a function of the surface chemistry). Although both the previous models show the same trend as seen the present experiments, a solid line is shown in this Fig. 3.5 which is a fit for the current data specifically for smooth dry aluminum surfaces.

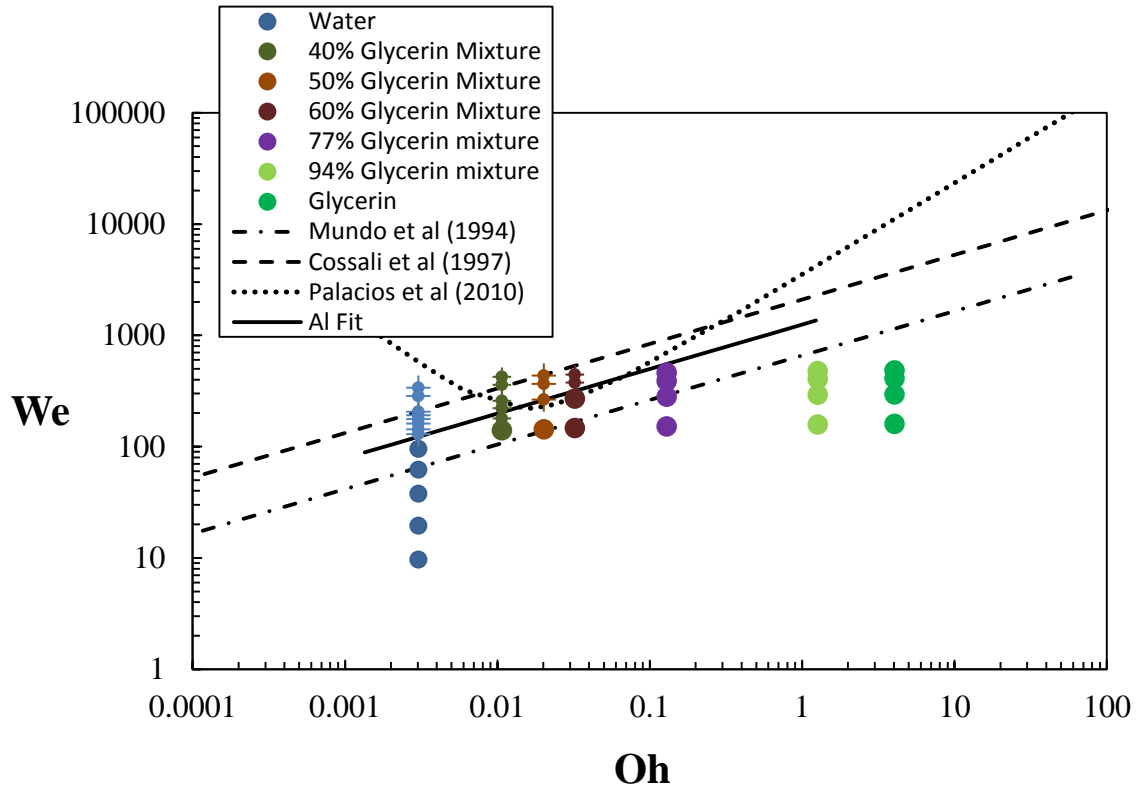


Figure 3.5 We-Oh regime for various liquid on aluminum surface with various previous empirical models that describe boundary between deposition and splash/deposition shown by dashed lines and the fit for smooth dry aluminum surfaces based on present data shown by a solid line.

The next set of test considered droplet impact on a superhydrophobic surface, denoted as SH-1 which is an irregular nano-composite coating of about 1 micron in roughness created by spray-casting slurry of SiO_2 nano-particles suspended in a solvent and a fluropolymer¹⁴. The resulting outcomes in the We-Oh space are shown in Fig. 3.6 using the same liquids as before, but which include two new outcomes not seen before on an aluminum surface. In particular, a complete bounce (open symbol) and a partial bounce (plus symbol) were observed as outcomes for 50% water-glycerin mixture. For pure water, the bounce occurs at a very low impact Weber number (~ 0.5) and at Weber number greater than 35 splashing is observed. This indicates that the critical deposition Weber number, i.e. the Weber number at which the transition from deposition occurs,

is lower than 0.5 for water on a superhydrophobic surface. The fit of the boundary is therefore shown as a dashed line as it only indicates an uppermost location of this regime boundary.

This estimated boundary for deposition of a water drop on a superhydrophobic surface is in marked contrast compared to the critical deposition Weber number of about 70 observed for water droplets on aluminum (both boundaries are shown on Fig. 3.6). The difference in outcome due to the surface change is also observed for 40%, 50% and 60% mixtures of glycerin and water but to a lesser extent. For glycerin mixtures of 77% or higher, only deposition was observed within the present test conditions and so it is difficult to determine whether the outcome boundary sensitivity to surface persists for these fluids. Overall, the impact of surface chemistry/geometry was much more profound for water droplets than for the higher viscosity glycerin mixtures. To understand this behavioral and outcome shift, it is instructive to consider the role of contact angle, which is defined by a combination of the fluid and the surface.

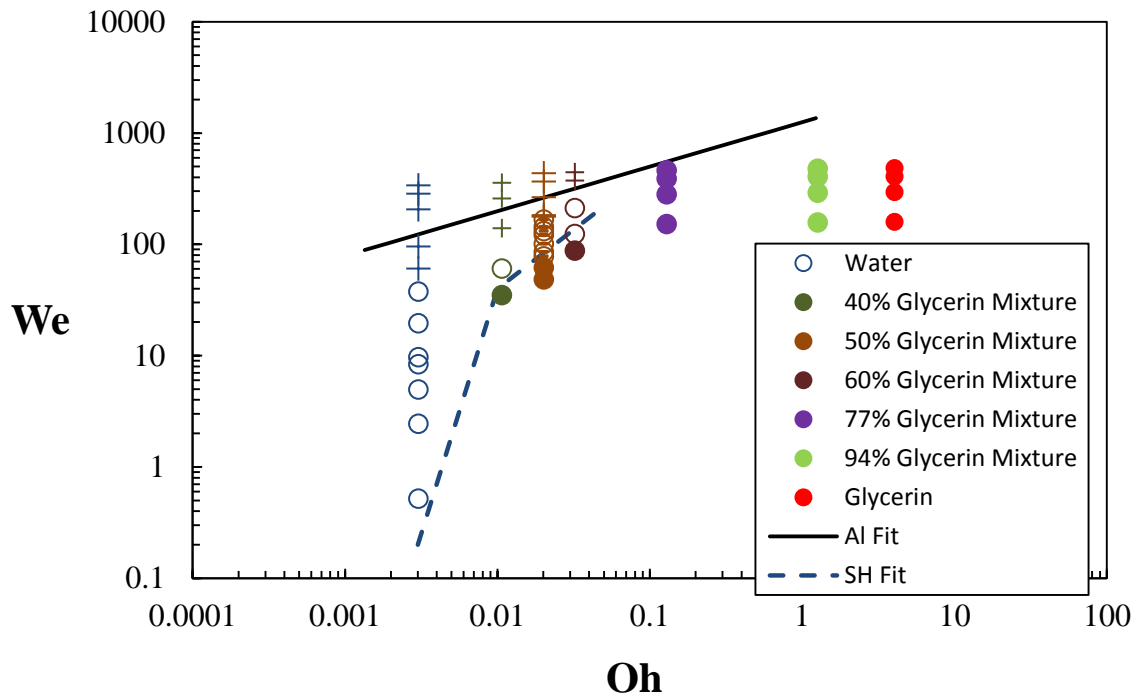


Figure 3.6 We-Oh Regime for Various Liquid on a superhydrophobic surface, SH-1, and fit for this surfaces based on present data shown by dashed line.

3.3.2 Effect of Contact angle

To investigate the effect of contact angle, different surfaces were tested with a fixed fluid (e.g. water) so that the Ohnesorge number remains a constant but the contact angle was varied. The five surfaces that were tested included two hydrophilic surfaces (acrylic and aluminum) and three hydrophobic surfaces (Teflon, SH-1, and NeverWet®). NeverWet is a commercially available spray-treatment that was applied herein to aluminum using a spray distance of about 6 inches to create a superhydrophobic coating. The advancing and receding contact angles were generally measured for these surfaces for water, glycerin and the glycerin mixtures with a

goniometer and a digital camera. The results are listed in Table 3.1 and the hysteresis angles (the difference between advancing and receding angles) are listed in Table 3.2. The trends indicate that the increase in viscosity and reduction of surface tension that is associated with increasing glycerin content generally led to a reduction in both the advancing and receding contact angles.

Table 3.1 Measured contact angles of different liquids on various surfaces

Liquid	Advancing and Receding Surface Contact Angles [deg]				
	Acrylic	Aluminum	Teflon	SH-1	NeverWet™
Water	79, 18	65, 23	97, 51	155, 147	158, 150
40% Glycerin Mix	64, 14	55, 13	99, 40	145, 120	151, 142
50% Glycerin Mix	52, 29	68, 37	79, 60	139, 123	145, 130
60% Glycerin Mix	62, 15	73, 12	89, 34	140, 125	157, 144
77% Glycerin Mix	68, 54	64, 44	87, 55	150, 126	*
94% Glycerin Mix	69, 41	73, 33	74, 54	149, 136	*
Glycerin	74, 37	74, 42	72, 44	*	*

* not measured in this study

Table 3.2 Measured hysteric contact angles of different liquids on various surfaces for fluids used to determine deposition boundary

Liquid	Hysteresis Surface Contact Angles [deg]				
	Acrylic	Aluminum	Teflon	SH-1	NeverWet™
Water	61	42	46	8	8
40% Glycerin Mix	50	42	59	25	9
50% Glycerin Mix	23	31	19	16	15
60% Glycerin Mix	47	61	55	15	13

The static and advancing contact angles are difficult to predict and the receding contact angle is a more deterministic measurement to predict.¹⁵ The droplet-wall collision outcomes were then analyzed based on the receding contact angles of the different surfaces for a fixed liquid. This choice is based on results of Rioboo *et al.*¹ and Antonini *et al.*¹³ who noticed that the receding

contact angle is more important than static or advancing angle with respect to the phenomena of break-up.

The outcome of water droplets on various surfaces is shown in Fig. 3.7, the critical Weber number (associated with the transition from deposition to another outcome) consistently decreased as the receding contact angle increased. It was also observed that the decrease is gradual in the hydrophilic region but becomes very large in the hydrophobic region. This trend was simply approximated with a fit of two straight lines to respectively represent the hydrophilic and the hydrophobic regions, as defined with respect to the receding angle. A single curved line fit would have been another viable option, but more experimental data would be needed to quantify such a variation. In either case, the more rapid reduction in critical Weber number for the hydrophobic regime indicates that surface properties become more important as the surface energy reduces. This trend is consistent with other data to be shown later.

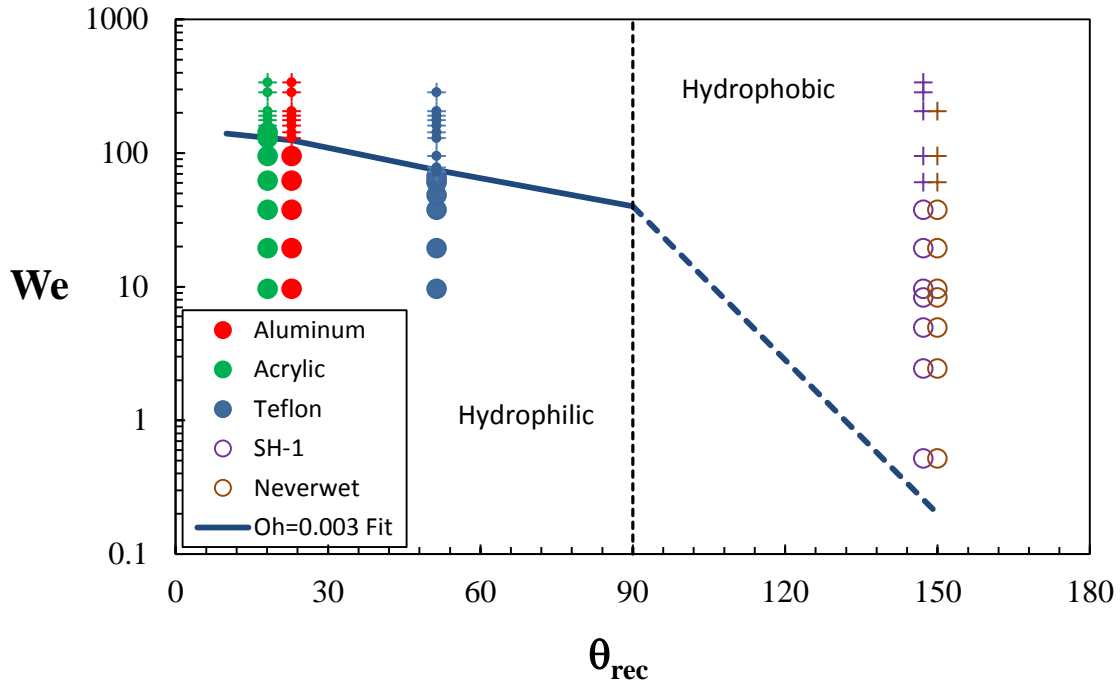


Figure 3.7 Water droplet collision outcomes on various surfaces for the hydrophilic and hydrophobic regimes as defined by the receding contact angle, along with simplified boundary fits for the hydrophilic region and for the hydrophobic region.

It is also important to note that above the critical Weber, the hydrophilic regime (as defined by receding angle) yields a splash/deposition whereas the hydrophobic regime yields a splash/partial breakup. These two different outcomes are contrasted in Figure 3.4 (as the 2nd and 4th rows) and indicate that the lower surface energy has allowed the spreading droplet material to separate from the center material (rather than coalescing into a deposited state). This suggests that a Cassie/Baxter regime is maintained throughout the drop-wall collision interaction on the superhydrophobic surfaces so that the droplet inertial dynamics can allow breakup. In contrast, the hydrophilic surfaces outcomes suggest a Wenzel regime has pinned at least part of the drop allowing it to be stabilize, which prevents breakup. Note that the splash/deposition outcome result of Fig. 3.7 is consistent *only* if a surface is defined as hydrophilic based on its receding

angle (whereas teflon is actually hydrophobic when based on static contact or advancing contact angles). This supports the use of receding angle to characterize the outcome of these drop-wall collisions, though it is expected that advancing angle should play at least a secondary role since it can influence the initial spreading of the droplet. Clearly, experiments with more surfaces would help better understand the physics and provide a more quantitative boundary (or set of boundaries) for the outcomes of water drops on various surfaces.

The outcomes for the 40% and 60% glycerin-water mixture on various surfaces are shown in Figures 3.8 and 3.9 where hydrophilic and hydrophobic regimes are again defined based on receding angle. As in Fig. 3.7, the critical Weber number (that provides an upper bound for simple deposition) similarly reduces as receding angle increases, and this reduction is accelerated as the interactions enter the hydrophobic regime. Also, as seen for the water droplets, the outcome at Weber numbers above the critical value is a splash/deposition for the hydrophilic regime but a rebound for the hydrophobic regime, that transition to a partial rebound at still higher Weber numbers. However, there are quantitative differences between the outcomes as the droplet Ohnesorge number is increased. In particular, the deposition boundary is translated to larger Weber numbers for the glycerin mixtures. This is particularly evident at high receding contact angles where deposition was not recorded for the water drops but was seen for the glycerin/water mixtures. This indicates that higher Ohnesorge numbers yield an increased critical Weber number, an effect that was also evident in Figs. 3.5 and 3.6.

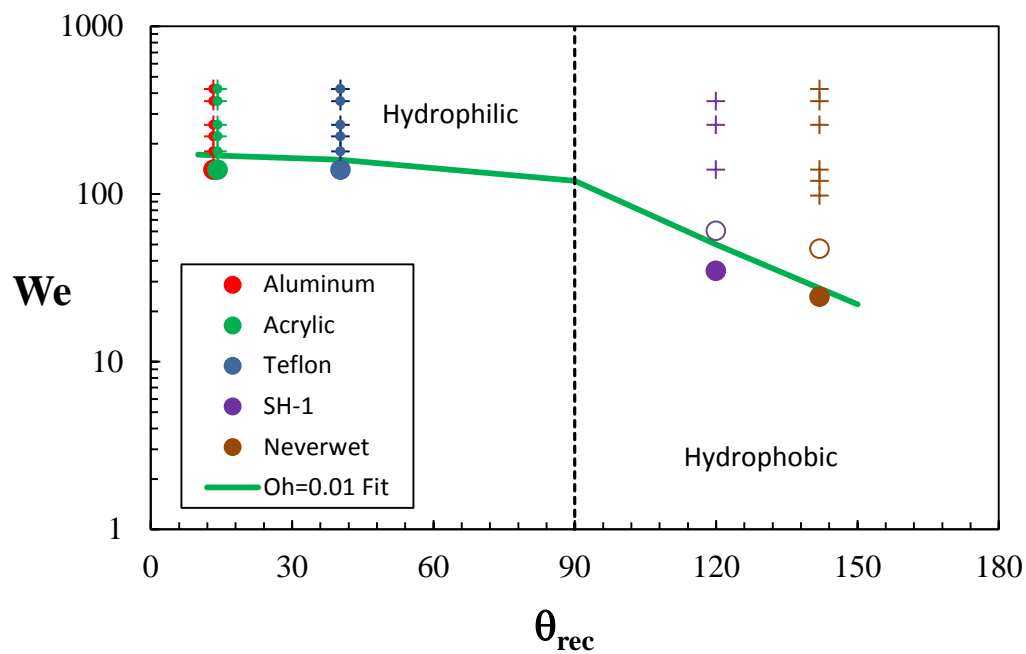


Figure 3.8 Collision outcomes on various surfaces as a function of receding contact angle for 40% Glycerin/Water droplets

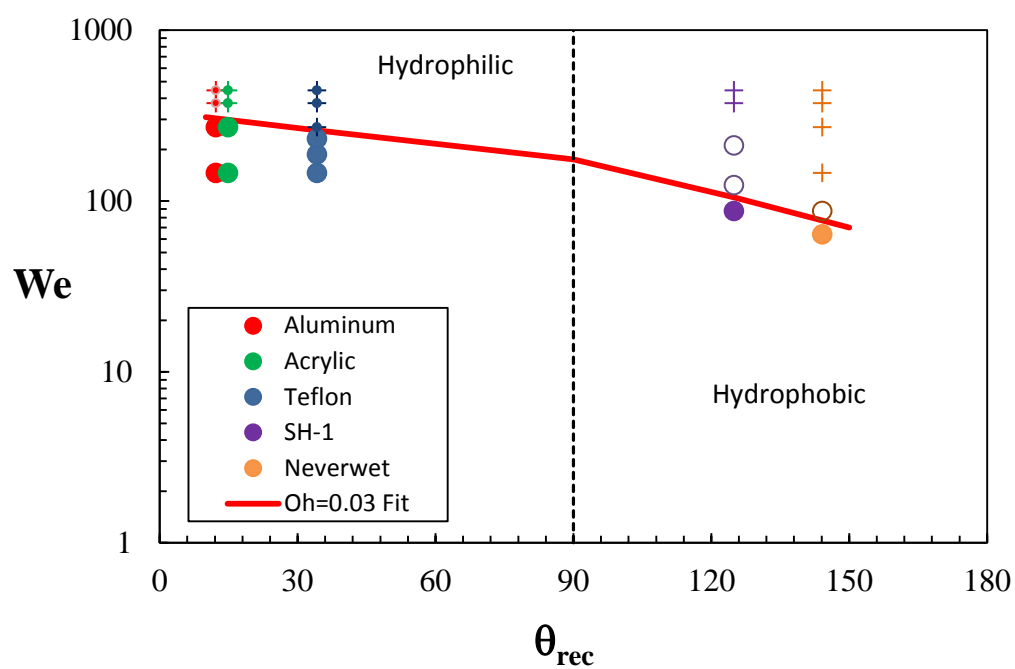


Figure 3.9 Collision outcomes on various surfaces as a function of receding contact angle for 60% Glycerin/Water droplets

Figure 3.10 shows the droplet outcome for a 77% glycerin/water mixture. In this case, all the droplet impact outcomes (which were limited a maximum Weber number of 500 due to experimental constraints) led to deposition. As such, the deposition boundary cannot be determined directly and instead a dashed line is shown to qualitatively indicate the lowermost expected location of this boundary. However, the results are consistent with the above trends associated with Ohnesorge number in that higher Ohnesorge numbers yield an increased critical Weber number.

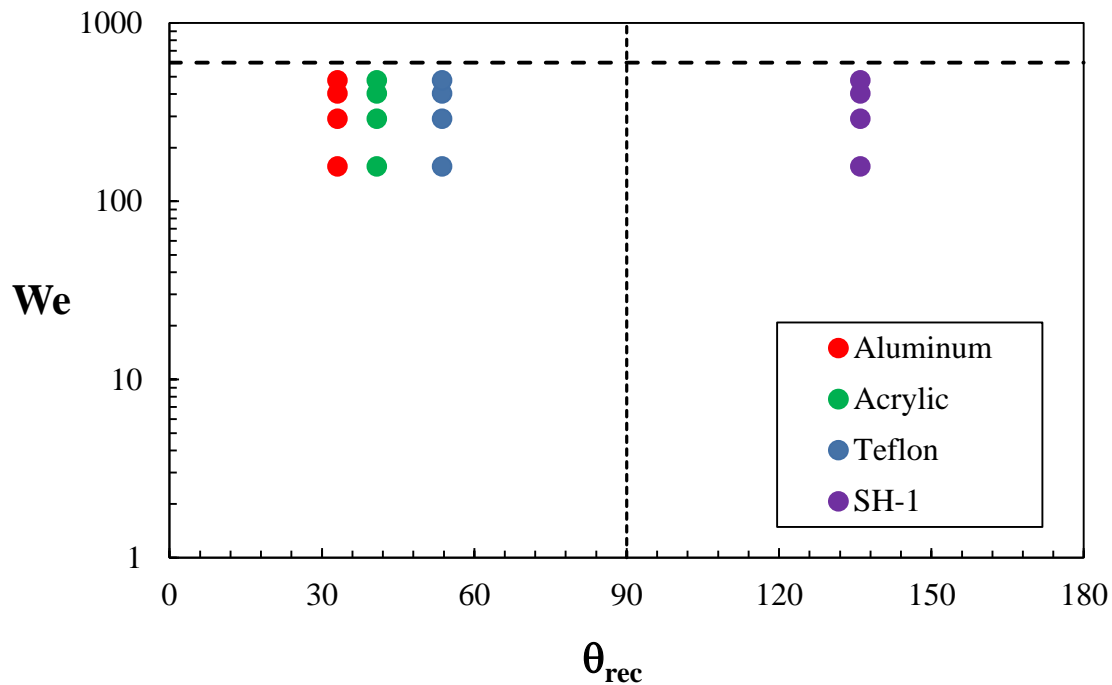


Figure 3.10 Collision outcomes on various surfaces as a function of receding contact angle for 77% Glycerin/Water droplets

Figure 3.11 shows the respective trends for the critical Weber number for the various liquids. As discussed above, We_{dep} is reduced at lower Ohnesorge numbers and especially at high

receding angles. This consistent sensitivity of the droplet outcomes to the surface receding contact angle (θ_{rec}) demonstrated by Fig. 3.11 explains why outcome boundaries of previous studies showed strong inconsistency when considered in terms of only Weber number and Ohnesorge number. For example, the outcomes results at low Ohnesorge numbers in Fig. 3.1 shows a strong differences, whereby the data Schmidt and Knauss indicates a very low We_{dep} while the We_{dep} for Palacios at low Ohnesorge is very high (and the present results for water drops on aluminum indicate an intermediate boundary between these two extremes). The results of Schmidt and Knauss can be attributed to their use of liquid metal droplets, which are associated with a high θ_{rec} that will reduce We_{Dep} . In contrast, the Palacios measurements in this regime employed about 3mm droplets on a glass surface, which will yield a small θ_{rec} associated with a large We_{dep} . Therefore, both previous and present results indicate that both fluid and surface properties are critical to the type of droplet wall outcome. This explains some of the discrepancies seen in Fig. 3.1 as the molten droplets and water droplets on glass have significantly different contact angles.

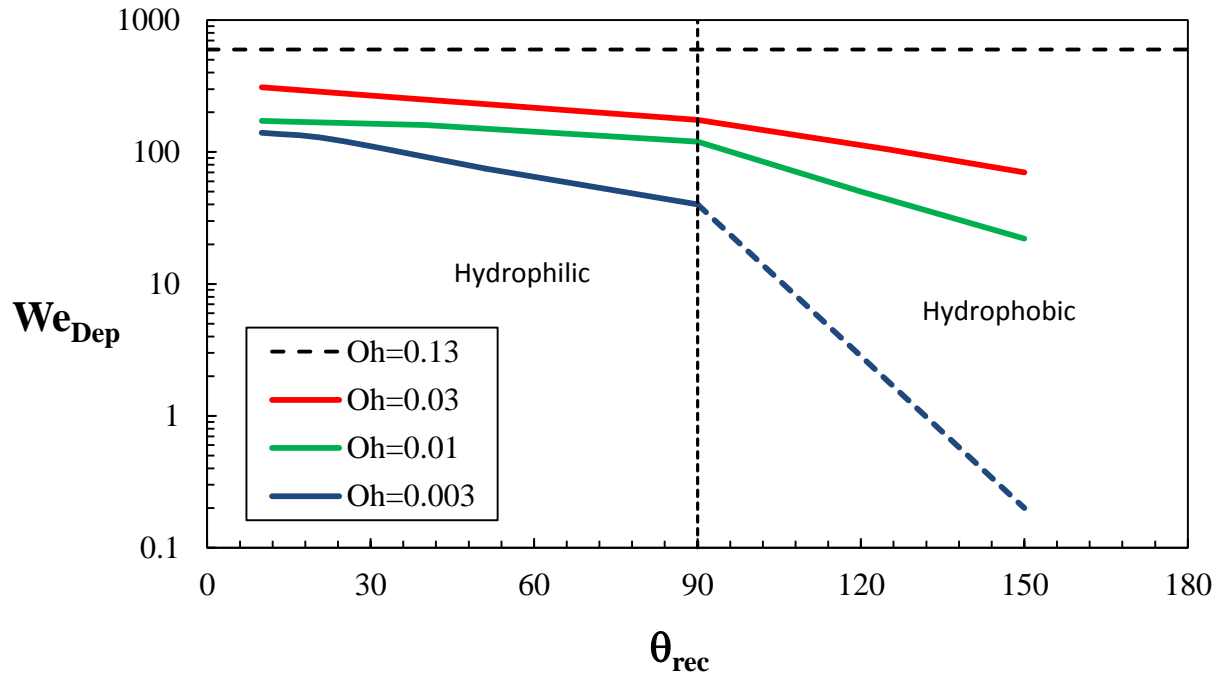


Figure 3.11 Plot of We_{Dep} against the receding contact angle for various Ohnesorge liquids

The trends are consistent with both the advancing and receding contact angles and it could yet be determined which one of the two has a dominating effect based on available data. However, the same scenario might not necessarily apply in the case of splashing and bounce. Another issue that needs further investigation is the effect of roughness relative to the droplet size. This effect was noted to be important by Rioboo *et al.*¹ and Yarin *et al.*² but maybe even more critical for super-hydrophobic surfaces which employ highly convoluted textured features. The 94% glycerin-water mixtures and pure glycerin droplets showed no difference, as only deposition was observed in all surfaces. Therefore, they are represented by dashed lines which show the lower bound for the water droplet at high contact angle and upper bound with the high concentration of glycerin mixtures. The dashed lines shown are for qualitative purposes.

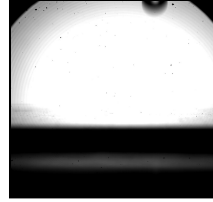
3.4 Conclusion

As a conclusion, this study shows the effect of contact angle on the outcomes in droplet-wall interaction. Two unique outcomes (not seen on smooth metal or glass surfaces) are observed for water droplets on superhydrophobic nano-textured surfaces and include complete bounce and partial bounce . When examining a range of droplet liquids and surfaces, increased viscosity tends to increase the critical Weber number associated with the deposition boundary, which is consistent with the qualitative results presented by previous studies. However, the onset of transition from deposition to splash also decreases as the receding contact angle increases with a gradual change in the hydrophilic region and with a bigger change in the hydrophobic region. This important effect, which is not accounted for by previous models for splash deposition, explains why the previous models were inconsistent with each other. Finally the effects of receding angle on the deposition boundary are greatest when the viscous effects are smallest (low Ohnesorge number). Finally, it is noted that changes in droplet viscosity tend to reduce the receding contact angle for hydrophobic surfaces, so that the Ohnesorge number effect and the receding contact angle effect are both coupled to the droplet properties (and the latter is also controlled by the surface properties).

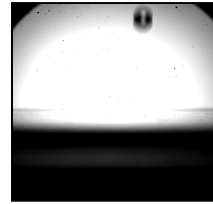
3.5 Appendix

Videos of droplet-wall outcomes from Fig. 3.4:

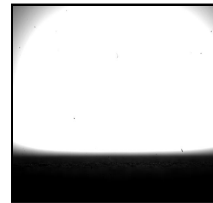
i. **Deposition:**



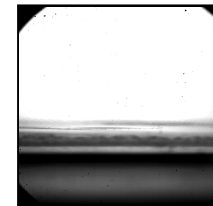
ii. **Splash/Deposition:**



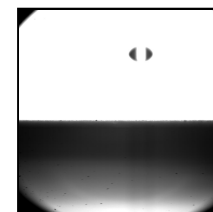
iii. **Prompt splash/Break-up:**



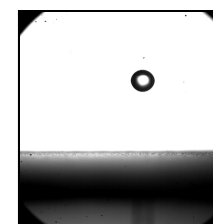
iv. **Corona splash/Break-up:**



v. **Partial rebound:**



vi. **Full rebound:**



3.6 References

1. Rioboo, R., Tropea, C., Marengo, M., *Outcomes from a drop impact on solid surfaces*, Atomization and Sprays, Vol. 11, pp. 155-165, 2001.
2. Yarin, A.L., *Drop Impact Dynamics: Splashing, Spreading, Receding, Bouncing...*, Annual Review Fluid Mechanics, 2006.
3. Lesser, MB. & Field, JE., *The impact of compressible liquids*, Annu. Rev. Fluid Mech., 15:97-122, 1983.
4. Rein, M., *Phenomena of liquid drop impact on solid and liquid surfaces*, Fluid Dyn. Res., 12:61-93, 1993.
5. Wenzel, R.N.; *Resistance of solid surfaces to wetting by water*, Ind Eng Chem, 1936, 28:988-994.
6. Wenzel, R. N., *Surface Roughness and Contact Angle*, Journal of Physical Colloid Chemistry, 53, 9, December, 1466-1467, 1949.
7. Cassie, A. B. D., Baxter, S., *Wetting of porous surfaces*, Trans. Faraday Soc., 1944, 40, 546-551.
8. Mundo, C., Sommerfeld, M. & Tropea, C., *Droplet-wall collisions: Experimental studies of the deformation and break-up process*, International Journal of Multiphase Flow, 21(2):151-173, 1995.
9. Cossali, GE., Coghe, A. & Marengo, M., *The impact of a single drop on a wetted solid surface*, Exp. Fluids, 22:463-72, 1997.
10. Palacios, J., Gomez, P., Zanzi, C., Lopez, J., & Hernandez, J., *Experimental study on the splash/deposition limit in drop impact onto solid surfaces*, 23rd Annual Conference on Liquid Atomization and Spray Systems, Brno, Czech Republic, 2010.

11. Vander Wal, R., Berger, G., & Mozes, S., *The splash/non-splash boundary upon a dry surface and thin fluid film*, Experiments in Fluids 40:53-59, 2006.
12. Putnam, A., *Integrable form of droplet drag coefficient*, American Rocket Society Journal, Vol. 31, Oct., pp. 1467-1468, 1961.
13. C. Antonini, F. Villa, I. Bernagozzi, A. Amirfazli, and M. Marengo, *Drop Rebound after Impact: The Role of the Receding Contact Angle*, Langmuir, 2013.
14. Davis, A., Yeong, Y.H., Steele, A., Loth, E., Bayer, I.S., Effect of Superhydrophobic Nanocomposite Surface Roughness on Anti-Icing Performance, *Nanotech Conference*, Washington DC, 2013.
15. Krishnan, K. and Loth, E., Predicting Contact Angles for Regular Surfaces, *Nanotech Conference*, Washington DC, 2013.

4 Hydrophobic Coating Resistance to Freshwater Biofouling Inception

4.1 Introduction

4.1.1 *Motivation for Reducing Biofouling*

The inception of biofouling consists of bacteria and microalgae producing extracellular polymeric substances (EPS) upon adhering to a surface, which form the base conditions for future adhesions.¹ Therefore, biofouling tends to start with microscopic organisms for short times (less than an hour) and then transitions to mesoscopic organisms (millimeter sized) over moderate times and finally macroscopic organisms (centimeter sized, such as barnacles) over very long times (several days or weeks).

Preventing biofouling in natural bodies of freshwater is important for a wide variety of applications. In particular, biofouling on moving vessels can increase the skin friction drag for surface and underwater which reduces the transport fuel economy, reduces the maximum speed, and increases maintenance cost in terms of hull cleaning. This increase in the skin friction drag can arise due to biological matter adhered to the wetted surfaces which causes hydrodynamic roughening. This roughening can increase drag for both the laminar and turbulent flow regimes when referenced to the flow conditions of the clean (un-fouled) surface.

These two mechanisms can be explained by considering the flat plate skin drag in non-dimensional quantities as shown in Figure 4.1. The vertical axis is the skin friction coefficient (the drag conventionally normalized by the hydrodynamic head and surface area) while the horizontal axis is the flow Reynolds number (product of flat plate length and velocity normalized by the kinematic viscosity). It can be seen that the skin friction in the “laminar smooth” regime reduces as the Reynolds number (Re) increases, but that “transition” (shown by the dashed lines) will cause the skin friction to rise substantially until it reaches the “turbulent smooth” regime.

For example, consider a Reynolds number of 4×10^6 (consistent with a location 1 meter from the leading edge for a surface moving in water at 4 m/s) as shown by the blue vertical arrows on this figure. The skin friction for turbulent flow is more than five times larger than it is for laminar flow. A surface that is very smooth can stay laminar, e.g. surface with less than $5 \mu\text{m}$ roughness based on the lowest dashed line in Fig. 1 and 1m length. However, a surface with about $50 \mu\text{m}$ roughness at this same Re will generally be fully turbulent. Roughness between 5 and $50 \mu\text{m}$ will tend to be in the transition regime, where skin friction can still be significantly greater than the smooth case. For a body length of 10 m, roughness on the scale of $200 \mu\text{m}$ is needed to significantly increase drag once the flow is turbulent.

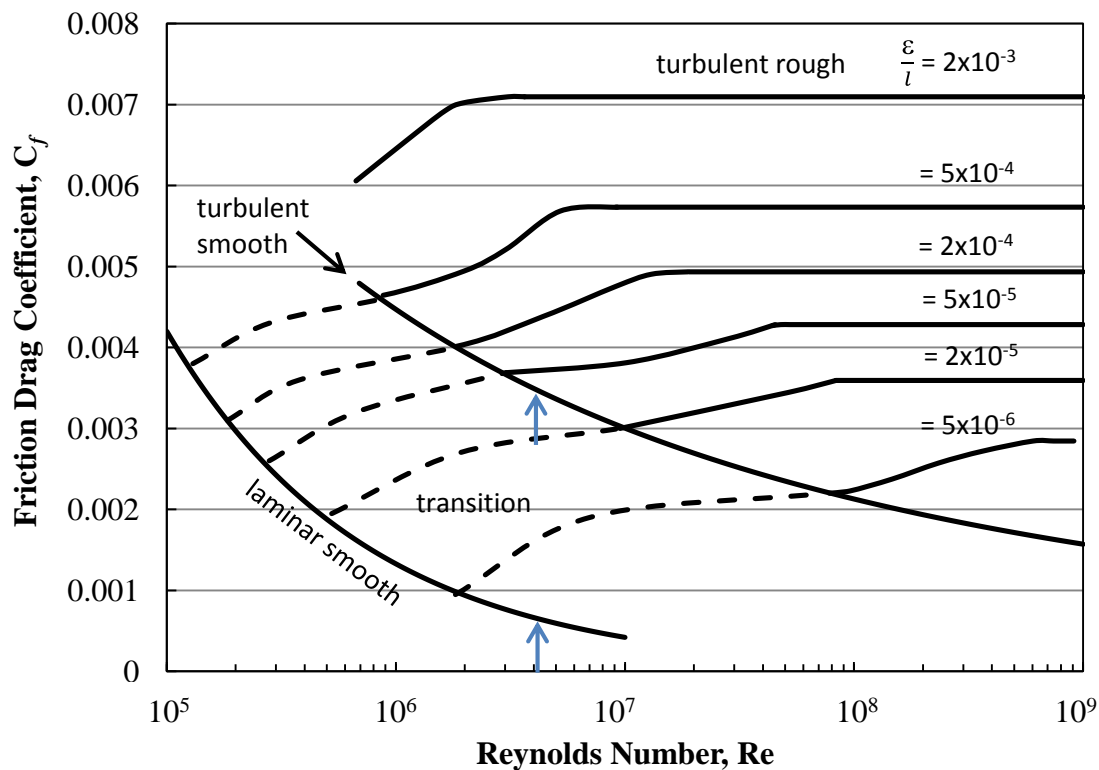
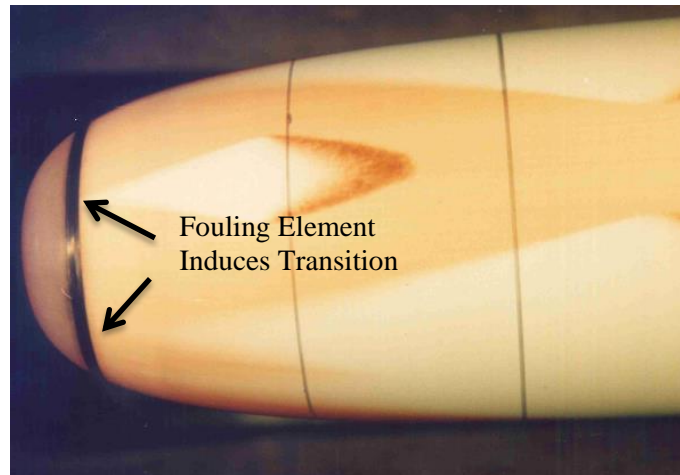


Figure 4.1 Skin friction increase in terms of roughness and Reynolds numbers where blue arrows indicate friction at location for laminar and turbulent conditions.

An example of this is shown in Figure 4.2a whereby an underwater surface test article traveled at a flow speed consistent with laminar flow for smooth surface conditions, but which resulted in transitional flow due to biofouling that occurred by being subjected to ocean-like water with micro-fouling. In particular, one may observe diamond shapes initialing upstream that represent the classic Emmons spots for turbulent transition and rapid skin friction increase. These spots only require a single fouling element to cause transition onset (Fig. 4.2b) and have been shown to occur on aircraft wings fouled by insects², which also cause a skin friction increase. Therefore, preventing biofouling is important to preserve low-drag laminar flow conditions for transitioning, particularly when operating at Reynolds number of 10^6 to 10^7 where it becomes more difficult to ensure flow stability.

a)



b)

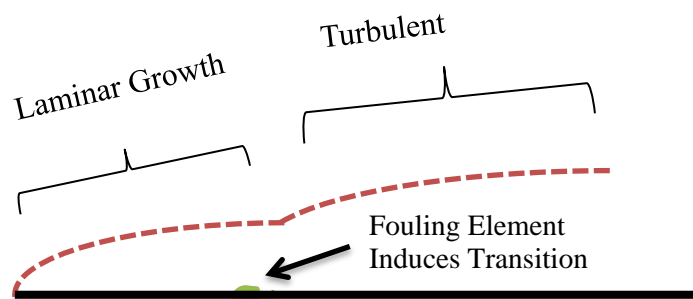


Figure 4.2 Biofouling effects on boundary layers: a) surface-view visualization of turbulent transition due to fouling elements (glass microspheres) shown by arrows from flow over a test article in the 48" water tunnel in the Applied Research Lab at Penn State University, courtesy Alan Jennings³, and b) side-view of average boundary layer growth (as dashed line) due to transition caused by fouling element.

At higher Reynolds numbers, biofouling increases drag through a different mechanism namely that of roughness effects. This can also be seen in Fig. 4.1 by considering a Reynolds number of 10^8 (consistent of the drag 10 m from the leading edge for a vessel moving at 10 m/s). At this Re value, the flat plate turbulent drag for a non-dimensional roughness of 5×10^{-5} is more than 60% larger than that for a smooth plate. In dimensional terms, the former corresponds to

surface roughness of 500 μm which is much larger than that associated with turbulent transition. Therefore, drag increases due to biofouling are generally more profound for the baseline laminar flow regime ($10^6 < \text{Re} < 10^7$) than for the turbulent flow regime ($\text{Re} > 10^7$), where the latter can be sensitive to even small amounts of micro-fouling. This regime is the focus of the present study, but preventing micro-fouling can also help prevent long-term macro-fouling that is important at high Reynolds numbers.

4.1.2 Previous Antifouling Studies

In the shipping industry, fuel economy is at a premium so maintaining smooth surfaces without biofouling is beneficial. This has led to several investigations of antifouling strategies. However, some highly-effective anti-fouling solutions carries negative ecological ramifications. This is because products using toxin-release systems designed to kill attached organisms (as opposed to preventing adhesions) can be environmentally harmful if released over long periods of time, especially in confined regions such as bays or ports. This has been halted to a large degree by the the International Maritime Organization Treaty on biocides in 2008, and this has led to rapid growth in studies for new, environmentally benign solutions.⁴ Biomimetic solutions are of particular interest, i.e. antifouling mechanisms found in the natural world. These mechanisms vary from antibacteria nanopatterns on a cicada wing to secretion from skin pores on whale skin.^{6,7} The associated natural material properties often also include as hydrophobicity and self-cleanability to prevent fouling.⁵ These natural properties are now used to inspire synthetic coatings such as the use of liquid-infused surfaces which can prevent bacterial adherence in air.⁸ Another strategy is to introduce a bacterial microbiofilm that can, in the case of certain species, prevent future macrofouling.⁹ However, these solutions lack universal

applicability for underwater fouling and there is no consensus for an inexpensive and effective solution.

4.1.3 Objectives

Most biofouling studies have focused on preventing long-term biofilm whereby colonies of microorganism grow. However few, if any, have focused on the short-time biofouling inception whereby micro-organisms can collect on surfaces due to their relative inertia causing them to impact on the a surface moving at a significant speed. Therefore, the current study focuses on short-term exposure associated with the inception of fresh-water micro-biofouling. It also examines the effectiveness of inexpensive nano-composite environmentally-friendly superhydrophobic surfaces in comparison to conventional polyurethane coatings and smooth teflon surfaces. The performance of these various coatings is quantified by measuring the relative number densities and heights of micro-fouling elements over a short-time interval at a fixed water velocity.

4.2 Experimental methods

4.2.1 Surfaces Preparation and Characterization

To choose the surfaces to be tested in dynamic conditions (in moving water), initial screening included freshwater static tests (in still water). This was achieved by transporting roughly 0.5L of a local pond water to an open container in the laboratory. Various coated substrates and surfaces were then immersed in these container for a period of 5 days. Following this period, the samples were lightly rinsed with clean water prior to being imaged under the 3D digital microscope for fouling height and population density analysis. The static test on the

polyurethane coating indicated the beginnings of a biofilm with about 10% of the sample covered by fouling specimens. In contrast, Teflon and the superhydrophobic surface showed negligible fouling. Furthermore, the superhydrophobic surface did not saturate (maintained an air layer) over the the 5 day underwater period and retained a very low drop roll-off angle performance immediately after it was removed from the container. In general, the results for the static testing are qualitatively consistent with the dynamic testing as will be described in more detail below.

For the dynamic testing, one-inch by two-inch square samples were coated with polyurethane (PUR), polyurethane (PUR) top coated with hydrophobic Capstone, teflon (Polytetrafluoroethylene - PTFE), and a polyurethane top coated with nanocomposite superhydrophobic (PUR + NC) surface were prepared. The surfaces are listed in Table 1 and were chosen based on the off the shelf boat/vessel coating investigation that identified that most industry coatings were polyurethane based. The capstone coating, teflon and nanocomposite coating were chosen due to hydrophobic and superhydrophobic properties. Details of the preparation of each surface are discussed below, followed by the procedure used to characterize contact and roll-off angles as well as the roughness.

Table 4.1 Properties of Surfaces

	Static Contact Angle (θ_{static})	Roll-Off Angle ($\theta_{\text{roll-off}}$)	R_a (μm)
Polyurethane (PUR)	77°	48°	0.05
PUR + Capstone	90°	45°	2.10
Teflon	110°	25°	0.36
PUR + NC	150°	2°	2.60

For the polyurethane samples, preparation consisted of applying a glass slide with a polyurethane coating and polishing cloth (average particle diameter = 0.01 μm) the sample to

reduce the final surface roughness. The polyurathane and Capstone samples were prepared by starting with a glass slide and applying polyurathane and polishing it to a smooth finish. After that, the polyurathane coated slide is dipcoated with Capstone solution and then air dried. This introduced some fine roughness but the final roughness still less than the critical 5 μm . The teflon samples were purchased as such and then sanded with 1000-grit sandpaper (average particle diameter = 18.3 μm) prior to polishing with polishing cloth as this provided the lowest surface roughness. The superhydrophobic surface was sprayed on the glass slide using a silicon dioxide based formulation followed by baking in an oven for overnight. The superhydrophobic surface was not polished or sanded because its superhydrophobic properties are derived from its surface finish, i.e, roughness. However, the final roughness was 2.60 μm ($< 5 \mu\text{m}$) and this was deemed to not affect the flow characteristics from the calculations in section 4.1.1 and Fig.4.1.

Following their preparation, the samples were examined for surface roughness measurements. The goal prior to measurement was to employ surfaces with R_a measurements below the critical height for laminar flow disruption ($\sim 5 \mu\text{m}$) so that they would not induce transtion if the remained clean (unfouled) while in a moderate Reynolds number condition.

The samples were then imaged on a Hirox 3D digital microscope. These pre-testing images are shown for polyurethane and Teflon as a baseline for comparisons with post-test images.

4.2.2 *Dynamic Testing*

This obejctive of the dynamic testing was to investigate inception of freshwater biofouling for various surface properties, by subjecting the samples in a short-term, moving-water environment. The testing was conducted at the Rivanna resevoir near Charlottesville Virginia

during the month of February to April. Samples were flush-mounted to the vessel surface (a rowing shell) corresponding to 15 cm below the waterline and 1 m from the leading edge. The vessel was then translated in a straight line for 45 minutes at about 4 m/s (this speed corresponds to $Re=4 \times 10^6$). The surface was then removed, transported to the lab in a closed container, rinsed with deionized water and then subjected to 3D digital microscopy within 1 hour of the end of the dynamic testing.

4.3 Results of Dynamic Testing

The dynamic tests were characterized through qualitative imaging and followed by quantitative counting and sizing of fouling elements. Samples of the imaging are shown in Fig. 4.3 where the left column shows the surfaces before testing and the right-hand-side shows the surfaces after testing.

The polyurethane sample showed the greatest fouling over the 45-minute time period as seen by the right-hand side of the top row. The largest specimen found on the dynamic polyurethane test was over 50 μm in height and there were several specimens over 20 μm in height. These very large particles tended to be small insect legs or plant parts. Such large adhesions were not observed in static testing and indicate particle impact due to the surface movement within the freshwater environment. However, the main biofouling specimens for the polyurethane sample were algae of roughly 5 μm in height, a result which was consistent with the static testing. Such elements were also observed, but with lower number density on the PUR + Capstone surface as shown by the right-hand side of the second row. No large (>50 μm) specimens like the insect legs and plant residue were observed in this sample. However, algae on the order of 5 μm were still observed, albeit with lower number density.

The teflon is pictured in the third row of Fig. 4.3, which again shows the absence of very large ($>50\text{ }\mu\text{m}$) elements. Consistent with the trend, particles on the order of $5\text{ }\mu\text{m}$ is observed although in lower quantities.

For the superhydrophobic surface (PUR + NC) pictured on the last row, the 3-D texturing which is integral to its high contact angle performance. These surface textures dwarfed any fouling specimen so that no new hydrodynamic roughness resulted from biofouling. It is important to note that the superhydrophobic surface became saturated over the 45-minute time period. This is likely due to the increased dynamic pressure associated with water flow (whereby the static test indicated no saturation).

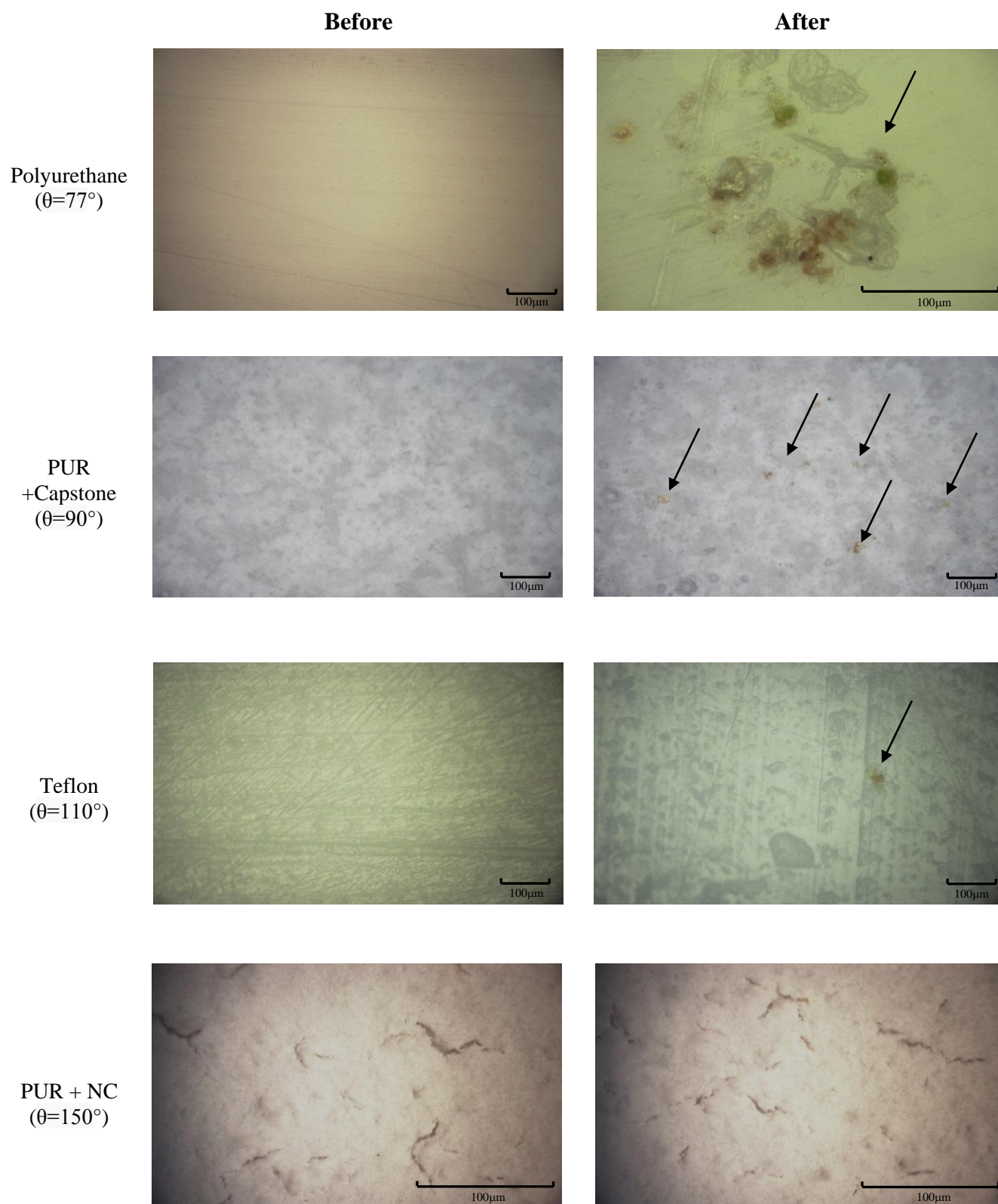


Figure 4.3 Images of surfaces before and after dynamic testing with arrows indicating fouling elements (very little fouling was observed for the PUR + NC surface).

A key observation from the dynamic experiments was the multitude of microorganisms, and this is demonstrated by the images shown in Fig. 4.4. The different microorganisms might have different method of attaching themselves to the surfaces, i.e. via adhesion, via hook, etc. and that could impact on the colonization rate of the surface. Figure 4.4a shows the close-up image of algae which was the most common microorganism observed. In addition to that, some fine plant litter and ciliates (Fig. 4.4b and c) were also observed. A fair amount of chlorophytes and insect parts were also observed under microscope. Besides that, there were a good amount of microorganisms that were not identified that had different shape, size, color and transparency one of which is shown in Fig. 4.4f.

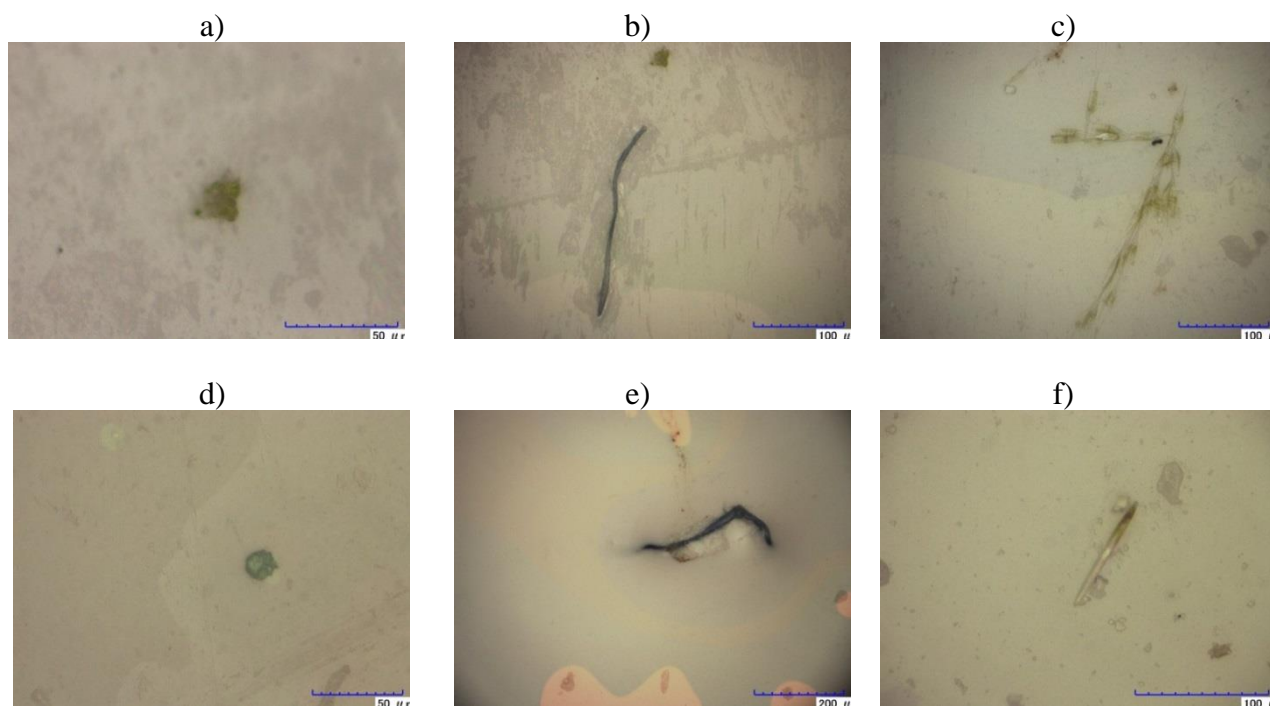


Figure 4.4 Magnified images detailing the variety of biofouling specimens found on the polyurethane sample, including a) algae, b) fine plant litter, c) ciliates, d) chlorophytes, e) insect parts, and f) unidentified microorganism

In order to quantify the heights of the sample, the sample was placed under a 3D microscope and a 3D topographic map was generated. A sample of image analysis used to identify the heights of microorganism is shown in Fig. 4.5a and b. Figure 4.5a shows the image analysis of PUR sample that tended to have a very large roughness that was in the order of 50 μm . Similarly, the image of a teflon sample that had elements with heights around 5 μm . Important note is to taken during the image analysis, is although the images might look similar they may vary in heights.

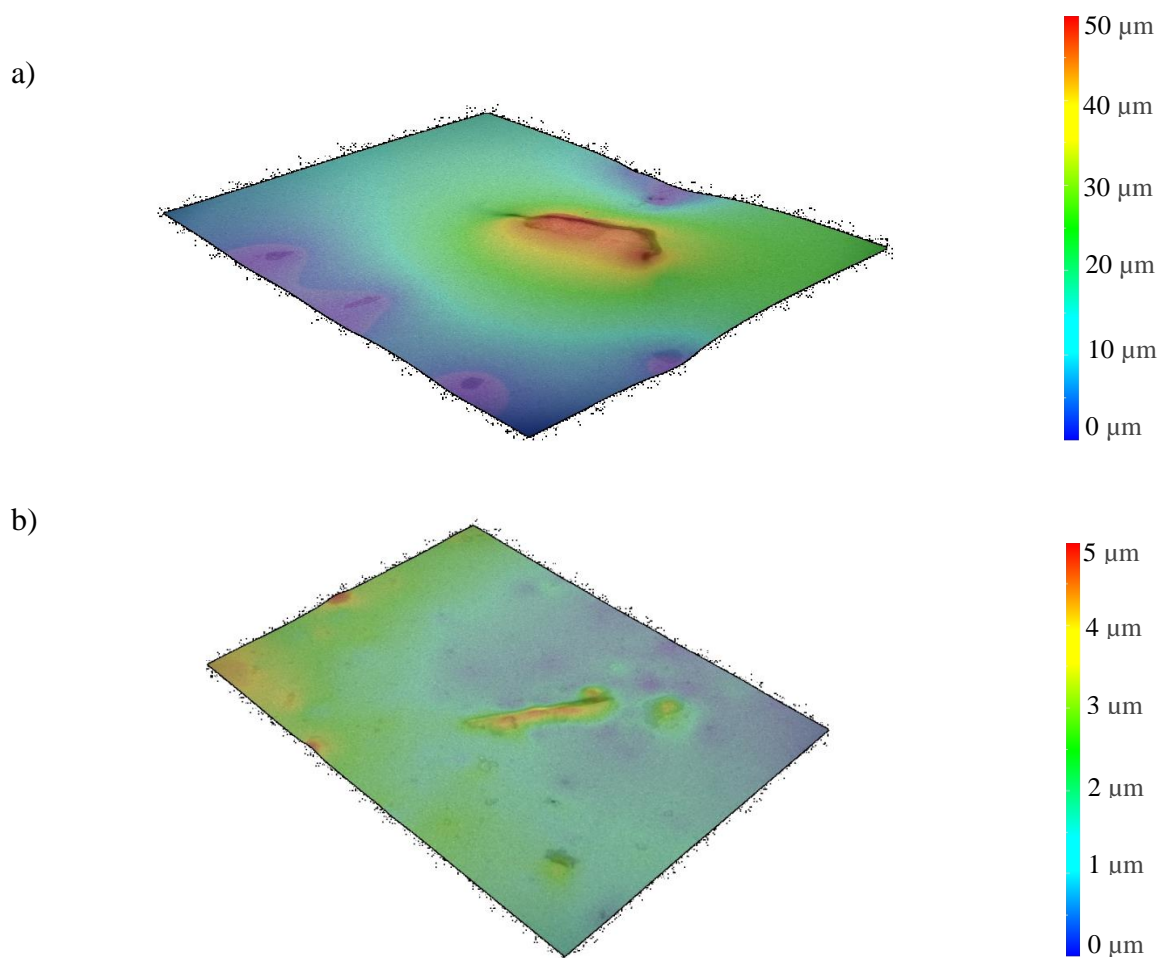


Figure 4.5 Three-dimensional surface rendering based digital microscope: a) for Fig. 4.4e, b) for Fig. 4.4f

The biofouling elements were then split into different height bins of 0 μm up to 20 μm in steps of 5 μm . Using the height analysis topography and digital microscope image, the heights of biofouling elements were recorded and counted. The height and number distribution of the biofouling elements of the surfaces are shown in Fig. 4.6.

Polyurathane (PUR) had the highest number of fouling elements in a 1cm x 1cm field of view (FOV) with 2557 fouling elements. In addition to that, the polyurathane also had the fouling elements in various heights ranging from 1 μm to larger than 20 μm although the number of elements progressively decreased as the height of the elements increased, i.e., more elements in the 0-5 μm range height than 15-20 μm height range. Reduced number of fouling elements were observed on PUR + Capstone surface with 600 fouling elements or reduction of about 77% in a 1cm x 1cm field of view (FOV). It is also interesting to note that no fouling elements beyond 10 μm in height were observed. Consistent results were also observed on teflon surface with 105 fouling elements or 96% reduction from PUR with all elements under the height of 10 μm although teflon had less fouling elements than PUR + Capstone in both height bins of 1-5 μm and 6-10 μm . The superhydrophobic PUR + NC surface had 5 fouling elements in total which translates to a reduction of 99.9% from PUR with all elements being under the height of 5 μm . This is due to the fact that superhydrophobic surfaces maintain superhydrophobicity by maintaining a thin air layer between the surface and water. Due to this thin air layer, the fouling elements are not in direct contact with the surface, making it difficult for the microorganisms to adhere to the surface.

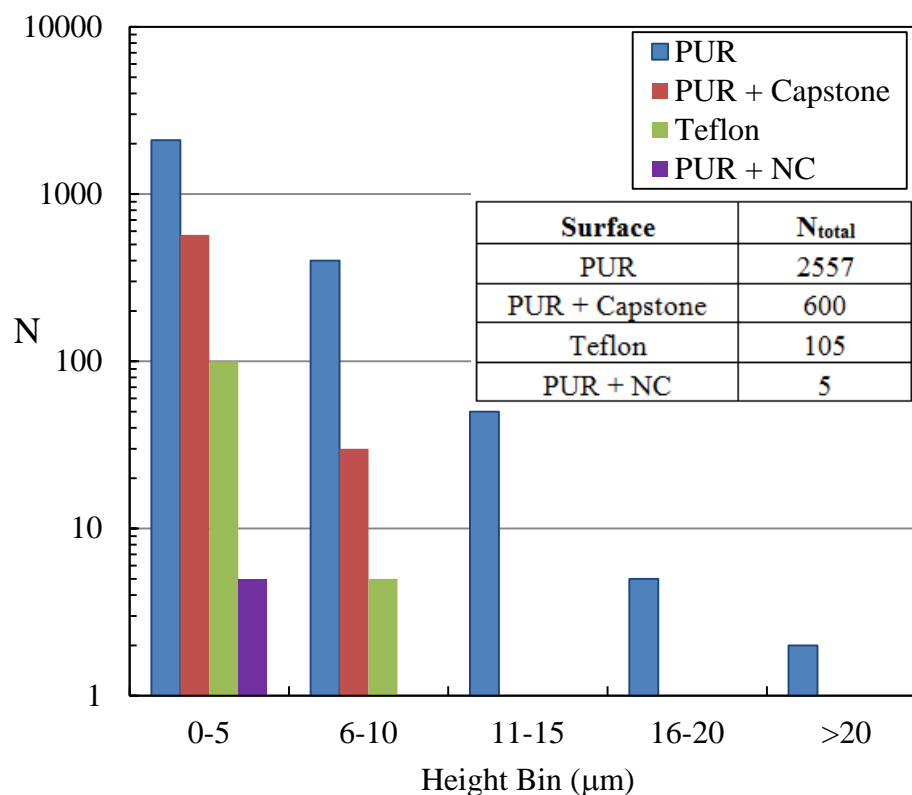


Figure 4.6 Plot denoting average number of fouling elements in a 1 cm x 1cm field of view for each surface based on height bins

Despite the successes in reducing biofouling with the present superhydrophobic coatings, they carry their own limitations as practical substitutes for polyurethane-based paints. The superhydrophobic surfaces, although they start superhydrophobic at the beginning of the test, the surfaces tend to saturate towards the conclusion of the test. This could pose a problem if longer time is needed. The superhydrophobic surfaces also tend to be not durable which may cause a problem in handling and transporting a vessel especially small ones, i.e care needs to be taken by not touching it with bare hands when transporting it. However, given the self-cleaning properties it would be worthwhile to pursue a more durable superhydrophobic surface.

4.4 Conclusions

Biofouling can occur even within a relatively short period of time. Biofouling of microorganisms such as algae, chlorophytes, plant litter, ciliates and others, were present to a large degree on the polyurethane surface in both the static and dynamic freshwater tests. The capstone sample was an improvement over the polyurethane, but large amounts of biofouling remained. The Teflon sample exhibited extreme improvement over the polyurethane surface with a 96% decrease in biofouling elements adherences greater than 5 μm in height, and the nanocomposite superhydrophobic surface essentially (99.9% reduction) eliminated biofouling. This shows that superhydrophobicity can prevent or delay biofouling and performed in a non-detrimental manner to the environment and the aqua species. Although other studies have investigated the use of superhydrophobic surfaces for biofouling prevention, they focused on the long term use. However, in this study, it is shown that superhydrophobic samples could be useful to prevent a short term biofouling inception.

4.5 References

1. Arpa-Sancet, M.P., Christophis, C., & Rosenhahn, A. (2012). Microfluidic assay to quantify the adhesion of marine bacteria. *Biointerphases*, 7(1-4), 26.
2. Wohl, C. J., Smith Jr, J. G., Connell, J. W., Siochi, E. J., Penner, R. K., & Gardner, J. M. (2013). *Engineered Surfaces for Mitigation of Insect Residue Adhesion*.
3. Jennings, Alan. Flow over a test article in the 48" water tunnel in the Applied Research Lab at Penn State University.
4. Rosenhahn, A., Schilp, S., Kreuzer, H.J., & Grunze, M. (2010). The role of “inert” surface chemistry in marine biofouling prevention. *Physical Chemistry Chemical Physics*, 12(17), 4275-4286.
5. Kirschner, C.M. & Brennan, A.B. (2012). Bio-inspired antifouling strategies. *Annual Review of Materials Research*, 42(42), 211-229.
6. Pogodin, S., Hasan, J., Baulin, V. A., Webb, H. K., Truong, V. K., Boshkovikj, V., . & Ivanova, E. P. (2013). Biophysical Model of Bacterial Cell Interactions with Nanopatterned Cicada Wing Surfaces. *Biophysical Journal*, 104(4), 835-840.
7. Salta, M., Wharton, J. A., Stoodley, P., Dennington, S. P., Goodes, L. R., Werwinski, S., & Stokes, K. R. (2010). Designing biomimetic antifouling surfaces. *Philosophical Transactions of the Royal Society A: Mathematical, Physical and Engineering Sciences*, 368(1929), 4729-4754.
8. Epstein, A.K., Wong, T., Belisle, R.A., Boggs, E.M., & Aizenberg, J. (2012). Liquid-infused structured surfaces with exceptional biofouling performance. *Proceedings of the National Academy of Sciences of the United States of America*, 109(33), 13182-13187.

9. Mieszkin, S., Martin-Tanchereau, P., Callow, M.E., & Callow, J.A. (2012). Effect of bacterial biofilms formed on fouling-release coatings from natural seawater and *Cobetia marina*, on the adhesion of two marine algae. *Biofouling*, 28(9), 953-968.